SHOCK INTERACTION WITH DUST LAYERS

A Dissertation

by

AMIRA YOUSUF CHOWDHURY

Submitted to the Office of Graduate and Professional Studies of
Texas A&M University
in partial fulfillment of the requirements for the degree of

DOCTOR OF PHILOSOPHY

Chair of Committee,	M. Sam Mannan
Co-Chair of Committee,	Eric L. Petersen
Committee Members,	Zhengdong Cheng
	Hae-Kwon Jeong
Head of Department,	Ibrahim Karaman

August 2015

Major Subject: Materials Science and Engineering

ABSTRACT

Dust explosion hazards in areas where combustible dusts are found have caused loss of life and halted business operations in some instances. The elimination of secondary dust explosion hazards, i.e. reducing dust dispersion, can be characterized in shock-tubes to understand shock-dust interactions. For this reason, a new shock-tube test section was developed and integrated into an existing shock-tube facility. The test section has large windows to allow for the use of the shadowgraph technique to track dust-layer growth behind a passing normal shock wave, and it is designed to handle an incident shock wave up to Mach 2 to impersonate real-industry scenarios. The characterization experiments presented herein demonstrate the advantages of the authors' test techniques toward providing new physical insights over a wider range of data than what have been available heretofore in the literature.

First, the effect of shock strength on the dust entrainment process was explored by subjecting limestone dust to Mach numbers ranging from 1.10 to 1.60. Also, the effect of dust-layer thickness on the entrainment process was observed by performing tests with two different layer depths, namely 3.2- and 12.7-mm thicknesses. New data were collected to develop correlations between the shock strength and the dust entrainment height as a function of time for each layer depth. The longer observation time and higher camera framing rates led to the discovery of trends not previously observed by earlier studies, such as a clear transition time between the early, linear growth regime and a much-slower, average growth regime. This second regime is

however accompanied by surface instabilities that can lead to a much larger variation in the edge of the dust layer than seen in the early growth regime. In addition, for the linear growth regime, there was no significant difference in the dust-layer height growth between the two layer thicknesses; however, the larger thickness led to higher growth rates and much larger surface instabilities at later times. Next, we conducted experiments to elucidate the effect of particle size and size polydispersity on dust cloud formation phenomena behind blast waves. Through systematic modification of the span of the particle size distribution, the striking effect of polydispersity on the entrainment process was demonstrated. Moreover, correlations between linear dust rise rate and particle size and size polydispersity have been developed. Finally, recommendations for numerical modelers of this field and NFPA 654, *Standard for the Prevention of Fire and Dust Explosions from the Manufacturing, Processing, and Handling of Combustible Particulate Solids* are provided for developing a better dust explosion hazard assessment tool.

DEDICATION

All praise is due to Allah
-Surat Al-Fātihah

To

My love, husband and best friend: Jubair Hossain

My parents: Dr. Abu Yousuf Chowdhury and Fatema Rokeya

My nieces and nephew: Mamnoor, Inshira, Farishta, Shejad

ACKNOWLEDGEMENTS

Being a part of Texas A&M graduate program has been a tremendous experience in my life. It has been such a joyful ride and the credit goes to many individuals that I met past few years. I would like to express my sincere gratitude to Dr. Mannan. I have learned so much from him. He has been there all through my PhD years not only as an academic adviser but also as a mentor to whom I could go for any suggestion related to my profession or family life. I am highly thankful to my co-advisor Dr. Eric L Petersen for his strong support and guidance throughout the course of this research. Dr. Petersen taught me to think outside the box, the variety of experiences I had in Turbo machinery lab have helped me become a better researcher. I would like to thank my committee members, Dr. Zhengdong Cheng, Dr. Hae-Kwon Jeong for their support and guidance. Thanks to Dr. Mashuga and Dr. Delphine Laboureur for their incomparable help that added to the success of this work.

I have to thank Greg for being there for each and every difficult experiment we performed. His credentials added greatly to this work. I have learned so much from his experience. I need to thank Greg also for adding laughter in otherwise serious environment. Special thanks also go to members of the Mary Kay O'Connor Process Safety Centers (MKOPSC), and Dr. Petersen's group, especially to Dr. Pasman, Valerie, Shubharthi, Jiaqi, Olga, Diana, Dr. Rahmani, Dr. Sachdeva, Donna, Anibal, Olivier and Brandon. I need to thank MKOPSC for funding my research and supporting me as a graduate research assistant. This work was supported primarily by the MKOPSC.

Additional support came from The TEES Turbomachinery Laboratory at Texas A&M University. I acknowledge the help from Dr. Calvin Parnell from the Biological & Agricultural Engineering Department at Texas A&M University for their assistance in obtaining the Beckman coulter counter analysis of the limestone dust. I acknowledge Elsevier for giving me copyright permission for reusing article titled "Effect of shock strength on dust entrainment behind a moving shock wave" from Journal of Loss Prevention in the Process Industries in my thesis.

No word is enough to express my feelings for my family. I am thankful to my mother for always believing in me. I can't actually thank her enough for the countless sacrifices she made for giving me this opportunity. I am thankful to my father for clarity, wisdom and courage, I am thankful to my nieces and nephew, they drive me to a better person every day. Finally, I am thankful to Jubair, my husband, for understanding me as a fellow researcher. I am thankful to him for inspiring me to be a better scientist. I have always admired his passion for research. My family has shaped me to be the person I am today. I am in debt to them for everything.

"You can't cross the sea merely by standing and staring at the water."

— Rabindranath Tagore

TABLE OF CONTENTS

LIST OF FIGURES

LIST OF TABLES

CHAPTER I

INTRODUCTION

Dust explosions are a serious industrial issue, which occurs when dust particles are dispersed within a confined space in the presence of an ignition source and an oxidizer (usually air) [1]. According to the chemical safety board, in the past 25 years, the United States has experienced more than 200 dust fire and explosion incidents [2]. The consequences included over 100 fatalities and 600 injuries [2]. In addition, secondary explosions are often more catastrophic in industries than primary explosions. For example, the shock wave of a primary explosion can dislodge flammable dust that might be present in the surrounding areas [1]. This larger dust cloud in the presence of an ignition source could create a more-severe, secondary dust explosion. Figure 1 demonstrates some of the devastating after effects of dust explosions in recent years in the United States.

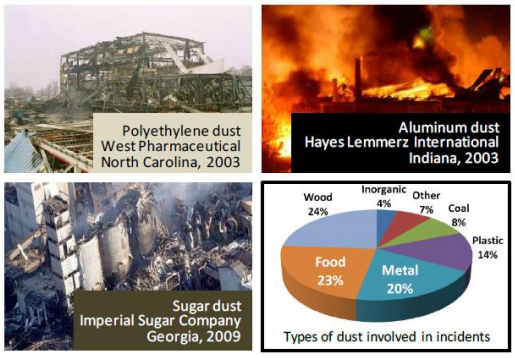

Figure 1: Example of devastating dust explosion accidents in the United States. (Between 1981-2006) [2, 3]

The chairman of United States chemical safety board Carolyn Merritt (2005) quoted, "*Chemical dust explosions in the United States are a serious industrial safety problem*" [2].The imperial sugar incident in 2008 killed 14 people and injured another 36 [4]. This incident let the industry regain awareness about dust explosion hazards. In this specific incident, the magnitude of catastrophic dust explosion was amplified because of a secondary explosion. The primary explosion took place in the silo tunnel but the overpressure wave from the explosion kept dislodging more dust in the surrounding area [4]. Powdered and granulated sugar continued to fuel the fireballs and explosion as sugar was thrown into the air by the propagating shock waves [4]. Therefore, it is of utmost importance to understand the formation mechanism of such post-shock dust clouds [1].

1.1. Problem statement

Research in the area of dust explosion indicated that dust lifting caused by primary explosion acts as a catalyst for secondary explosion. It would be advantageous to gain insight into the dust lifting process as well as quantitative parameters to define the process. The dust lifting process behind a propagating shock wave is described in Figure 2. When the shock wave passes over the stagnant layer of dust, it induces velocity into the air medium behind it [5] (Figure 2b). The air, with its induced velocity, starts lifting dust particles, and later on a bigger dust cloud is created [5] (Figure 2c). For simulating a secondary explosion scenario, it is necessary to identify the true governing forces and also other fluid mechanics factors. It is also necessary to identify useful parameters for developing correlations that can be used in industrial-scale simulations. The primary

focus of the current study is to investigate the initial dust lifting process right behind the shock front.

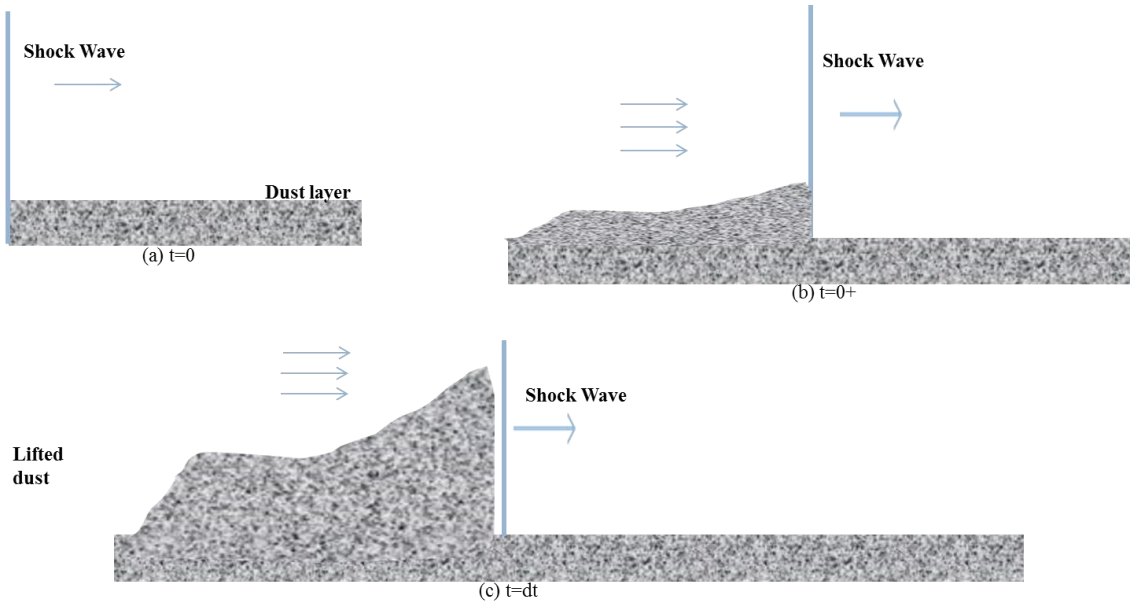

Figure 2: Dust lifting behind a propagating shock wave.

1.2. Methodology of study

The main objective of this research was to gain an understanding of the formation mechanism and parameters affecting the dust entrainment behind a propagating shock front in order to develop more efficient methods to prevent secondary explosion accidents. The chart in Figure 3 summarizes the step-by-step plan of work for the current research topic. The specific tasks to achieve these objectives were:

1. Experimental setup design

2. Study effect of shock strength on the dust entrainment process

3. Study the effect of particle size polydispersity on the dust entrainment process

4. Identify valuable parameters and hypotheses for numerical modelers of this phenomenon.

1.3. Thesis organization

1) Chapter I provides an introduction to the research work, problem statement, and objective.
2) Chapter II documents the necessary background information related to this study. The requirements to obtain a dust explosion and parameters affecting primary and secondary dust explosions are discussed. This chapter provides a review of the fundamental understanding of shock-tube physics and aerodynamic forces responsible for the dust entrainment process. Experimental and computational efforts to understand the formation of a dust cloud for a secondary explosion are also summarized. Finally, the gaps are identified in previous work to determine the objective of this study.
3) Chapter III describes the design and modification of an existing shock-tube facility. A new shock-tube test section for the study of shock wave passage over dust layers was integrated into an existing shock-tube facility. This new windowed test section allows for optical visualization of interaction of a range of dust-layer thicknesses and incident-shock Mach numbers up to 2.
4) Chapter IV presents image and data analysis techniques adopted in the current study. This chapter also includes a methodology for extracting dust-layer height

from the camera images, and typical results for two incident-shock Mach numbers are presented to illustrate repeatability of the collected data.

5) Chapter V documents the study of the effect of shock strength and dust-layer thickness on the dust entrainment process. The main purpose of this investigation was to elucidate understanding of the role of shock Mach number on dust entrainment behind a shock front. This chapter also presents other significant parameters of the dust-lifting phenomenon such as effect of dust-layer depth, delay time, and the effect of moisture content.
6) Chapter VI demonstrates the effect of particle size and polydispersity on the dust entrainment process. Aluminum dust particles with different sizes and polydispersity were subjected to incident-shock Mach numbers of M_s = 1.42. Also, different types of dust particle (limestone, aluminum) entrainment processes were compared. This study also focused on superior ways to express the particle size distribution compared to what currently is used in the industry i.e. median mean diameters (D_{50}) for dust explosion research. The outcomes are of fundamental significance to predict the actual potential of secondary dust explosion hazard while handling different polydispersed samples.
7) Chapter VII goes further in understanding the phenomenon of dust entrainment behind propagating shock waves in light of all the experimental findings. Also, some recommendations are provided for numerical simulation to analyze the dust lifting process.
8) Chapter VIII summarizes the main conclusions from the current research and provides some recommendations for future work.

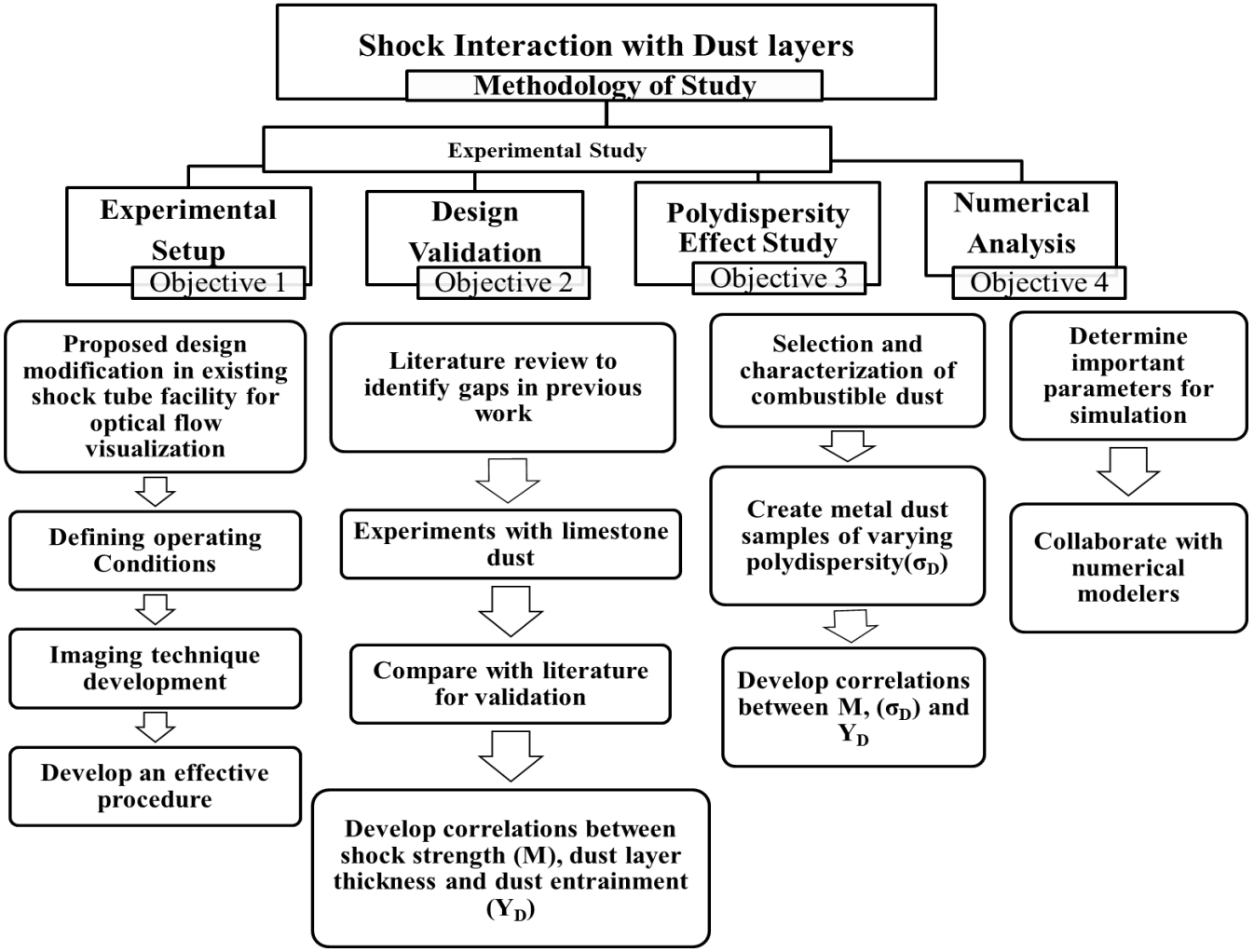

Figure 3: Methodology of the study of shock interaction with dust layers.

CHAPTER II

BACKGROUND AND LITERATURE REVIEW

2.1. Synopsis

In this chapter, a brief background is provided on the requirements to obtain a dust explosion, understanding the parameters affecting primary and secondary explosion, and industrial safety practices to prevent secondary dust explosions. Also, a review of the fundamental understanding of shock-tube physics related to our experiments is provided with supporting figures. The one-dimensional *Rankine-Hugoniot equations* [7, 42, and 45] to determine the shock-tube test conditions in a given experiment are presented. An overview of the aerodynamic forces that govern the dust-lifting phenomenon in air is also provided. Finally, the literature review part summarizes the existing results of experimental and computational efforts to understand the formation of a dust cloud behind a moving shock front.

2.2. Dust explosion

Dust explosion research can be separated into following main regions: formation of dust cloud, ignition and propagation of fire and generation and propagation of pressure wave resulting from dust explosion [6]. There has been extensive amount of research on initiation and propagation of dust fire and explosions. Dust explosion is a rapid combustion reaction where fuel (dust) and oxidizer react to generate oxides and heat [1]. When the dust cloud (fuel), in presence of an oxidizer, comes in contact with an ignition source, temperature of the reactants begins to increase locally resulting in a

combustible reaction. As soon as the heat generation becomes greater than heat dissipation within a specified volume, combustible flame starts to propagate [1]. The flame spreads from the ignition point toward the unburned mixture until at least one of the reactants is consumed [1]. The abrupt generation of heat causes the hot gases to expand, resulting in generation of a pressure wave in a dust explosion [7]. For a dust explosion to occur, we need five elements [8]: (1) combustible dust particles within a size range of 500 µm, (2) oxidizer which often comes from air, (3) external energy source to increase temperature and initiate reaction, (4) suspended dust particles in air creating a dust cloud, and (5) confinement which is needed to increase the pressure buildup during flame propagation. It is the turbulence and confinement that creates explosion when added to a fire triangle as presented in Figure 4 which demonstrates the dust explosion pentagon.

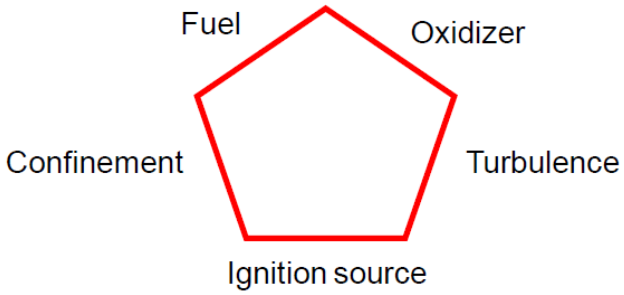

Figure 4: Dust explosion pentagon [8]

The combustion reaction mechanism depends on the physical state of the dust and reaction products. It can broadly be classified into heterogeneous and homogeneous

combustion [9]. Heterogeneous combustion occurs on the solid surface of combustible dust particles which generates gaseous products. A typical example is combustion of carbonaceous dust particles where the reaction depends on the dust surface area where the following reaction takes place: $C(s) + O_2(g) \rightarrow CO_2(g)$ [9].

On the other hand, homogeneous combustion reaction occurs in the gas phase [10]. Organic powders such as sugar, corn starch dust and also polymer powders exhibit homogeneous combustion [10]. In this case, dust devolatizes with the increase in temperature due to pyrolysis and later combustion takes place in the gaseous phase [10].

2.2.1. Primary and secondary dust explosion

A primary explosion can occur in the presence of the five elements of the dust explosion pentagon [8]. While primary dust explosions can be fairly severe, secondary dust explosions can be far more destructive. According to the OSHA definition, secondary explosion takes place if the primary explosion occurs in processing equipment or in an area where combustible dust has accumulated [12]. The pressure wave from the primary explosion can dislodge more dust in the surrounding area. It has been found in the industry that primary explosion damages a primary containment system (such as a duct, vessel, or dust collector) [12]. This secondary dust cloud is of course a bigger fuel source and in contact with an ignition source will result in more severe consequences. The heated atmosphere or the fire from the primary explosion acts as the ignition source for secondary explosion [12]. Figure 5 demonstrates the generation of a secondary dust explosion scenario [11]. The United States Occupational Safety and Health Administration [12] and the U.S. National Fire Prevention Association (NFPA) [13]

have provided guidelines for preventing secondary dust explosions. Some of the significant recommendations are summarized here: Industry should implement proper housekeeping techniques to keep dust accumulation less than 0.8 mm. Proper dust collection system and filters must be used to prevent dust from accumulating. High velocity fans should not be used during housekeeping as this may result in dust cloud accumulation [12-13].

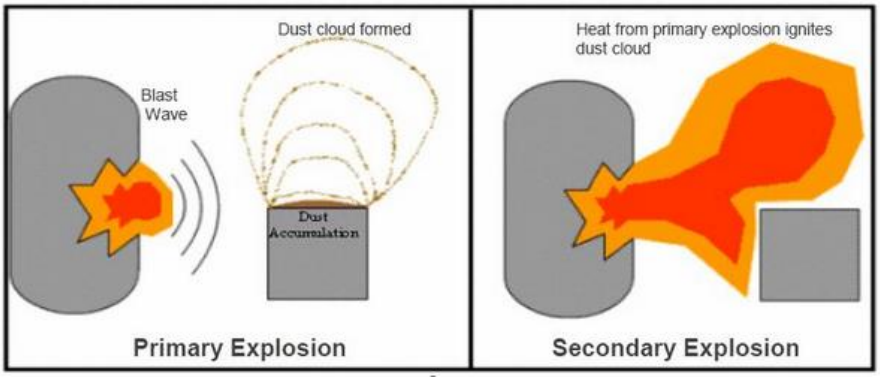

Figure 5: Primary and secondary explosion adapted from OSHA [11]

Though the prevention of secondary dust explosion looks comparatively easy, but still it is a common incident in the industry. The knowledge of the parameters affecting the development of dust layers into dust clouds is crucial to advance current models used to predict the likelihood of secondary dust explosions in the industry [14-15]. For studying shock interaction with dust layers to understand dust cloud formation the most commonly used experimental equipment is a shock-tube. The shock produced in the test device is assumed to resemble a pressure wave created in a primary explosion.

In reality, the pressure waves generated from dust explosion is subsonic [1] (Mach# less than 1). However, in experimental studies in this field, supersonic shock wave generation is common. A typical example of the apparatus for the experimental studies is shown in Figure 6 [16] which represents a schematic of shock-tube with a test section for optical flow visualization. The test section needs to have arrangement for creating a dust layer and synchronize the facility with a high-speed camera to take images of the shock and dust-layer interaction [16].

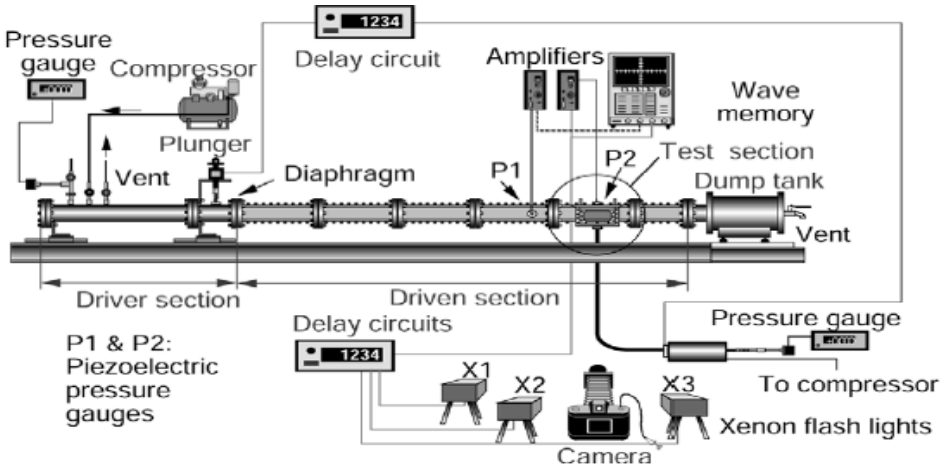

Figure 6: Typical example of experimental setup for studying shock interaction with dust layers [16]

2.3. Shock-tube physics

The shock-tube was first introduced in 1899 [42], and since 1950 it is recognized as a device for measuring different physical phenomena applicable in the fields of physics, chemistry, astrophysics, and engineering [42, 50]. A shock-tube can produce

gas systems or flow conditions with wide range of temperature and pressure that are difficult to attain in other equipment [41]. A shock-tube generally consists of a long tube of constant area [41]. In its simplest configuration, a diaphragm is used to create the separation of two systems at different pressures (Figure 7a). The driver is the shorter section of shock-tube and remains at a higher pressure than the driven section. The longer part of the tube is at a lower pressure and is referred as the driven section [41, 42]. The gases in the high- and low-pressure regime do not have to be the same. Even the temperature in the driver and driven sections can be different. The typical example of diaphragms will be polycarbonates or aluminum plate [44]. With the rupture of the diaphragm, rapid expansion of gas results in the formation of a shock (compression) wave which propagates through the lower-pressure or driven section. However, these gas flow conditions are constructed for very short duration. On the other hand, a train of rarefaction (expansion) waves travels into the driver section [42]. The flow regions induced between the compression and expansion wave are separated by the contact surface. Across the contact surface, pressure and velocity are equal but the density and temperature are different as shown in Figure 8. The contact surface also is the boundary between the driver and driven gases [42]. Therefore, different gases may be present on either side of the contact surface. In Figure 7, different zones are identified. The initial two zones are termed as Zone 1 representing the low-pressure driven section and Zone 4 the high-pressure driver section before rupture of the diaphragm (Figure 7a).

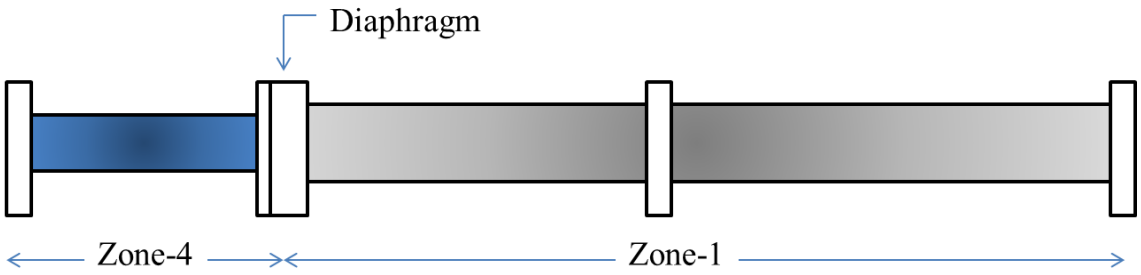

Figure 7: Shock-tube simplest schematic. (a) Showing high- (Zone-4) and low-pressure (Zone-1) sections which are separated by diaphragm of specific critical pressure [Adapted from 42, 45]

As soon as the diaphragm bursts as explained above, a shock wave moves across the driver section, and Zone 2 is the gas system behind the incident shock wave (Figure 7b) [41-42].

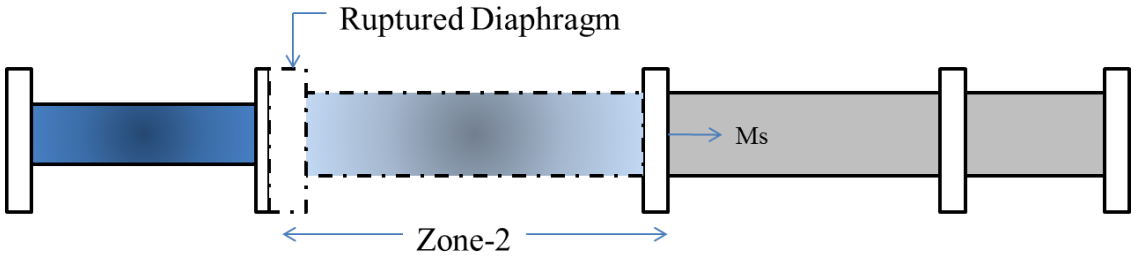

Figure 7: Shock-tube simplest schematic. (b) Showing moving shock front (M_S) which is created by rupturing diaphragm through introducing diaphragm specific critical pressure in Zone-4. Zone-2 is the regime behind incident shock. As a result of sudden breaking of diaphragm, high velocity gas exits Zone-4 forming shock wave and heats and compresses Zone-1 and transfer the area behind shock front to Zone-2 having higher temperature and pressure. [Adapted from 42, 45]

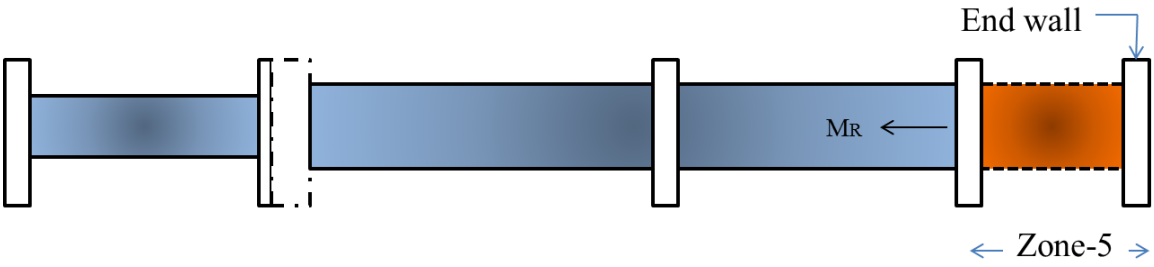

Figure 7: Shock-tube simplest schematic. (c) Showing reflected shock. Incident shock (M_S) travels through the driven section, hits the end wall and returns back as reflected shock (M_R). Zone-5 is the regime behind reflected shock with highest temperature and pressure achieved in the system. [Adapted from 42, 45]

The incident shock wave travels through the driven section and hits the end wall and comes back as a reflected shock. Zone 5 is the gas system following the reflected shock wave [42] (Figure 7c). Zone 3 is the regime between expansion wave and contact surface [42]. The shock strength or Mach number of the incident shock wave as well the reflected shock wave is a function of initial conditions: pressure, temperature, and gas systems present in Zone 1 and Zone 4 before rupture of the diaphragm [42]. In Figure 8, the pressure and temperature in each regime are numbered as the Zone itself. So, P4 is the pressure in Zone 4, etc. With the increase of pressure ratio across the diaphragm (P4/P1), the Mach number also increases [42, 43]. Depending on the physical properties, different driver gases such as air or more commonly used helium and nitrogen will have significantly different Mach numbers for the same pressure and temperature conditions [42].

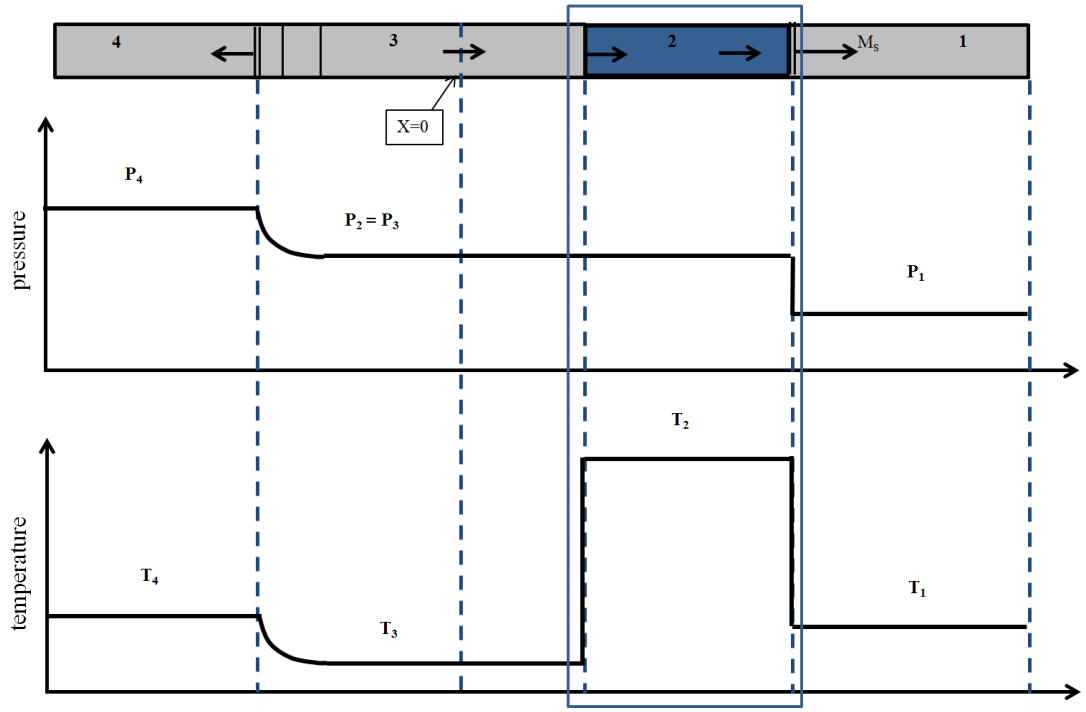

Figure 8: Pressure and temperature distribution in the shock-tube.

[Adapted from 41, 42]

By definition, the shock wave is a strong compression wave, when introduced into a gas system demonstrates instantaneous step changes in different thermodynamic conditions such as entropy, temperature, and pressure. As this adiabatic process involves a major increment in entropy in a very short period of time, the process becomes irreversible. Sound waves travel through a medium via molecular collision. When a shock wave with higher speed than sound in a given medium is introduced, it becomes physically impossible for the surrounding media to respond and change instantaneously. The sound speed in a given medium can be described by the following equation (1) assuming ideal gas law:

$$a_s = \sqrt{\gamma R T_1} \tag{1}$$

The strength of a shock wave is defined by a Mach number, which is the ratio of the speed of a shock wave in a specific medium with respect to sound speed of that medium as shown in Equation (2):

$$M_s = \frac{V_s}{a_s} \tag{2}$$

The Rankine-Hugoniot equations [53-55] are used to forecast the thermodynamic conditions in a shock-tube. Equations (3) through (11) are the ones used for our experimental purpose. These equations are based on the ideal gas approximation [42] - first, the high- and low-pressure section gases obey the equation of state. Therefore, the gas has constant specific heat independent of temperature. Second, all the waves are assumed to be one-dimensional [42, 53-55]

$$\frac{P_2}{P_1} = \frac{2\gamma}{\gamma+1} M_s^2 - \frac{\gamma-1}{\gamma+1} \tag{3}$$

$$V_2 = V_s \left\{ \frac{2}{\gamma+1} \left[1 - \left(\frac{a_s}{V_s} \right)^2 \right] \right\} \tag{4}$$

$$M_2 = \frac{V_2}{a_2} \tag{5}$$

$$\frac{T_2}{T_1} = 1 + \frac{\gamma-1}{2a_1^2} (2V_s V_2 - V_2^2) \tag{6}$$

$$a_2 = \sqrt{\gamma R T_2} \tag{7}$$

$$V_r = -V_2 - \left(\frac{a_2^2}{V_2 - M_s} \right) \tag{8}$$

$$\frac{P_5}{P_2} = \frac{2\gamma}{\gamma+1} \left(\frac{V_r + V_2}{a_2} \right)^2 - \frac{\gamma-1}{\gamma+1} \tag{9}$$

$$M_r = \frac{V_r + V_2}{a_2} \tag{10}$$

$$\frac{T_5}{T_2} = \frac{2(\gamma-1)}{(\gamma+1)^2}\left(\frac{1}{M_r^2}\right)\left(1 + \frac{\gamma-1}{2}M_r^2\right)\left(\frac{2\gamma}{\gamma-1}M_r^2 - 1\right) \tag{11}$$

2.4. Aerodynamics of dust lifting in air

Different aerodynamic forces contribute to the dust entrainment phenomenon. In fact, the dust lifting phenomenon has different governing forces and has diverse modes of lifting [57-59]. Powders demonstrating cohesive behavior have a tendency to be lifted from a surface as agglomerates, whereas none or less-cohesive particles usually are entrained individually [57]. If the dust layer is subjected to uniform aerodynamic conditions, the dust is lifted either uniformly over the entire dust surface or it may start lilting from the leading edge of dust deposit. However, in case of dust explosion the dust deposit is subjected to instantaneous development of different aerodynamic conditions behind the shock front. Figure 9 demonstrates different modes of dust entrainment in air for sand particles for various particle size ranges [57]. One of the common behaviors reported is particles colliding with each other to transfer momentum to the new particles and assist their lifting process. Particles can be lifted for very short periods of time as in the surface creep process or leave the dust layer vertically in a saltation process [58]. No matter which mode of lifting occurs, it all depends on the balancing forces between the forces responsible for dislodging the particle, and the forces accountable for keeping the particle at rest [57-59].

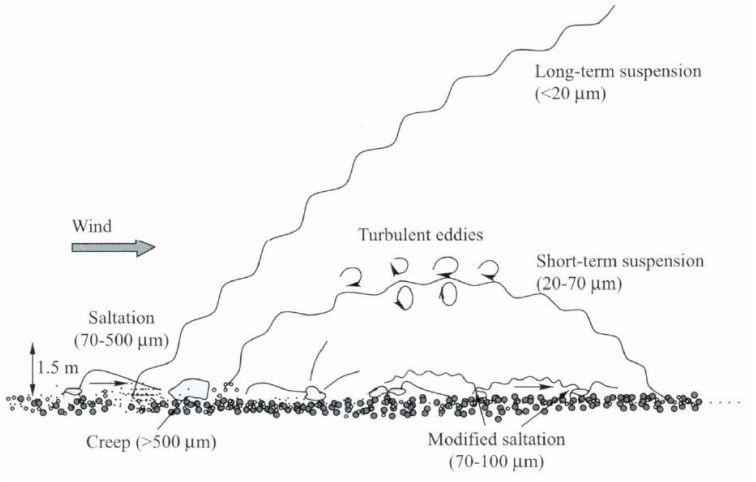

Figure 9: Different type of sand particle lifting phenomenon [57]

Aerodynamic force generally has two components. The force resolved in the direction of air flow is termed as the drag force, whereas the force perpendicular to the dust deposit surface is the lift force [60]. For uniform aerodynamic conditions over a spherical dust deposit layer, the drag force can be expressed as [60]:

$$F_D = \frac{1}{2} C_D \,.\, A \,.\rho\, U^2 \tag{12}$$

Conventionally C_D, A, ρ, and U, represent particle drag coefficient, particle cross sectional area, density and velocity of the air, respectively. For small spherical particles and very low Reynolds number (Re_d) the drag coefficient is known as Stokes drag coefficient. Therefore in Stokes regime (i.e. $1 << Re_d$), the terminal settling velocity of particles can be determined by balancing the drag force and weight of single particle [60] which can be expressed by Eq. (13):

$$U_t = \frac{g.\rho_p.D^2}{18\mu} \tag{13}$$

The terminal settling velocity therefore, for small particles and low Reynolds number (Re_d) depends on particle density (ρ_p), particle diameter (D) and air viscosity (μ). At higher Reynolds number (Re_d) drag co-efficient does not depend on Reynolds number, as a result terminal settling velocity only depends on the size and density of particle [60]. The drag force co-efficient even for a low Reynolds number tends to be very high if the particle is adjacent to the wall [61]. Agglomerated particles have higher terminal velocity compared to monodispersed, spherical particles [62, 63].

Most of the research for understanding the lift force considered spherical particles either rotating perpendicular to the flow direction or when experiencing shear flow [57]. The Saffman force [64] is one of the profoundly accepted lift forces that was calculated for spherical particle subjected to shear flow by the following formula, where ΔV represents the velocity gradient [64].

$$F_{LS} = 1.61.\rho.\sqrt{\Delta V}\sqrt{\nu}D^2.U \tag{14}$$

Cleaver and Yates [65] suggested a lift force for a turbulent boundary layer. Their theory is based on the turbulent burst phenomenon that occurs due to abrupt breakouts in the boundary layer. The calculated lift force in this case can be expressed by the following formula:

$$F_{LT} = 0.76.\rho.\Delta V^{3/2}\sqrt{\nu}D^3 \tag{15}$$

The Magnus force is another type of lift force, which occurs when spherical particles rotate perpendicular to the flow direction and is commonly observed in spinning balls such as in tennis or football [57].

Shock-tubes have been accepted as a beneficial device for investigating aerodynamic dust entrainment. Especially for secondary dust explosion research, as the stagnant dust layer is exposed to blast waves, and an instantaneous air flow behind the shock front takes place. The experimental efforts to understand the aerodynamics of dust lifting behind the shock front is summarized in the following section.

2.5. Experimental study of shock interaction with dust layers studies

For physico-mathematical modeling [17] of dust layer lifting behind a moving shock wave, the initial motion of the dust particles needs to be understood. There have been a considerable number of practical studies reported starting from early 1950 on the interaction of unsteady dust layers with different gas-dynamic waves (*e.g.* shock, compression, expansion). Theoretical studies were carried out by Brown [18] and Prandtl [19]. On the other hand, results from experimental program were first reported by Gerrard [20]. Gerrard investigated the process of lifting of small particles after shock wave passage (particle size 60 μm, Mach # 1.1–1.28, observation time 100 μS). His experimental finding concluded that dust entrainment is a result of the action of a shock wave passing through the dust layer [20]. Borisov et al. [21] also performed experiments to understand the dust dispersion phenomenon and concluded that a compression wave created from reflection from the shock-tube walls that extends through the dust layer is the main reason behind dust cloud formation. Fletcher [5] later on argued both Gerrard's [20] and Borisov's [21] theory. His theory was based on experimental data and numerical analysis. In his experiments, Fletcher used limestone dust for Mach#1.23 and different dust layer thickness. According to Fletcher, dust is lifted by the rapid flow

behind the propagating shock wave [5]. Though Fletcher provided an hypothesis on the lifting mechanism, the governing forces for particle entrainment were still not identified. Many experiments later on focused on identifying the forces responsible for dust lifting.

Bracht and Merzkirch [22] demonstrated experimental and theoretical investigations of dust lifting behind a moving shock front. By assuming thin laminar boundary layer of dust adjacent to shock wave produces high velocity gradient [22]. They concluded Saffman and drag forces contribute significantly to the dust lifting phenomenon. Magnus force was found to have significant effects as well [26]. Also, turbulent mixing of the particles within the air medium behind the shock wave was analyzed using mathematical models [23-25]. Tateuki and Takashi [16] focused on the effect of particle sizes on the lifting phenomenon. In this study [16], organic dust powder of 15, 84, and 300 μm was used for Mach numbers ranging from 1.4 to 1.7 [16]. According to Tateuki and Takashi [16], smaller particles tend to lift faster than large particles [16]. Gelfand et al. [27] used a vertical shock-tube for understanding dust lifting phenomenon, where dust samples were placed at the bottom face of the tube. This experiment pointed out the effects of bulk density of layered particles on the lifting mechanism. In the same study, a horizontal shock-tube was used to understand the shock-tube pressure characterization. Manjunath and Kurian [28] conducted experiments on dust lifting in an air flow behind the shock front in the formulation for higher Mach# 1.92–2.48 and focused on delay time in dust lifting behind the shock wave. Experiments also on the effect of a reflective shock wave were conducted [31].

Table 1. Summary of experimental findings of dust lifting behind shock front

Author /Year	Mach #	Particle size/ layer thickness	Observation time	Significant contribution
Gerrard (1963)	1.1–1.28	60 μm/ 13 mm	0.01 ms	Provided a theory of dust lifting (later criticized by Fletcher)
Borisov *et al.* (1967)	1.3	200–300 μm/ 0.5 and 3 mm sand layer	0.03 ms	Reported wave-like profile in dust cloud surface
Fletcher (1976)	1.23	unknown/6.4 and 9.6 mm limestone	0.03 ms	Suggested dust particles lift due to rapid flow behind shock wave
Bracht and Merzkirch (1978-79)	1.18-1.3	10-50 μm/ unknown	1.2 ms	Identified Saffman force to be a governing force of dust lifting and indicated turbulent mixing in air behind shock front
Boiko *et al.* (1987)	2-3	50 μm / 2 mm organic glass layer	0.04 ms	Studied effect of Magnus force on dust lifting
Tateuki and Takashi (1984)	1.4 -1.7	Organic powder 15, 84 and 300 μm / unknown	0.8 ms	Studied effect of particle size and concluded smaller particles lift higher
Manjunath and Kurian (1991)	1.9–2.48	16.3 μm/3mm dehydrated calcium carbonate	1 ms	Dust entrainment height with respect to dust concentration and delay time with respect to time are reported
Wolnaski *et al.* (2005-2013)	1.3-1.56	Coal 18 μm, silicon 20 μm / 0.1, 0.4, 0.8 mm layer	5 ms	Delay time measurement of dust lifting and working to identify parameters for modeling

Klemens et al. [29, 30] experimentally investigated the interaction of coal dust and silica dust with a shock wave and monitored important parameters such as delay time and the dust concentration gradient behind the moving shock. There have been many other experiments in the same field but with a different objective. Many large scale or industrial experiments focused on identifying detonation characteristics for a dust layer in a shock-tube [32-33] have also been reported. The significant contribution from the above mentioned experiments are summarized in Table 1 [5, 16, 20-28] with experimental variables and observation time.

From Table 1, it can be seen that most of the experiments related to this study had limited observation time. Another very important factor in the current study is high frame speed as that will allow collecting more data within a very short period of time. In most cases, this information was not available from the literature. However, based on the available data it is fair to assume that mostly low-frame speed cameras were used in the previous experiments.

2.6. Numerical study of shock interaction with dust layers

A considerable amount of attention has also been given to the numerical analysis of the dust-lifting process. It should be noted that no mathematical model has been developed which can define every stage of dust entrainment, such as the propagation of wave processes in the very early stage (laminar boundary layer) and the turbulent mixing process and governing forces between different phases [17]. To the best of the author' knowledge, there is also no widely used industrial-scale simulation tool available for modeling dust lifting behind a moving shock wave. Skjold et al. [14]

published a paper on the first version of the CFD code, DESC 1.0, which was used to develop a dispersion model of coal dust behind a propagating shock wave. Additional modeling work on the problem includes those from Fedorov et al. [35, 36], Kuhl et al. [37] and many among others [38-40]. Most of the numerical analysis related to the previous study consider either Eulerian-Eulerian (E-E) or Eulerian-Lagrangian (E-L) approach for two phase modeling [66-68]. Navier–Stokes equations are used for describing gas phase and solid (dust) phase is expressed using Euler equations in E-E framework [68]. Both phases are coupled by considering the effect of aerodynamic forces resolved on a solid particle in the gas system. In the E-L approach, the gas phase is expressed similarly as the Eulerian framework. However the dust particles in this case are treated as points, whose movement is the product of the impact of the gas phase [69]. Using an Eulerian framework for computation, the results of Houim and Oran [34] trended well with data obtained from our experimental findings at M=1.4 (which are discussed in detail later).

Another popular approach is direct numerical modeling. In this case, the Navier Stokes equations are solved around each particle considering all the governing forces [68]. All this mathematical modeling is very rigorous, hence the idea of having specific correlations for dust lifting (solid phase) have gained interest in current studies [67]. However, not much progress has been made in developing correlations for dust lifting behind a shock front. The only current application is noted in DESC 1.0 [14] which has used an in-house developed correlation to develop the CFD model. But the author [14] reported that the tool is not ready for industrial-scale simulation. The specific

correlation is applicable only for coal dispersion and can only be used when the particle velocity is known. In our current facility, we do not have scope of laser scattering which is needed for particle velocity measurement to validate their existing correlation. One of the main challenges of the correlation development according to the authors was no repeatability of the data obtained, which causes a huge uncertainty. Also, the correlation has been used only by a research group [14]. Since no publication on an updated version of DESC is available currently, further information could not be provided.

2.7. Gaps in existing information

Though there have been experiments to understand the aerodynamics of particle lifting in uniform aerodynamic conditions, comparatively there are very limited experimental studies of dust lifting behind a shock front, which is necessary in secondary dust explosions investigations. From the extensive literature survey, some significant gaps in the existing information have been identified.

- The entire phenomenon of dust propagating behind a moving shock is yet unknown.
- No systematic study available to develop correlations that could be used for developing industrial scale simulation tools for secondary explosion hazard assessment.
- Attempts to study the effect of particle size [16] on dust entrainment have been carried out. However, particle size measurement was obtained for different material with different sizes which provided valuable information but neglected

the effect of properties of individual dust samples. Therefore, the particle size effect needs to be studied using the same dust with different particle sizes. Also to the best of our knowledge, there is no experimental investigation that addressed the effect of polydispersity on dust lifting behind a moving shock front.

- From the literature survey, it is evident that not many experimental works have been carried out in recent years using modern techniques such as high-speed cameras which give more data than earlier studies. As most of the studies in this field generated fewer data for very short experimental time period, no conclusion on the boundary layer phenomenon have been derived. The occurrence of turbulent mixing and the possibility of the presence of turbulent boundary layer have been mentioned [23]. As a result, no numerical model is able to portray all stages of the dust lifting phenomenon, including shock wave propagation, possible turbulent mixing, and precise features of force interaction of the phases.

In summary, it is evident that a conclusive model to accurately simulate the entrainment process is yet to be developed. For preventing or controlling dust fires and explosions, the simulation of the secondary explosion scenario is necessary. Accordingly, it is vital to study the dust-lifting process experimentally and recognize parameters that will be valuable for the development and validation of numerical predictions of this phenomenon.

CHAPTER III

DESIGN AND MODIFICATION OF SHOCK-TUBE FACILITY

3.1. Synopsis

This chapter describes the shock-tube design modification strategy undertaken to develop the facility for current study. A new test section was designed and built for the present application, utilizing an existing shock-tube as the core facility. The key features of the new test section are the inclusion of a large-windowed region and the ability to quickly change the bottom dust layer. This chapter provides necessary details on the existing facility and later discusses the design modification performed. The necessary shock wave and facility characterization while developing specific experimental procedure for current studies are mentioned at the end.

3.2. General description of the facility

The existing shock-tube is made of 304 Stainless Steel, and it has a 1.86-m-long driver section which is circular in cross section (7.6-cm diameter). The driven section is approximately 10.8 cm square and 4.1 meters long. This shock-tube was ideal for modification as the driven section has a squared cross section. Details on the original facility can be found in Rotavera [45] and Rotavera and Petersen [46].

3.3. Design modifications

To this existing shock-tube, a new test section was introduced. As the main purpose of this test section is flow visualization, it has windows on the top, left, and right sides. The port and starboard windows are each 5.1×30.5 cm. With the strength

limitations of a large window in mind, the new test section was designed to handle incident-shock velocities up to Mach 2 with an initial pressure of 1 atm (101.3 kPa), and it is capable of holding pressures up to 15 atm (1.52 MPa) behind the reflected shock wave. Higher Mach numbers are achievable with initial pressures below 1 atm. Conditions behind the reflected shock wave determine the upper bounds on allowable shock strength. The possibility of a dump tank being added in the future would allow even greater shock strengths, if necessary. A schematic of the proposed modification to the shock-tube is provided in Figure 10, where the insertion of dust plate and new plumbing scheme is mentioned. Based on this modification strategy, we developed the test section, and Figure 11 shows a photograph of the modified shock-tube facility with the new test section. It has an easily removable dust pan inserted at the bottom surface of the windowed test section, with a dust deposit area of 6.9×27.3 cm. The dust pan can be adjusted to provide various dust layer thicknesses in 3.2-mm increments, between 3.2 mm and 12.7 mm. Figure 12 shows an image of the test section focusing on the dust pan with adjustable inserts.

The separate vacuum manifold was installed to protect the present facility from the negative effects of fine dust particles. Vacuum manifold consists of a roughing pump, exhaust vent, an analog and digital pressure measurement. When the shock-tube pressure gets to atmospheric pressure, the vacuum pump eliminates post-experiment gasses from the shock-tube. Further details on the shock-tube hardware and related procedures can be found in the thesis of Marks [44]

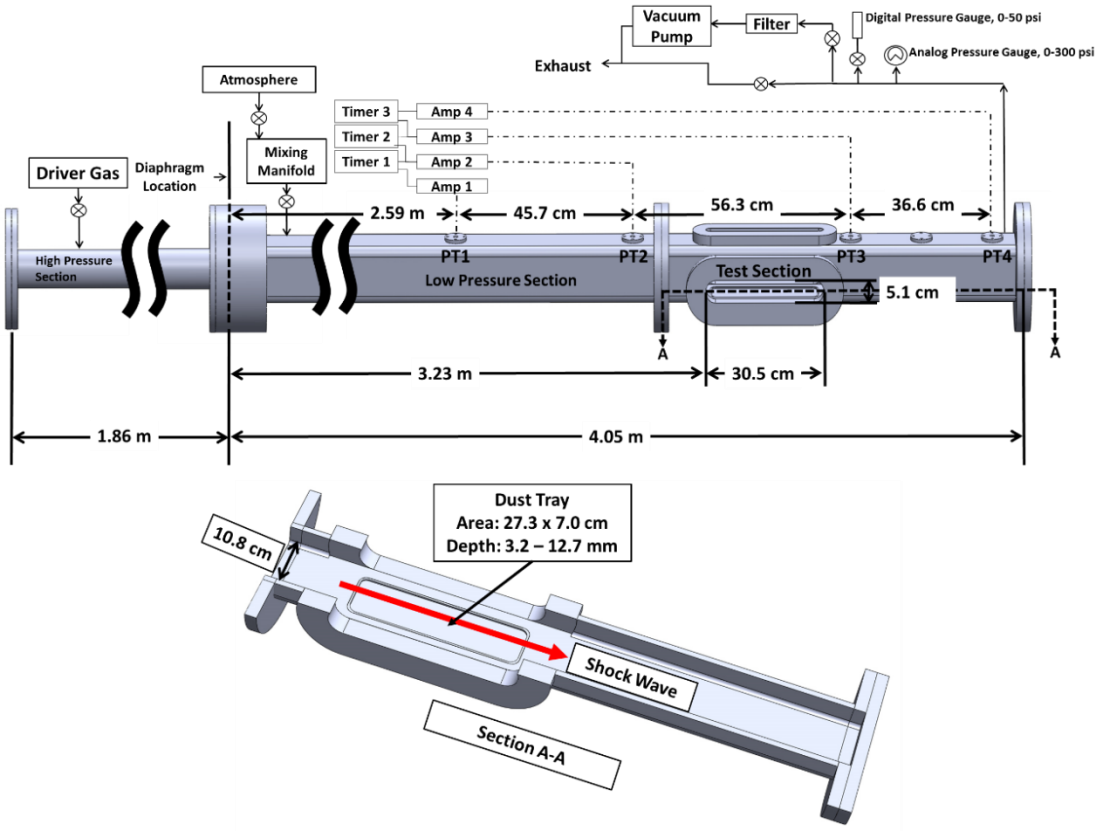

Figure 10: Shock-tube schematic (top) showing new plumbing, relative distances, test-port location, pressure transducers (PT), velocity-detection timers, and section-cut of new dust-layer test section (bottom).

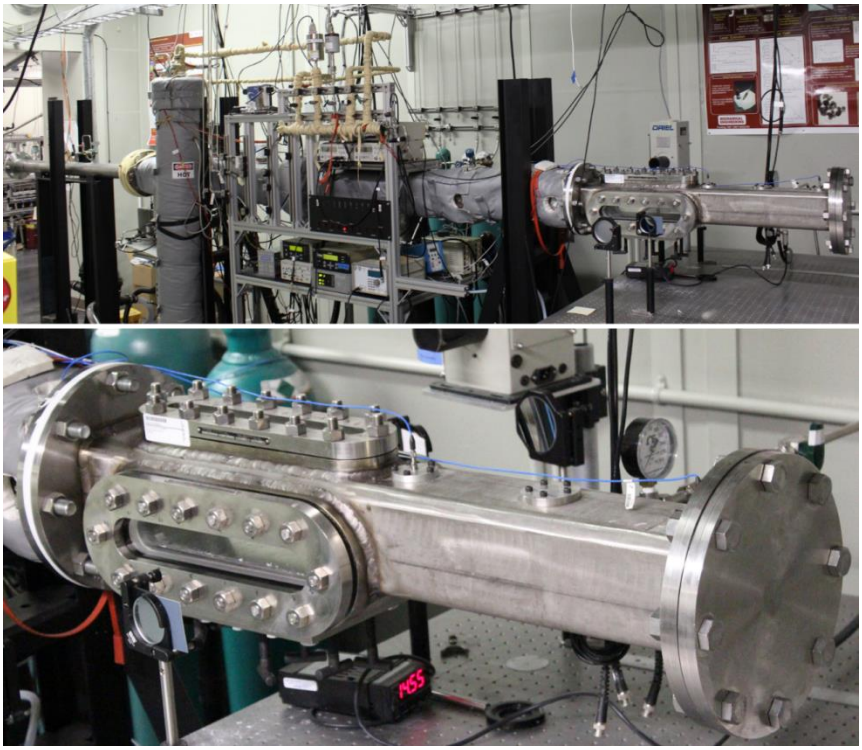

Figure 11: Photographs of complete shock-tube and test setup (top) with new dust-layer test section (bottom).

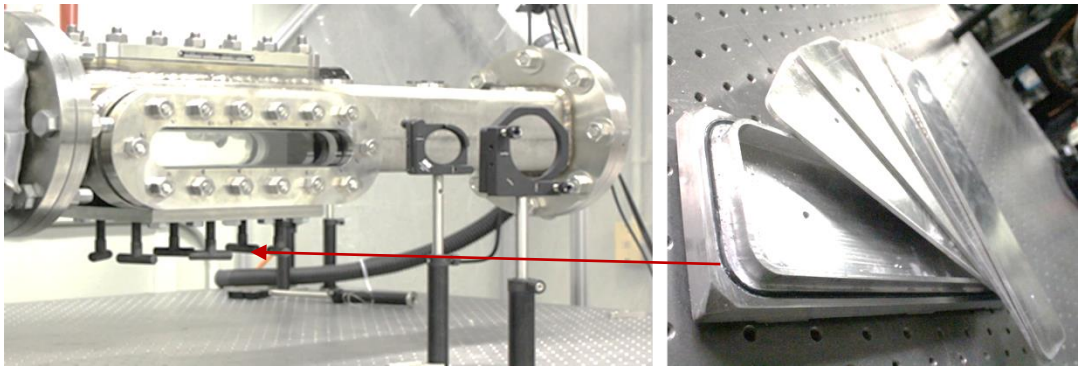

Figure 12: Photographs of the shock-tube test section (left) and unassembled dust pan hardware (right).

3.3.1. Optimum location for test section

Consideration was given to maximizing the test time for observing the passage of the shock wave over a dust layer. That is, the arrival of the reflected shock wave and the contact surface for experiments up to $M_s = 2$ were estimated during the design process using 1-D wave diagrams (Figure 13.), where M_s is the incident-shock Mach number. The optimum position was calculated based on maximum observation time between incident shock- contact surface crossing and reflective shock-contact surface crossing. For incident shock wave of Mach 2.0 the current facility has an observation time of 2.79 ms.

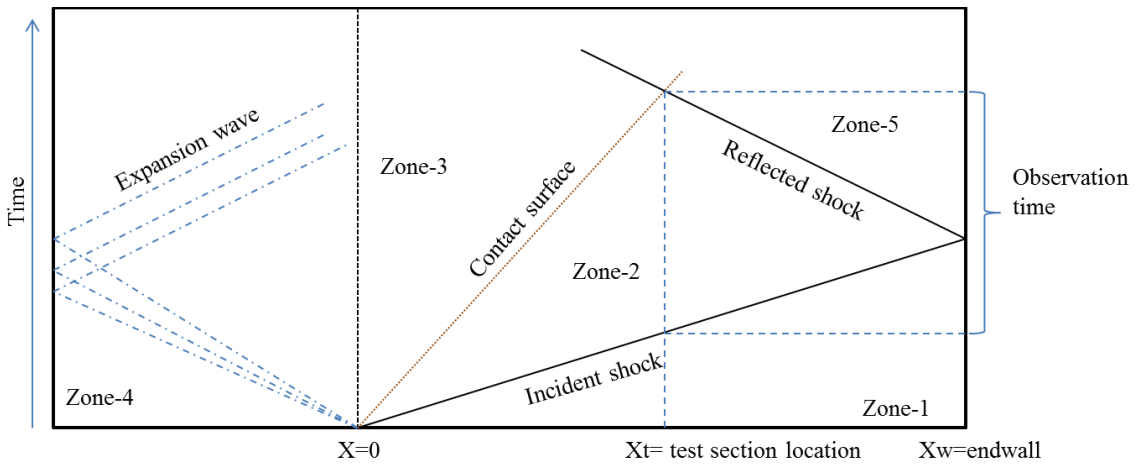

Figure 13: X-t diagram showing ideal propagation of compression and expansion waves after rapture of diaphragm for optimum test location determination. [Adapted from 41, 42, and 43]

As mentioned in shock-tube physics discussion, Zone-2 is the region behind the incident shock wave and for the current study our area of interest. In order to get longer experiment time, the optimum location determination calculation was based on maximum presence of Zone-2 from X-t diagram. From the *Rankine-Hugoniot equations* [53-55] the following formula can be generated:

$$t = \frac{\frac{V_r}{V_s}+1}{\frac{V_r}{V_2}+1} \quad w \tag{16}$$

$$t_o = \frac{X_w - X_t}{V_s} + \frac{X_w - X_t}{V_r} \tag{17}$$

Where X_t and t_o represent optimum test location and longest experimental time, respectively. For our experiments, the maximum Mach number required was $M_S = 2$. Therefore, applying equation (1, 2, 4, 5,8,16 &17) the optimum location was determined. The calculated observation times for $M_S = 2$ and $M_S = 1.3$ are 2.8 ms and 3.4 ms, respectively at the chosen location.

3.4. Facility characterization

Perhaps the most important independent variable in these experiments is the incident-shock velocity, ultimately specified as the Mach number. The shock velocity is determined by a series of piezoelectric pressure sensors (PT1 through PT4) connected to three timing gates (Fluke PM6666 counters) in between each sequential pair of transducers, depicted schematically in Figure 10. Of the three timing intervals, one is before the dust-layer test section, one span the test section, and one is after the test section. The first pressure transducer is also used to trigger the camera to begin recording (discussed in details on the imaging diagnostic). The resulting velocity,

determined from each $\Delta x/\Delta t$, is taken to be the average velocity over the particular interval, or in other words the local velocity is assumed to correspond to the midpoint axial location between two transducers. Knowledge of the incident-shock velocity at the location of the test section is critical to the present experiments. By running shocks with and without a dust layer present, the effect the dust layer has on shock velocity may be observed, and such tests were also part of the facility characterization. Figure 14 shows two typical results for the measured three velocities.

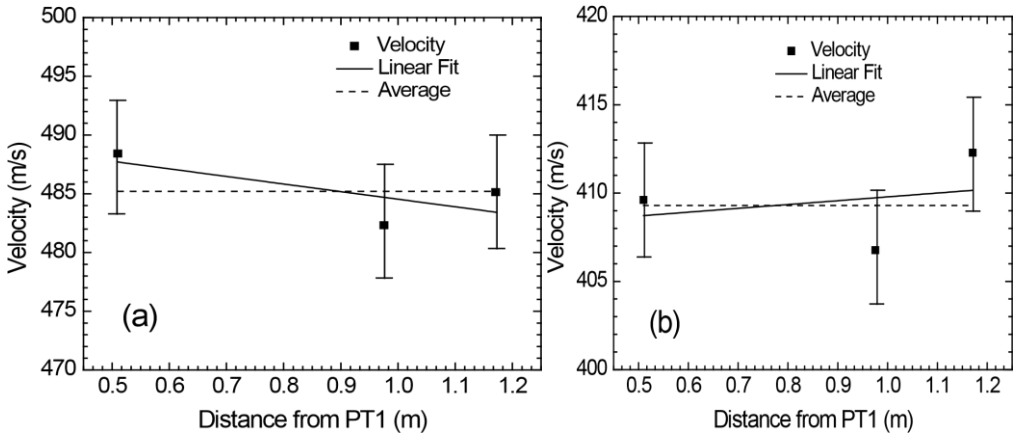

Figure 14: Typical measured velocity profiles across the windowed test section. The three velocities correspond to the intervals between PT1-PT2, PT2-PT3, and PT3-PT4, respectively (see Fig. 1) (a) velocities with dust, for M_s = 1.41, P_2 = 1.4 atm. (b) velocities without dust, for M_s = 1.19, P_2 = 0.98 atm.

In general, there are three main observations taken from the facility characterization experiments for the shock velocity: 1) the overall variation in the shock velocity over the 3 intervals is not large, and typically within about 3 m/s of each other;

2) the middle velocity is always lower than the first and third velocities; and, 3) the overall trend of the velocity as the shock moves downstream over the test location is to decrease, although this is not always the case. For example, Figure 14a exhibits an overall (but slight) decrease with axial distance, while Figure 14b shows an overall (slight) increase with distance. It should be noted that the basic characteristics of the axial velocity profiles seen in Figure 14 remain mostly unchanged in the new test section whether a dust layer is present or not. In fact, Figure 14a is with dust, while Figure 14b is without dust. Note that the slight increase in velocity for the case in Figure 14b without dust is not indicative of the usual trend for all cases without dust; either trend in shock velocity is seen whether the dust is present or not and, if anything, seem more dependent on the magnitude of M_s, with the higher M_s tending towards producing slight decreases across the test section. The lower velocity in the test section is a facility artifact, and is a repeatable trend with or without dust or a dust tray present (flat plate). From a microscopic perspective, Figure 15(a) with dust shows a slight lag in the shock front at the dust-wall interface, where Figure 15(b) without dust shows a relatively flat front at this same interface. The apparent reduced shock velocity at the wall with dust reveals an interaction between the shock and dust layer, however, the shock speed at the center of the shock-tube, where shock-position measurements are made, appears to be unaffected. Pressure measurements taken at the opposite surface (top) of the dust tray have a flat, dust-free interface, yielding accurate measurements for macroscopic shock speed determination. These microscopic and macroscopic phenomena do not affect the time-dependent dust height measurements with the image processing techniques

described herein. Dust-wall interactions reveal interesting phenomena that should be studied in great detail for ranges of M_s and dust layer thicknesses.

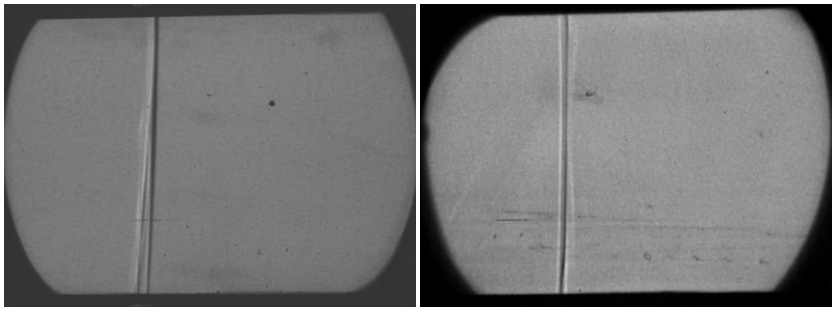

Figure 15: Typical shock with (a) with limestone dust (b) without limestone in dust tray at M_s = 1.24.

As seen in Figure 14, the variation in shock velocity across the test section is small enough so that there is little difference between either a linear fit or an average value for all three positions. As a result, the final velocity value that is assigned as the M_s for a given experiment is therefore taken on a case-by-case basis and is usually either an average of all three velocities or the center velocity (the latter when one of the timer boxes does not trigger properly). Nonetheless, the variation in velocity across the test location is within the uncertainty of the velocity measurement itself and within the variation amongst the three velocity intervals, which in any case is relatively small. The end result is that the stated velocity of the incident shock wave when propagating over a dust layer has an overall, estimated uncertainty of ±1.2% (or about ±5 m/s). This velocity uncertainty corresponds to a variation in stated Mach number of ±0.013 – 0.019 for the range of M_s of interest herein (typically for M_s between 1.1 and 1.6). This overall

uncertainty in M_s takes into account any slight variation across the test location (Figure 14) as well as the uncertainty of the measurement system in detecting the arrival of the shock wave at each transducer port.

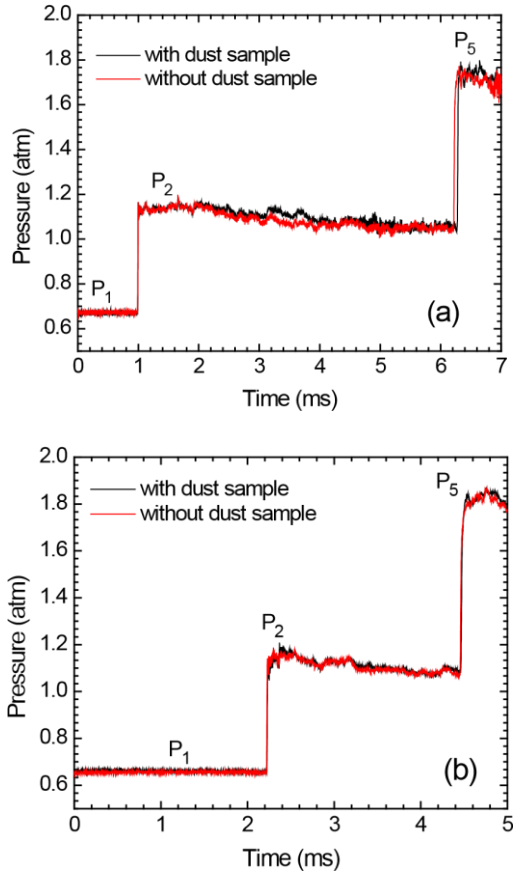

Figure 16: Measured pressure time histories upstream and downstream of the test window and with and without a dust layer present. Plot (a) shows the result for the transducer immediately upstream of the window, and plot (b) is for the transducer downstream of the window. Test conditions are M_s = 1.32 in air.

Also of interest is the stability of the test conditions for the duration of the experiment, prior to the arrival of the reflected shock wave at the test section. Figure 16 shows typical measurements from the pressure transducers located immediately upstream and downstream of the windows, both with and without the presence of the dust layer. One trend is that there is no noticeable difference in the pressure time histories with or without the dust layer, indicating that the dust seems to have little if any effect on the test pressure (and hence temperature and induced velocity as well). The second observation is that the test pressure (P_2) is relatively stable, but typically with a slight decrease with time. Even with this decrease, the pressure varies no more than about 8% for the examples shown Figure 16, which are representative of the conditions of interest in this study. Of course, since the pressure measurements in Figure 16 were located at the opposite (i.e., top) wall from the dust layer, it would be of interest to (in future tests) monitor the pressures along the lower wall, closer to the dust layer and the corresponding holding plate.

3.5. Shock wave characterization

For the current experiments, shock waves with M_S ranging from 1.1-1.6 were generated using nitrogen as the driver gas. Table 2 summarizes all the thermodynamic conditions and obtained/calculated parameters used in current study for each specific shock wave. Calculations for the parameters are in the Appendix.

Table 2. Thermodynamic conditions and calculated parameters for current study

Driver/ Driven	Diaphragm thickness	V_s (m/s)	M_S#	P4 (atm)	P2 (atm)	P5 (atm)	V_2 (m/s)	T5 (K)
N_2/air	10-fold-Al foil	365	1.1	0.68	.54	0.76	33	319
N_2/air	0.005” LEX	427	1.24	2.04	1.07	1.68	124	388
N_2/air	0.01” LEX	457	1.32	4.76	1.23	2.21	164	421
N_2/air	0.02” LEX	488	1.42	7.48	1.42	2.86	204	457
N_2/air	0.03”+0.02” LEX	549	1.6	16.33	1.83	4.46	278	532
He/air	0.005” LEX	580	1.68	2.38	0.83	2.19	314	571
He/air	0.005” LEX	670	1.96	2.04	.559	1.79	412	693
N_2/N_2	0.005” LEX	429	1.23	2.38	1.04	1.61	120	382
N_2/N_2	0.02” LEX	498	1.42	10.5	1.46	2.95	210	461
N_2/N_2	0.03” LEX	536	1.53	10.67	1.69	3.85	257	507

3.6. Safety analysis of new facility

As the existing facility was not used previously for experiments handling dust particles, during design modification special consideration was given to a new plumbing scheme for ensuring safe removal of dust from facility. Also, a safety analysis on the project was performed to ensure safety while running the experiment. For example, for introducing windows in a shock-tube attention was given to pressure testing the new windows. All components, except for the glass windows, have a minimum safety factor of 2 based on a designed operating pressure of 1.48 MPa (215 psig). The glass windows

are rated to 1.6 MPa (230 psig) and include the manufacturer's own safety factor. The shock-tube test section was hydrostatically pressure tested to 1.6 MPa (230 psig). The maximum experimental operating pressure within the tube will be 1.03 MPa (150 psig) which is only ~65% of the rated pressure and of the hydrostatic test pressure. Only inert driven gas and inert dust combinations were used during dust experiments to prevent unwanted combustion and associated pressure rise. For introducing combustible dust into the system, both the driver and driven gases used were oxidizer free (such as nitrogen/nitrogen system shown in Table 2). After the completion of the project safety analysis, an experimental procedure was developed.

3.7. Operating procedure development

One of the challenges with handing dust samples in a shock-tube is the cleaning process after each experiment. As high pressure is created, after each experiment dust particles travel in every direction, and the entire shock-tube needs to be cleaned every time or else dust residue from previous experiments will contaminate the next experiments. Cleaning of the shock-tube every time is very time consuming and physically challenging. Therefore, the procedure was developed carefully to have an efficient operating procedure.

i. The first step is **dust layer preparation**. Preparation of the dust layer involves removing the bottom plate, selecting the proper layer height, and filling the depression with the powder. Figure 17 shows the test section located at the end of the shock-tube where the dust is leveled coincident with the incident shock wave path.

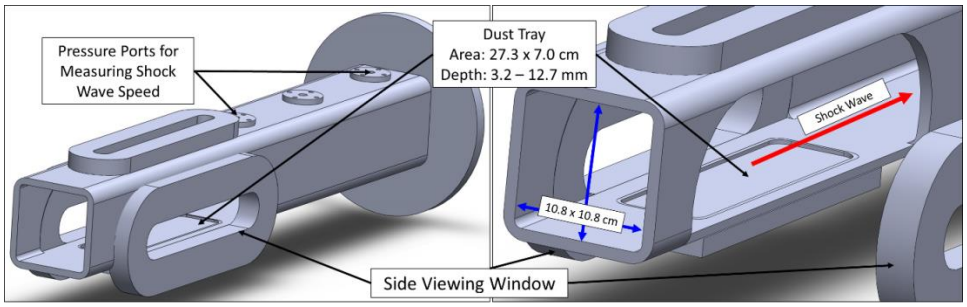

Figure 17: Assembled shock-tube end (left) with side viewing window removed (right) revealing the depressed, variable-depth dust tray.

The dust tray is depressed 3.2 mm below the shock wave path, and its depth can be varied for further studies. Care is taken to create a uniform layer while minimizing compaction. The present methods lead to high test-to-test repeatability in the results.

ii. After replacing the sealing and fixing the bottom dust pan to the shock-tube, the next step is to install diaphragm of specific thickness (as discussed in Table 2) into the breach loader and make sure the driver and driven section are sealed completely.

iii. Next, the high- and low-pressure sections are vacuumed simultaneously, the driven section is evacuated to at least 0.7 kPa (5 torr) using a vacuum roughing pump.

iv. After achieving the desired vacuum in both regions, the driven section is filled with air or nitrogen (depending on what type of dust is used for the experiment) to the desired initial pressure P1. For our experiments, we tried to keep this variable constant at around 66.67 KPa (500 torr) (shown in Table 2) to replicate

atmospheric condition during dust entrainment behind a shock front. When the desired P_1 is attained, all the connecting lines to the driven section are sealed.

v. The next step is to reset the three timing gates (Fluke PM6666 counters) and ensure the camera/light source is set up and triggered.

vi. The driver section which was being vacuumed till this point must be pressurized to the desired pressure P_4 by filling with nitrogen/helium until the diaphragm raptures. As discussed in shock-tubes physics with the increase of P_4/P_1 the shock strength M_s increases.

vii. With the rupture of the diaphragm, rapid expansion of the gas results in the formation of a shock wave which propagates through the driven section. As a result, the dust layer from the dust pan starts to disperse. This phenomenon is captured in the shadowgraph images. For our image analysis purposes, the recorded shadowgraph images need to be saved in ".avi" and ".bmp" format. Also, the counter recordings should be documented to calculate shock speed.

viii. Prior to moving to the next step, at least five minutes rest time needs to be provided for settling dispersed dust particle. Even after giving enough time there will be airborne particles dispersed in the shock-tube, therefore plumbing carefully is very important. The shock-tube pressure needs to be monitored at this point utilizing analog pressure gauge installed at the exhaust manifold. In almost every case for our experimental condition shock-tube pressure at this stage remains below 1 atm. The pressure is further lowered using vacuum pump to

almost 5 torr to extract any remaining suspended dust particles from the previous test gases. By filling air, the shock-tube is brought back to room pressure next.

ix. Then the diaphragm breech loader is opened to collect the used diaphragm. The diaphragm needs to be inspected as improper breaking of the diaphragm will have an impact on shock generation. This has impact on repeatability of the experiments.

x. The following task is to take out the endwall from the shock-tube. A powerful vacuum cleaner is then used to extract as much of the dust as possible. Currently we are using a vacuum cleaner with a three-stage filtration process. For lab-scale dust explosion research, it is necessary to use HEPA filter as it can filtrate almost 99.97% of airborne dust particles with a minimum size of 0.3 μm. We added a long telescoping pole to the vacuum cleaner hose to reach the entire driven section which is 4.1 m long. When vacuuming combustibles dusts such as aluminum, special attention was given to make sure the vacuum cleaner grounding is proper. The dust can create a combustible cloud inside the vacuum cleaner, hence have potential explosion hazard. Therefore, while vacuuming, the dust cloud needs to be diluted at regular intervals with inert dusts such as limestone dust.

xi. We also use a duster, and again added a long telescoping pole to remove dust deposits from the shock-tube walls. Basically the duster loosens the dust particles stuck on the wall. Therefore, next we need to vacuum again the driven section to remove the loose dust particles.

xii. Most of the time after following the above cleaning procedure, still the windows need to be cleaned with acetone, or residue caught up in the window become visible in shadowgraph. Therefore, we need to remove the dust pan to gain access to the interior window.

xiii. For runs with high Mach numbers (M_s = 1.32-1.6) the residual dust reaches the very end of the driven section as well as the high-pressure section. Figure 18 shows how having residue dust impacts the shadowgraph images. Both images are of an incident shock. In this case, often after following all the above mentioned steps of cleaning, still huge amount of residue remains in the tube. Figure 18 (a) clearly demonstrates the residual dust is travelling from either high pressure/driver section or at least the other end of driven section, which is difficult to reach using a vacuum cleaner even with a long telescoping pole.

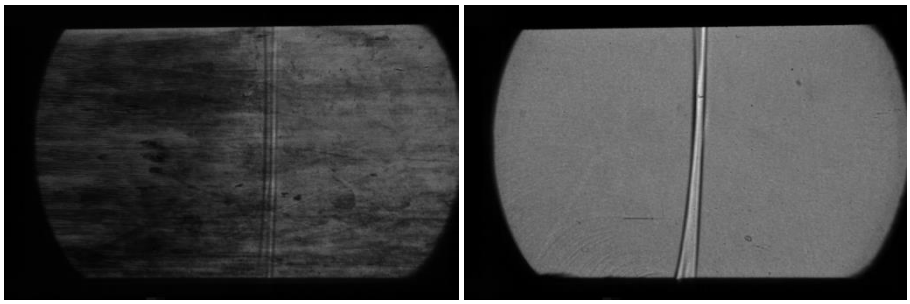

Figure18: Incident shock wave image (a) when there is residual dust (b) without the presence of residual dust.

xiv. Hence in case of higher shocks we decided to run dry shocks in between each experiment. Dry runs are repeating the same experimental procedure without

having dust introduced in the system, basically following steps (ii to xiv). This has been very effective. Because the shock brings all the dust from the driver section to closer vicinity for cleaning from the open endwall. When the dust is at close vicinity, it can be cleaned following our procedure above.

xv. After completing all the steps, the experimental setup is ready for another test run following steps (i) to (xiv).

CHAPTER IV

DEVELOPMENT OF IMAGE AND DATA ANALYSIS TECHNIQUE

4.1. Synopsis

A new test section (window) for the study of shock wave passage over dust layers was integrated into an existing shock-tube facility. A shadowgraph imaging technique with high-speed camera is installed into the new setup to capture images of the shock front and dust dispersion behind that moving shock. This chapter discusses the image analysis technique in detail, focusing on the methodology used for extracting data of dust-layer entrainment height from the shadowgraph images by using typical results for two incident-shock Mach numbers (1.23 and 1.32) as examples.

4.2. Optical setup and procedure

A basic shadowgraph technique was employed for flow field visualization. The shadowgraph technique [70,71] allows one to observe the density difference and therefore the shock. For our experiment, it was necessary not only to visualize the dust entrainment process but also the shock wave itself. Identification of the shock wave is necessary to understand the true delay time of the dust lifting process as well the end of the experiment. This is as soon as the reflected shock wave is visible in the frame. A schematic of the shadowgraph arrangement in relation to the test section is shown in Figure 17. Two windows on both sides with an approximate viewing area of 76 mm wide by 50 mm high are used for applying the shadowgraph imaging technique, whereas

the top window gives the possibility of using laser scattering [73] and other laser-imaging techniques in the future.

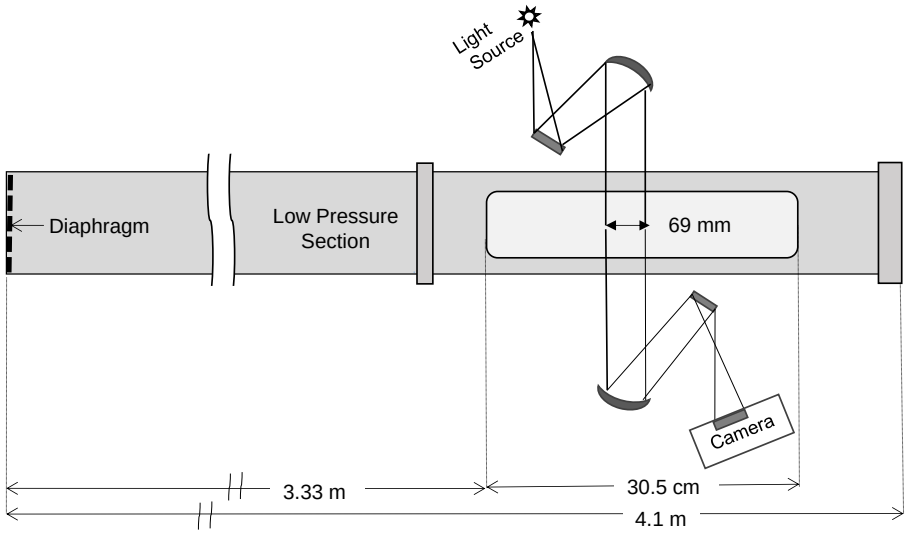

Figure 19: Schematic of shock-tube facility showing the windowed test section on the driver side for studying shocks over a dust layer and the relative placement of the shadowgraph optical setup.

The schematic in Figure 19 has some detail dimensions of the driver section as well as the newly installed side windows. The parabolic and flat mirror arrangement to establish a shadowgraph imaging technique is also portrayed in Figure 19. Width of the captured images is controlled by the concave mirror diameter. The curved mirrors have a 76-mm diameter and 44-cm focal length, resulting in F # of 5.8. Along with the focusing and guiding mirrors, a Photron Fastcam SA1.1 high-speed camera (with 15,000 frames per second) and an Oriel 70-W Hg-Ze lamp was used as the light source. This framing

rate provides a 67-μs time difference between each image. The camera was set to an image area resolution of 768×576 pixels.

To understand dust-layer entrainment into the post-shock gas flow, particle lifting is typically measured with respect to time or with respect to the shock-wave propagation. For each experiment, images are captured of the air and dust-layer interaction behind the incident shock wave. A typical image sequence of the dust-air interaction behind a shock wave of Mach number of 1.32 is shown in Figure 20.

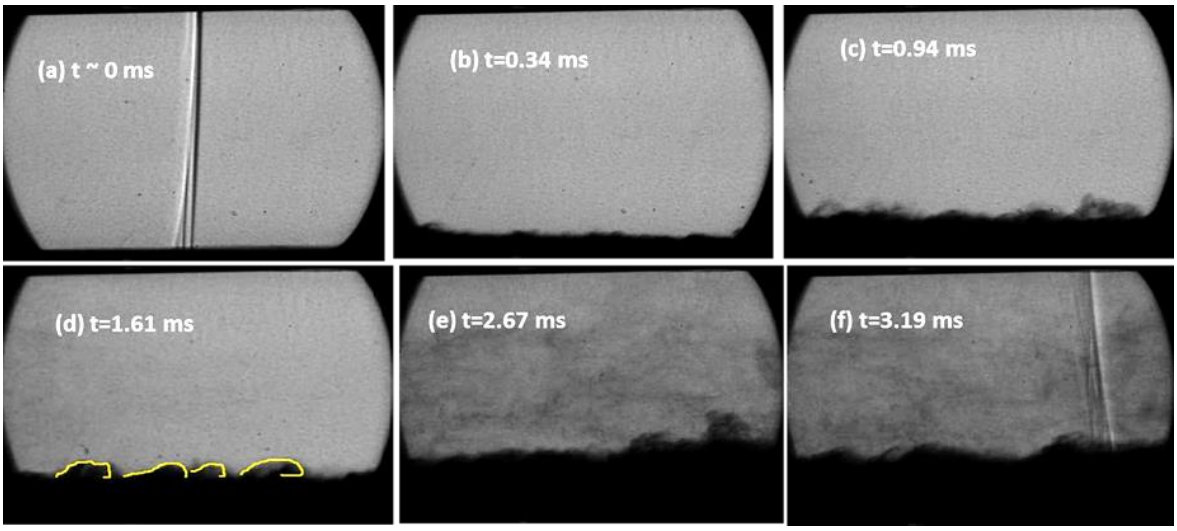

Figure 20: Images of air and limestone dust interaction in the flow behind a shock; M = 1.32. All captured images were for 15,000 frames per second with a 1-μs exposure time.

It can be observed that a normal shock wave is followed by the subsequent movement of the dust layer in the vertical, or y, direction. Note that the shadowgraph method provides very good resolution of the boundary between the edge of the bulk dust

layer and the gas above it, particularly for the earlier portion of the experiment. As seen in the latter frames in Figure 20, the edge of the dust layer becomes more turbulent, with obvious eddies or ripples forming on the surface. In Figure 20 (d) typical eddy structures are highlighted in yellow just to show this common turbulent trend. Eventually, as seen in the last frame of Figure 20, the reflected shock wave arrives at the test section, and the data acquisition portion of the experiment is concluded. The dust height in the y-direction can be compared with shock wave propagation past a reference horizontal location [44]. Dust height as a function of time is determined by examining the shadowgraph images, as described in detail in the following paragraphs. The corresponding shock wave propagation was derived from the shock velocity and time recorded by the camera using a known camera trigger location, which in the present tests is the pressure transducer immediately upstream of the window, PT2 in Figure 10.

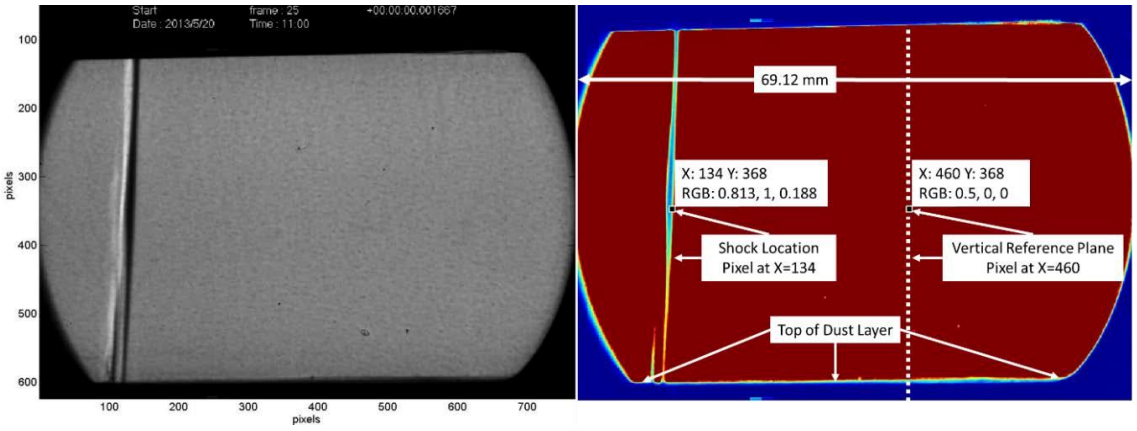

Figure 21: Incident shock wave with M_s = 1.32; raw indexed image (left) and RGB image (right) with RGB pixel values at vertical reference plane and shock wave.

Figure 21 shows the initial image of the incident shock wave entering the test section and traversing the top of the depressed dust layer. The initial and subsequent images taken during the experiments were analyzed frame-by-frame for spatially and temporally dependent dust measurements. Image analysis was performed by an in-house MATLAB code designed to examine pixel-to-pixel variation and to identify the location of dust-air boundaries and shock waves. A user-created MATLAB add-on application, Image Measurement Utility [47], was used to calibrate the distance of each pixel in the image setup.

Figure 22 presents a typical calibration image taken with a pair of digital calipers opened to 10.00 mm. A calibration line was drawn between the measuring edges of the calipers, and with a known 10.00-mm distance, a pixel calibration of 0.09 mm/pixel was established. Once this procedure establishes the image calibration, point-to-point calculations of post-shock dust-layer height can be accurately made.

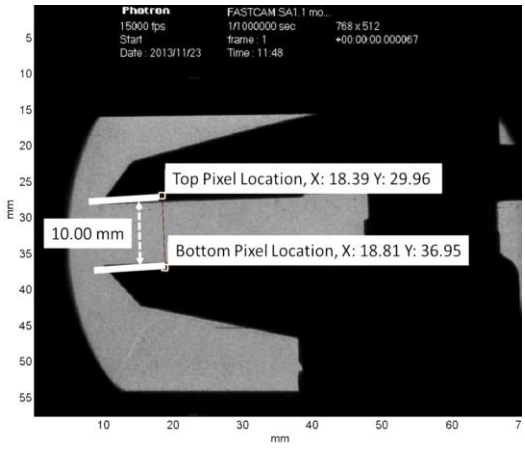

Figure 22: Image-Pixel calibration using calipers and the MATLAB Image Measurement Utility.

To discern and measure a clear dust-air boundary for recording dust-height variation, the images are converted from raw, indexed values to RGB. Pixel RGB values are examined to set thresholds correlating to shadowgraph density gradients. In Figure 21, the incident-shock image is used to establish a fixed vertical reference plane at X = 460 to measure the fixed vertical height of the viewing window bottom and distance to the shock wave. Subsequent images continually measure dust heights from the vertical reference plane. The RGB image shown in Figure 21 identifies the shock wave above a zero (0) threshold for green and blue pixel color values, as compared to the zero (0) green and blue values in the constant-density air located in the space between the shock wave front at X = 134 and the vertical reference plane. The number of pixels at a constant height of Y = 368 are counted between the shock wave and vertical reference plane, and with a pixel calibration of 0.09 mm/pixel, shock wave distance is determined. The image frame rate, measured shock speed, and measured distance allow a precise time to be calculated to determine when the shock wave passes the vertical reference plane. As frames were 66.7 microseconds apart for a 15,000 fps rate (~3 ms total test time), the post-shock images were corrected by the elapsed time between the shock wave passing this plane and subsequent time stamped images. For example, a M_s = 1.32 wave presents an elapsed time of 90.9 microseconds, which is a typical value.

The left image in Figure 23 identifies a pre-shock horizontal reference plane at Y = 596, relative to which all subsequent dust-height measurements are referenced. This plane corresponds to the viewing window bottom and was identified to terminate in air at a zero (0) threshold blue pixel color value, as compared to the space between the

image bottom and the horizontal reference plane. The right image in Figure 23 is post-shock dust which is rising at the fixed vertical reference plane and above the horizontal reference plane, which is 1.45 mm above the top of the dust layer. The zero (0) threshold blue pixel value is used on most of the subsequent images to identify the dust-air boundary and to record dust-height measurements with time. Ultimately, the uncertainty in the determination of the dust layer edge is within one pixel, since the RGB contrast goes to zero very dramatically at the dust-air boundary. Therefore, the stated uncertainty for the dust height Y is ±0.09 mm.

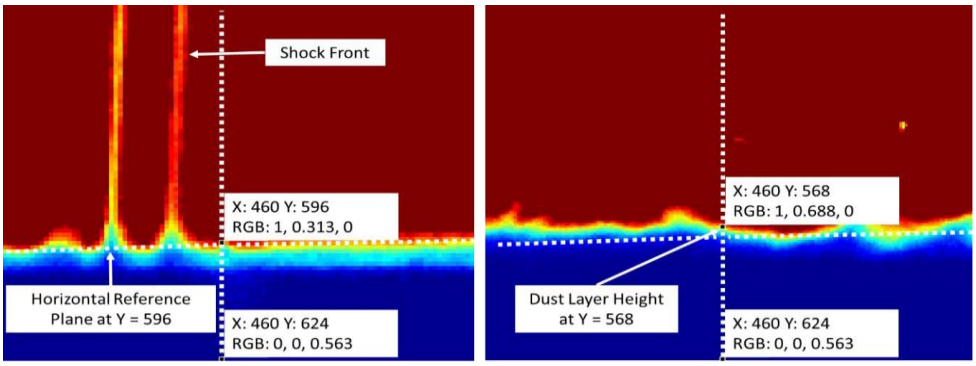

Figure 23: Pre-shock horizontal reference plane (left) and post-shock dust height measurement (right) with RGB pixel values at horizontal reference plane and dust-air boundary.

In some cases at longer observation times, a background dust cloud can enter the observation area, increasing the uncertainty. This cloud is thought to be caused either by residual dust deposits on the shock-tube walls from previous experiments being lifted and carried into the observation area, or from enhanced mixing between the dust layer

and surrounding air. This uncommon event is addressed by slightly modifying threshold values to account for increased sensitivity in density variations. This adjustment provides an accurate representation of the boundary between areas that were filled with dust lifted from the initial dust layer, and those which are composed of background dust. Data are presented as the dust-layer height rises with time at the vertical reference plane, with height = 0 at the horizontal reference plane (window bottom), and time = 0 when the shock wave reaches the vertical reference plane.

4.3. Data analysis

In the prior section, Figure 20 shows images of air and limestone dust interaction in the flow behind a shock; M_s = 1.32. Applying the above described image analysis technique data was generated from the captured shadow images. Figure 24 shows the relation between the generated data and physical phenomenon of dust lifting process.

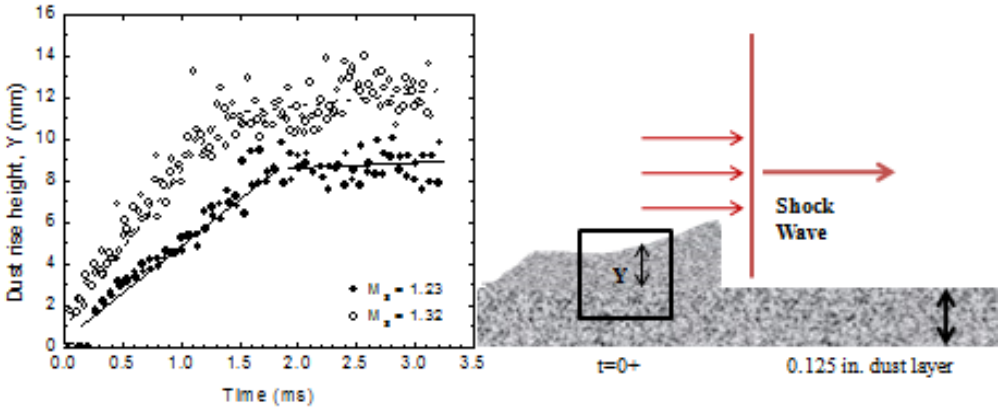

Figure 24: (a) Results for measured dust layer height, Y, as a function of time for two different M_s (1.23 and 1.32). The trend lines are present for convenience in highlighting the two growth regimes. (b) Dust lifting behind shock front.

For the 3.2-mm limestone dust layer depth, data were collected for shock Mach numbers of 1.23 and 1.32. The time evolutions of the dust surfaces are plotted in Figure 24(a) for each of the two shock speeds to also compare the influence of Mach number. In both Figure 24(a) and (b) the positive y-axis is measured vertically upward. Note that the bottom surface of the image does not correspond precisely with the lower wall of the shock-tube (and, hence the top edge of the dust layer). Rather, the y=0 in the images are 1.45 mm above the dust layer initial height. Dust rise height in the positive y-direction can be associated with shock wave propagation past the reference x-location. From the measurements taken, of which those in Figure 24(a) are representative, several observations can be made which highlight the kind of data that can be obtained with the new facility. The data processed from the images can be discerned within about ±0.09 mm, and the data show high test-to-test repeatability. Some factors that may add to the existing uncertainty and temporal variation include the dust erosion. That is, as time passes, more and more dust is removed from the dust pan and the surface level changes. Subtle differences in the creation of a uniform dust layer and particle agglomeration prior to each experiment also limits higher repeatability as the dust's spatial distribution can vary amongst layers prepared for different experimental runs, and this variation can be difficult to quantify. Despite these factors, the results presented show very good repeatability (Figure 25), and clear growth-rate trends are discernible.

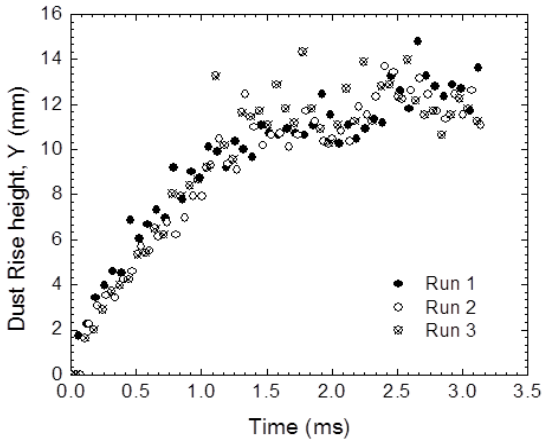

Figure 25: Repeatability of experimental results for M_s = 1.32. Three experimental runs are shown on the same plot.

To identify the validity of in-house developed MATLAB code, obtained results are compared with data points attained using a user-created MATLAB add-on application, Image Measurement Utility [47]. With this utility tool the bitmap images were analyzed frame by frame which is very accurate but very time consuming. Figure 26 (a) presents the comparison of data obtained by developed MATLAB program and manual analysis using measurement tool. The results demonstrate very good matching. In our study, we used a fixed vertical reference plane to measure the fixed vertical height of the viewing window bottom and distance to the shock wave. Subsequent images continually measure dust heights from the vertical reference plane. Figure 26 compares the data obtained by choosing one vertical reference along the x-axis with multiple reference points on the x-axis where data are obtained by averaging total reference points. Figure 26 (b) identifies there is no significant difference in the results.

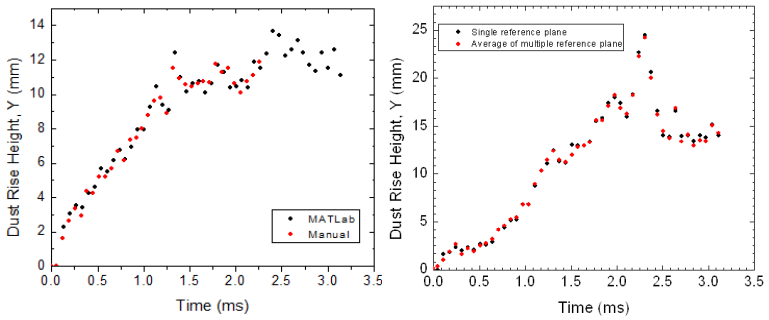

Figure 26: (a) Comparison of obtained data using in-house developed MATLAB code and user created measurement tool (b) comparison of data obtained with single reference line and multiple reference point.

One of the reasons behind choosing only one fixed vertical plane is that we only capture shadowgraph images of a small portion of the window. Therefore, we basically want to understand the trend and have repeatable data. Since we were not covering the whole window anyway with our current optical setup, we believe having a single reference plane is sufficient.

CHAPTER V

EFFECT OF SHOCK STRENGTH AND DUST LAYER THICKNESS ON DUST ENTRAINMENT PROCESS[1]

5.1 Synopsis

In this chapter, detailed study of the effect of shock strength and dust layer thickness on the dust entrainment process behind a propagating shock wave is discussed. Limestone dust was subjected to Mach numbers ranging from 1.10 to 1.60. Tests were performed with two different layer depths, namely 3.2- and 12.7-mm thicknesses. Details on the experimental variables and dust sample characterization relevant to this study are provided. The obtained shadowgraph images were analyzed using the image analysis technique described earlier. In the later section of this chapter, detailed analyses of the obtained data are provided to elucidate the impact of shock strength and dust layer thickness on the lifting process. New correlations were developed between the shock strength and the dust entrainment height as a function of time for each layer depth. In summary, the results herein are in agreement with trends found in previous work, where there is a linear relationship between dust growth rate and shock Mach number at early times after shock passage. Also, new data were collected for image analyses over longer periods than found in prior works, where the longer observation time and higher camera framing rates led to the discovery of trends not previously observed by earlier studies,

[1] Reprinted with permission from "Effect of shock strength on dust entrainment behind a moving shock wave" by A. Y. Chowdhury, H. G. Johnston, B. Marks, B., S. Mannan, and E. L. Petersen, Journal of Loss Prevention, Copyright [2015] Elsevier

namely a clear transition time between the early, linear growth regime and a much-slower average growth regime. This second regime is however accompanied by surface instabilities that can lead to a much larger variation in the edge of the dust layer than seen in the early growth regime. In addition, for the linear growth regime, there was no significant difference in the dust-layer height growth between the two layer thicknesses; however, the larger thickness led to higher growth rates and much larger surface instabilities at later times.

5.2. Operating conditions and experimental variables

The experimental variables of interest for the present study included operating pressure, dust-layer thickness, and strength of the shock wave, *i.e.*, the incident-shock Mach number, M_s. For all experiments; the initial driven section pressure was maintained at 67 kPa (500 torr) via the shock-tube vacuum manifold using the facility roughing pump. This particular driven-section pressure level provided an optimum value that led to efficient production of the shock speeds (via driver-to-driven pressure ratio) and near-atmospheric conditions while still being within the safety limits of the large windows in the test section (to keep the reflected-shock pressure under 500 kPa). Nitrogen was used as the driver gas for convenience. Different shock wave velocities were achieved by using polycarbonate and aluminum diaphragms of various thicknesses. The diaphragms were broken by filling the driver section until the diaphragm bulged and was punctured by a cross-shaped cutter immediately downstream of the diaphragm. This procedure has been used in the authors' laboratory for many years and produces repeatable shock speeds with minimal material contamination. For this study, the shock

Mach numbers ranged from 1.1 to 1.6. The operating conditions are summarized in Table 3. Different dust pan inserts were used to achieve two dust-layer thicknesses, namely 3.2 and 12.7 mm. For the experiments described in this chapter, the pressures (P_2) behind the incident shock wave for M_s = 1.1, 1.23, 1.32, 1.4, and 1.6 were 0.07, 0.106, 0.126, 0.143, and 0.19 MPa, respectively. For the 12.7-mm depth, the highest shock Mach number used herein was 1.56.

Table 3: Operating conditions for experiments with limestone dust

Driver/Driven Gas	Diaphragm Thickness (in)	Variables	T1 (K)	P1 (torr)	Mach #
N_2/Air	Al-foil (10 fold)	Dust Layer Depth 0.125 in 0.5 in	295	500	1.1
N_2/Air	0.005 (LEX)		295	500	1.23
N_2/Air	0.01 (LEX)		295	500	1.32
N_2/Air	0.02 (LEX)		295	500	1.4
N_2/Air	0.02+0.03 (LEX)		295	500	1.6

5.3. Dust sample characterization

All of the experiments (in this chapter) used limestone dust samples. Past explosions in coal mines were reportedly caused by methane detonations [74, 75], which led to shock waves propagating over coal dust in surrounding areas. Current methods to mitigate explosive atmospheres involves the spreading of limestone in these areas to create an inert mixture if such an accident were to occur, therefore limiting the possibility of a secondary explosion [75,76]. The new facility described herein uses

limestone to present measured dust dispersion, as its density is near coal and its actual presence in the hazardous area. A Beckman coulter counter was used to determine that the average particle size was 4.2 microns. Figure 27 displays SEM images of the limestone dust particles used in the experiments described herein.

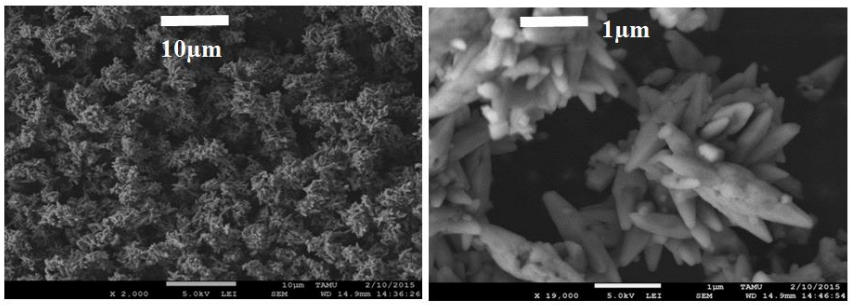

Figure 27: SEM Images of a limestone sample at two different resolutions.

Average particle sizes closer to the measured value of 4 microns are evident in the image, with some agglomerations of approximately 20-30 microns, which may affect dust lifting height in contrast to a homogenous 4-micron mixture. For each experiment, an appropriate amount of limestone dust was used to fill the entire depth of the removable dust tray. Excess dust was gently removed using a straightedge so that the dust surface was flush with the inner wall of the shock-tube. No intentional compaction of the dust within the tray was performed. For 3.2-mm dust-layer depth on average, approximately 20 grams of limestone in the 60 cubic centimeter dust pan was needed. For 12.5-mm dust-layer depth, approximately 75 gm of the dust sample was required.

This gives roughly compaction densities of 0.33 and 1.25 g/cc for the 3.2-mm and 12.5-mm depths, respectively.

5.4. Analysis of shadowgraph

The edge of the optically thick dust cloud was identified using the pixel red, green, and blue (RGB) intensity details of which are in the image analysis chapter. The precise definition of the lifted height is the maximum raised height where the dust cloud is optically thick for detection. Figure 28 shows a typical image sequence, starting from the top left corner; for this particular experiment, the depth of the limestone dust layer was 12.7 mm, and the shock Mach number was 1.32 (In image analysis discussion similar shadowgraph images for another dust layer thickness was demonstrated).

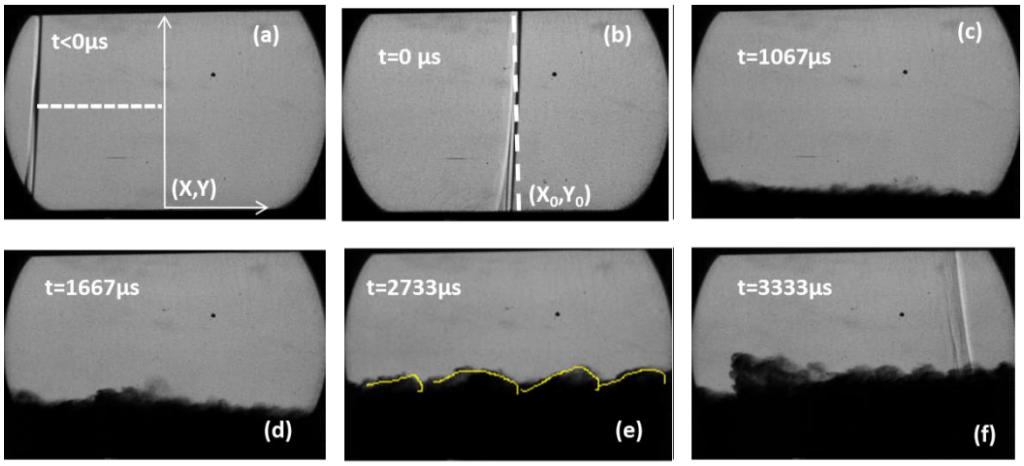

Figure 28: Typical images of air and limestone dust interaction in the flow behind a moving shock wave in the shock-tube facility. M_s = 1.32, 15,000 frames per second, dust-layer depth = 12.7 mm.

From the images shown, which are typical for the tests herein, it is observed that the normal shock wave is trailed by the subsequent movement of the limestone dust layer. Image data are analyzed until the reflective shock wave is visible in the image, as in the bottom right corner in Figure 28(f). Figure 29 shows example RGB images of the shadowgraph data shown previously in Figure 28. In Figure 29c, unambiguous identification of the rising dust cloud boundary is demonstrated.

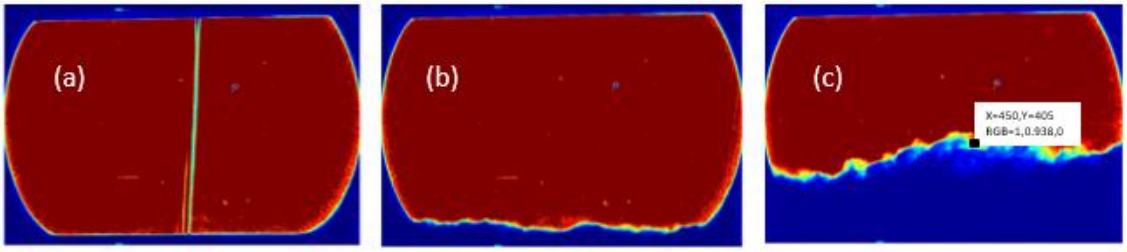

Figure 29. RGB images of air and limestone dust interaction behind a moving shock wave (M_s = 1.32). Such images are used to determine the edge of the dust layer in each frame, as described in the text.

From analyzing the shadowgraph images, the presence of a delay time between shock wave passage and dust lifting was evident. In the presence of dust, the shock wave curvature at the bottom was also very interesting. From the overall analysis, dust lifting from the adjacent bottom wall strongly proposes a boundary layer phenomenon, which is discussed in detail after analysis of the data.

5.5. Effects of shock strength and dust-layer thickness

Given in this section are the results of the experiments outlined above. The rate of the dust height rise is presented first for both dust-layer thicknesses, and correlations of this rate as a function of M_s are given. In the latter part of this section, the dust rise delay times are discussed. The 3.2-mm limestone dust was subjected to normal shock waves of the following M_s: 1.10, 1.23, 1.32, 1.40, and 1.60. Figure 30 is the graphical representation of the time evolution of the dust layer at different Mach numbers for this smaller dust-layer depth. For each shock speed in Figure 30, the data points represent the measured dust layer height over the time period shown for at least 2 and in most cases 3 different tests. The data scatter therefore represent a combination of the turbulent nature of the turbulent surface layer (discussed more below) and test-to-test variation (*e.g.* powder compaction, repeatability of diaphragm bursting, measurement of M_s). Within the current experimental data, it was observed that the rate of dust rise increases with increasing Mach number. For a few sample trials, the growth rate for all but $M_s = 1.10$ occurred in two stages: a linear regime of higher growth, followed by a regime of lower average growth but increased dust surface variation. These results for the linear, first regime are in agreement with trends found in the literature [5], namely with respect to the effect of M_s on increasing growth rate. However, this trend does not appear to hold true for shock Mach number of 1.32 and 1.40 from the tests herein. The rise rate and overall rise height at both Mach 1.32 and 1.40 are nearly identical (Figure 30). However, an increase in rise rate is observed as the Mach number increases between $M_s = 1.10$ and 1.32. Further experiments at the higher Mach number of 1.60 were performed to observe

whether or not M_s =1.32 is a threshold limit for dust entrainment rise height for the 3.2-mm depth. However, for M_s = 1.6 the general trend of increasing dust rise rate with increasing shock Mach number was again observed. Three tests were performed at both M_s = 1.32 and 1.40 with similar results; the reason for the similar results at these two M_s could not be determined at this time, but this trend did not prevent successful correlation of the general trends with M_s, discussed next.

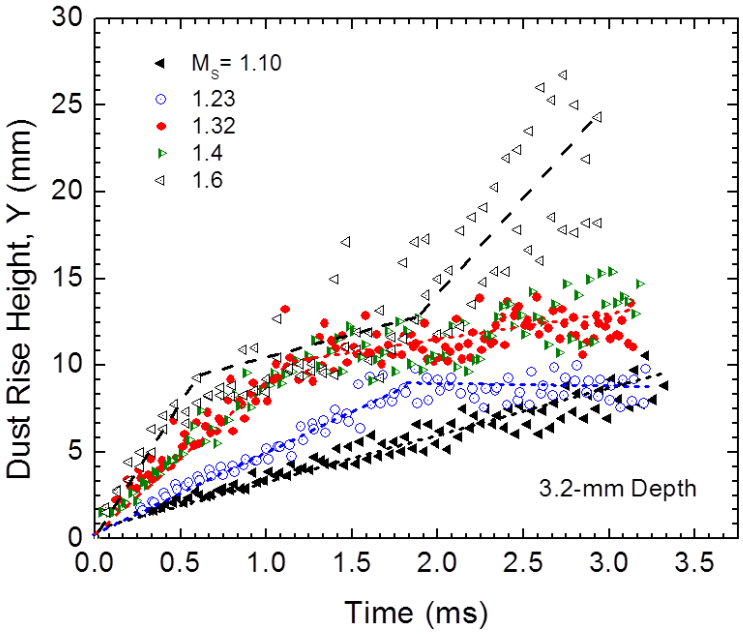

Figure 30: Time dependent dust rise height for various Mach numbers for a dust-layer depth of 3.2 mm. Dashed lines are guidelines to emphasize the average trends. The data symbols for each M_s represent up to three different experiments at each condition.

A linear correlation was derived for the slope of this initial dust layer rise and is plotted for the various Mach numbers in Figure 31a; this figure provides valuable information for the early growth regime where the dust height linearly increases with time for different Mach numbers. For times after the dust-layer rise delay time, τ, and the regime transition time, t_{tr}, the dust height Y follows a linear trend

$$Y = \alpha t \quad (\text{for } \tau < t < t_{tr}) \tag{18}$$

Table 4 summarizes the resulting α values for each M_s. Hence, the curves in Figure 31a represent Eqn. 18 for the different shock speeds, to accentuate the Mach number trend (note that the delay times τ are not shown in Figure 31a).

Table 4: Experimental results for various dust-height parameters for different M_s and the two layer depths studied (3.2 and 12.7 mm). The slope dY/dt is defined in Eqn. 18, and the delay time τ is the raw delay time including the 1.45-mm blind zone.

	3.2-mm Depth			12.7-mm Depth		
M_s	t_{tr} (ms)	dY/dt (mm/ms)	τ (ms)	t_{tr} (ms)	dY/dt (mm/ms)	τ (ms)
1.10	2.32	2.42	0.28	2.82	3.50	0.78
1.23	1.99	4.33	0.27	2.70	5.44	0.37
1.32	1.18	7.39	0.11	2.23	9.11	0.31
1.40	1.21	7.06	0.06	1.70	9.46	0.11
1.56	-	-	-	1.37	12.4	0.20
1.60	0.47	11.4	0.07	-	-	-

To better identify the time at which the dust layer stopped rising linearly for each test, the absolute value of the difference between the linear prediction and the observed data was plotted and is shown in Figure 31b. In this way, Figure 31b can be used to identify the transition zone by accentuating the deviation from linear behaviour for different shock strengths.

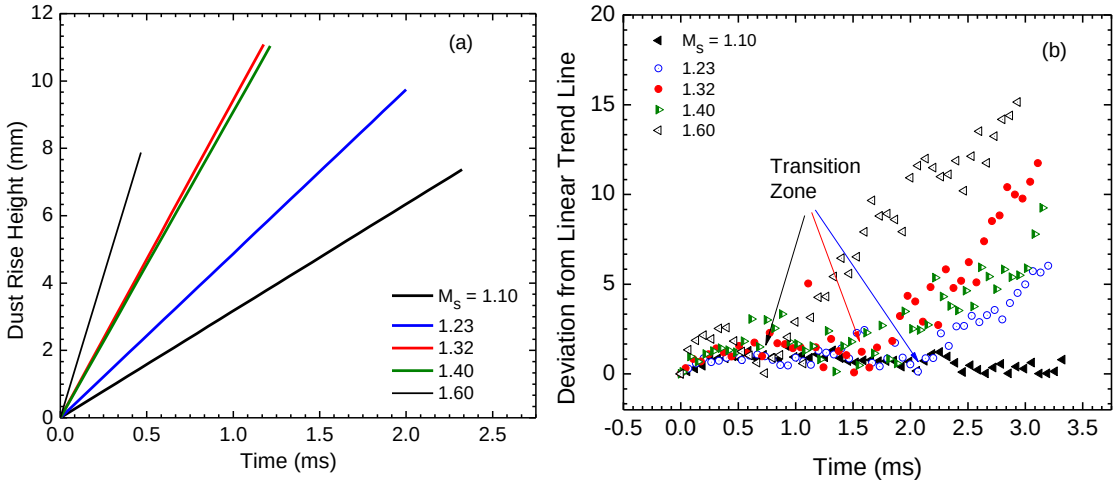

Figure 31: Detailed analysis of the 3.2-mm dust-layer depth results. (a) Initial (linear) rate of dust layer rise as a function of Mach number from Eqn. 18; values for α are in Table 4. (b) Deviation of dust rise height from the linear trend prediction versus time for various Mach numbers. The transition time t_{tr} between the initial, linear regime and the second regime becomes clear on such as plot, as shown.

This post-shock time at which the regime changes is defined herein as t_{tr}. Values for t_{tr} at each shock speed for the 3.2-mm depth are summarized in Table 4. As seen in

Figure 31b and Table 4, the M_s = 1.10 case exhibits a near-linear trend for almost the whole duration of the useable experiment (i.e. 2.32 ms), and the M_s = 1.23 scenario loses its linear behaviour after about 1.99 ms; for Mach 1.32 it is 1.75 ms and for Mach 1.40 it is around 1.24 ms; but for Mach 1.60, it is about 0.47 ms. One can therefore conclude that comparatively weaker shocks (M ~ 1.1) show the initial, linear behaviour for the longest period of time. Also, with an increase in Mach number, the dust-rise trend loses its linear behaviour sooner *(i.e.,* t_{tr} decreases with increasing M_s).

The experimental findings plotted in Figure 30 and the results of the analyses in Figure 31 provide valuable information to develop a correlation between the shock strength and the dust entrainment height. From the above-mentioned graphical representation, it can be concluded that an M_s-dependent correlation with an excellent goodness of fit (r^2) could be determined, as seen in Eqn. 19.

$$\alpha = dY/dt = 17.74M_s - 17.08 \quad (19)$$

The above correlation has an r^2 of 0.96 and uses Y as the dust height and M_s as the shock Mach number, with units of α of mm/ms; it should be noted that the correlation is limited to the conditions of the current study, although it does shed light on the general trend between growth rate and M_s.

For the 12.7-mm dust layer depth, data were collected for a set of five different shock Mach numbers similar to those studied for the 3.2-mm dust layer. The time evolution of the dust-layer depths is plotted in Figure 32, which also compares the influence of M_s. Similar trends as for the study of the 3.2-mm dust-layer depth is observed, i.e., the rate of dust rise increases with increasing Mach number, particularly

for the initial, linear regime. In this set of tests with the larger dust thickness, interestingly the M_s = 1.32 and 1.40 cases did not show similar results as in study of the 3.2-mm limestone layer. Correlations for the growth rate in the linear regime were obtained for each M_s using the form of Eqn. 18. For times greater than t_{tr}, Figure 32 shows a reduced average growth rate but a much larger level of height variation with time than seen in the first regime. These effects are discussed in more detail in the Discussion section. Figure 33a provides a relative comparison of dust growth in the first regime, where the dust height linearly increases for different shock Mach numbers for the 12.7-mm dust layer depth. Such a plot (which excludes the delay time, τ) displays the strong effect of M_s on the growth rate for times less than t_{tr}.

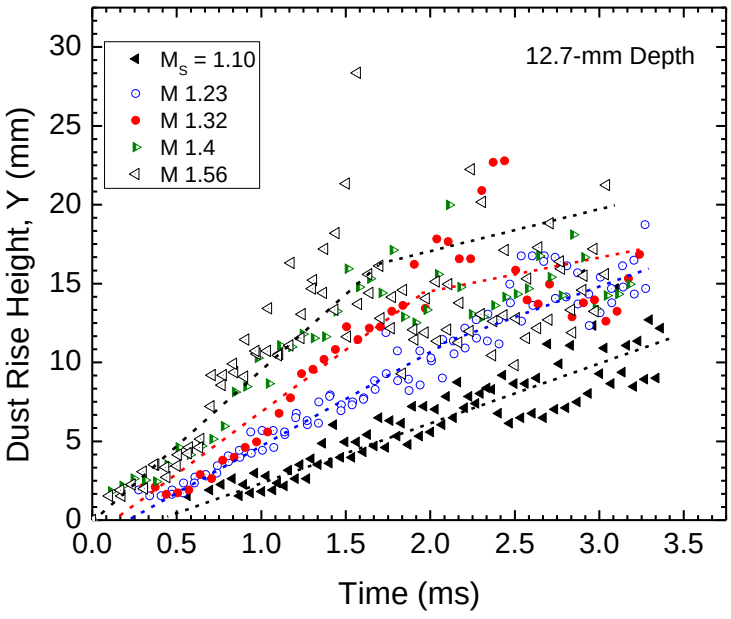

Figure 32: Time-dependent dust rise height for various Mach numbers for a dust-layer depth of 12.7 mm. Dashed lines emphasize average trends.

From the experimental findings plotted in Figure 32 and the result of the analysis in Fig. 33a, a correlation has been developed between the shock strength and the dust entrainment height for the 12.7-mm dust-layer depth, as seen in Eqn. 20.

$$\alpha = dY/dt = 19.83M_s - 18.23 \quad (20)$$

The above correlation has an r^2 of 0.96 and should only be used for summarizing the trends seen at the conditions and powder type of the present study. Similar to the discussion above for the smaller depth, Figure 33b identifies the transition zones for each M_s (i.e., the deviation from linear behavior) for the 12.7-mm dust-layer experiments. Table 4 summarizes the results for each t_{tr}.

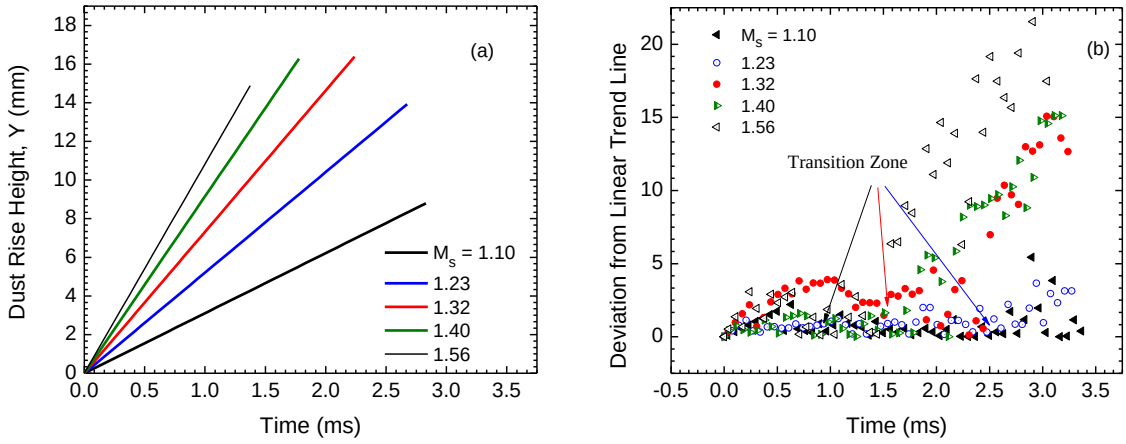

Figure 33: Detailed analysis of the 12.7-mm dust-layer depth results. (a) Initial (linear) rate of dust layer rise as a function of Mach number from Eqn. 18; values for α are in Table 4. (b) Deviation of dust rise height from the linear trend prediction versus time for various Mach numbers.

Note that for the two smallest M_s, there was no discernible t_{tr} within the 3-ms or so test time herein. Also, comparing the results between the two different depths (Table 4), it is observed that the larger-depth dust layer leads to larger t_{tr} values and, hence, longer times within the initial, linear growth regime.

At this point within the presentation of the results, it is useful to begin to compare the relative growth rates between the two different dust-layer depths. Figure 34 contrasts the linear dust height increase rates for $t < t_{tr}$ for the 3.2-mm and 12.7-mm dust-layer depths. In each case, the linear correlation for different Mach numbers was obtained with an average r^2 value of 0.96 (Eqns. 19 and 20).

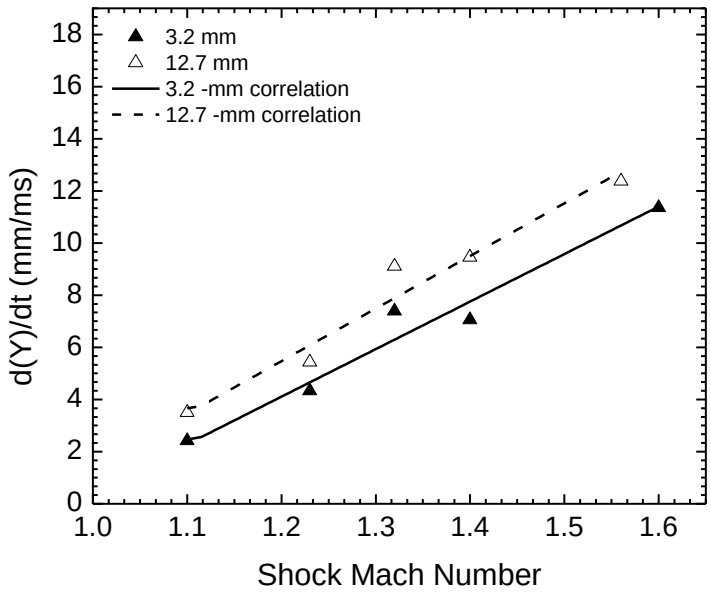

Figure 34: Correlations of the dust rise rates in the linear regime (α = dY/dt) with shock Mach number for the 3.2- and 12.7-mm dust-layer depths. The data are the symbols, and the correlations from Eqns. 19 and 20 are represented as the lines.

From Figure 34, it can be observed that with increasing dust-layer depth, a measurable increase in the rate of the dust layer rise rate is seen. For the range of M_s in Figure 34, the rate for the 12.7-mm depth is about 20% higher than the corresponding rate for the 3.2-mm dust-layer depth.

To understand this finding better, in Figure 35 the effect of dust-layer depth is studied separately for four different M_s (1.10, 1.23, 1.32, and 1.40) by utilizing the Y-versus-time data.

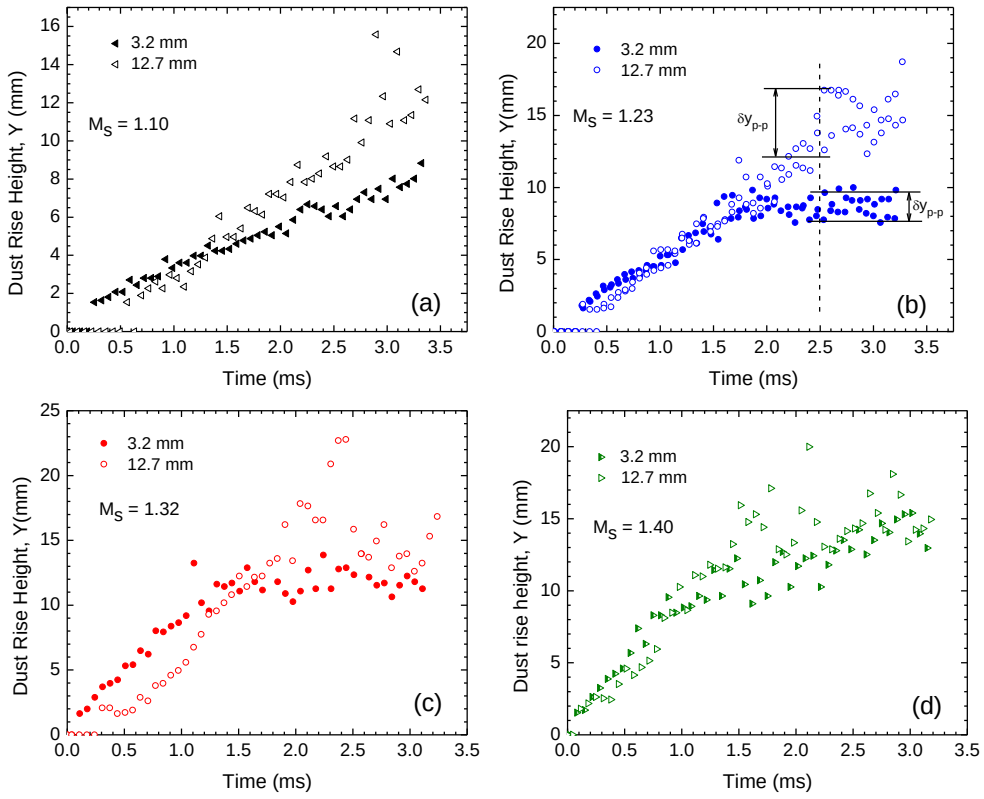

Figure 35: Effect of dust layer thickness on dust entrainment for four different shock wave Mach numbers (a) 1.10; (b) 1.23; (c) 1.32; and (d) 1.40. The definition of the peak-to-peak fluctuation $\delta y_{p\text{-}p}$ at t = 2.5 ms is shown in (b).

In each case, the slopes are similar, but there is a slight difference in slopes between the two dust-layer depths over the initial period of dust-height rise. This minimal (yet measurable with the data herein) effect of dust-layer depth at earlier times shows fair agreement to the limited findings available in the literature [5]. However, there are stark differences between the two layer thicknesses for later times, particularly the delayed transition to the second growth regime for the 12.7-mm cases and the much larger variation in Y with time for $t > t_{tr}$. At longer times, in general, the dust heights are greater for the 12.7-mm-depth experiments for all shock strengths.

5.6. Effect of moisture content on the entrainment process

For all the previous experiments, we used untreated limestone, as that is the form used in coal industry where our data will be useful. In order to investigate the effect of moisture content, limestone dust samples were dried until no further weight loss in the sample was evident. The 3.2-mm dried limestone dust was subjected to normal shock waves of M_s: 1.24. Figure 36(a) is the graphical representation of the time evolution of the dust layer at M_s = 1.24 where the data points represent the measured dust layer height over the time period shown for 3 different tests. Figure 36(b) compares the linear growth rate of a dried and undried limestone dust sample. For identical experimental variables such as shock strength and dust layer depth, the dried limestone dust demonstrates higher dust rise rate in the linear regime. The increasing dust rise rate could be explained through the effect of agglomeration on the dust lifting process. Agglomerated particles have higher terminal velocity compared to monodispersed

particles [62, 63]. Therefore we looked into the scanned electron micrograph of both dried and undried limestone samples.

From Figure 27, already we identified the shape of limestone is complex and it is difficult to identify the size of individual particle. The dust particle size distribution is very wide as well. However, closely observing the dried limestone SEM images (Figure 37b) and comparing with undried limestone (Figure 37a) it seems the particles lose agglomeration but also it looks as if particles were breaking down into smaller pieces. This behavior is very interesting, and more attention should be given towards this issue. Drying most likely breaks the limestone dust agglomerates, thus the dust rise rate increases significantly in the fast-growing linear regime as shown in Figure 36(b).

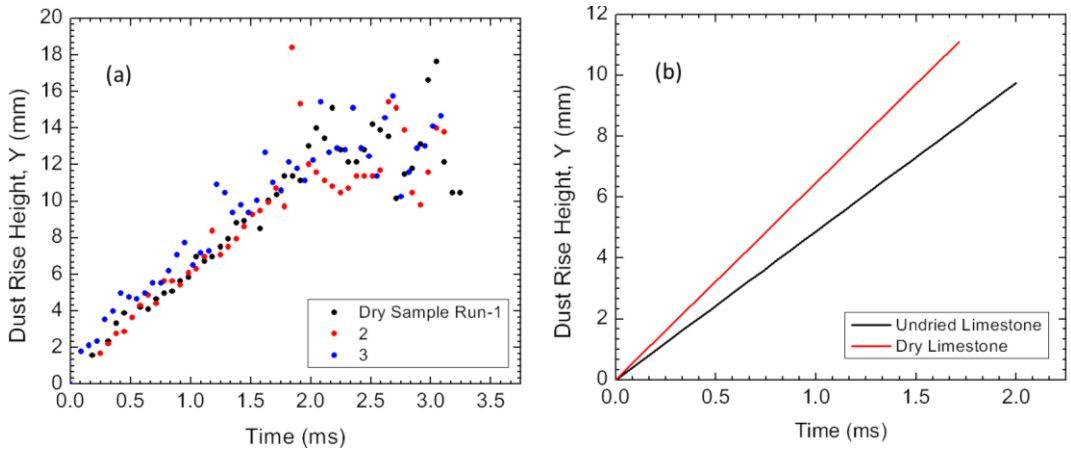

Figure 36: (a)Time-dependent dust rise height for Ms=1.24 for 3.2 mm dried limestone dust layer (b) Initial (linear) rate of dust layer rise as a function of Mach number for dried and undried limestone dust sample.

However, due to the shape of limetsone it is difficult to identify the single particle size and agglomerated particle size for both dry and undried samples, as shown in Figure 37.

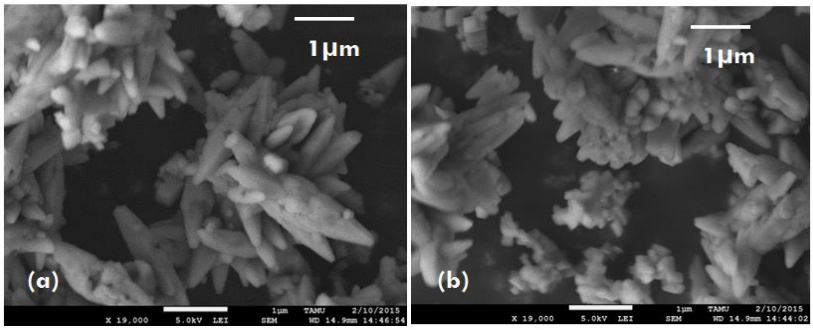

Figure 37: SEM images (a) undried (b) dried limestone sample.

5.7. Delay time measurement

The delay time τ is defined herein as the delay in lifting the dust from the layer behind the moving shock wave. It was measured by determining the time difference between appearances of the shock wave at the reference x-axis in the image and lifting the dust above the reference y-axis (*i.e.*, the visible bottom surface of image). However, in the present facility, there is a small difference in height between the lower window/aperture and the shock-tube lower wall. The result is that the initial top of the dust layer (*i.e.*, the shock-tube wall) is 1.45 mm below the field of view (see Figure 24). Therefore, the first 1.45 mm of dust rise was not observable for the tests presented in this work. The end result is that any experimentally determined delay time is higher than the actual delay time.

Figure 38a presents a plot of the raw τ as a function of M_s for the two different dust-layer depths studied. This plot in Fig. 38a shows a trend towards decreasing τ for increasing Mach number. At first inspection, this trend is certainly in agreement with previous work on dust-lifting delay times [28-30].

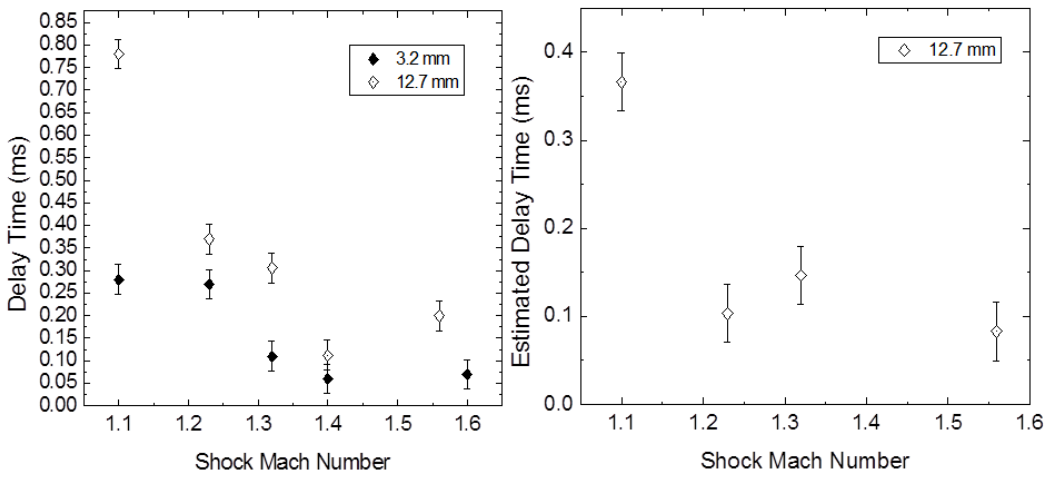

Figure 38: Measured delay time for the dust layer to reach the 1.45-mm optical aperture window for both dust-layer depths, 3.2 and 12.7 mm. (a) Raw values for delay time τ from the experiments as a function of M_s. (b) Re-plot of the t data, but adjusted for the estimated time it takes for the dust to pass the first 1.45 mm, using the rates from Eqns. 20 to estimate the dust layer vertical velocity for 12.7-mm dust layer depth.

However, on closer inspection, one has to take into account the time it takes the dust layer to rise above the 1.45-mm blind zone mentioned in the previous paragraph. This effect can be corrected for by assuming the rate of dust rise over this zone is the

same as the rates determined from the data presented above. In this way, the Y-versus-time correlations with M_s were employed to adjust the observed delay times for the blind region. Figure 38b shows the resulting comparison. The overall result from Figure 38b is that when the dead zone is taken into account, there is essentially no delay time in the dust rise, at least not within the accuracy of the of the present setup.

For example, the framing rate of the camera itself creates an uncertainty of at least ±0.03 ms or more. For all but the smaller M_s, the corrected delay times are on the order of 0.1 ms or less, with very little if any dependence on M_s within the accuracy of this determination. Hence, if there is any dust rise delay time dependence on M_s, it cannot be resolved with the present apparatus. Future studies on this phenomenon using the author's facility would need to be done after modification of the hardware to eliminate the 1.45-mm blind zone and to incorporate a faster framing-rate camera. Some variation in dust-rise delay time could also be due to variation in the dust compaction from test to test. Better resolution on the delay time phenomenon in future experiments might also shed some light on the theory provided by Gerrard [20] and Borisov et al. [21] as both studies discussed the possibility of shock and compression waves being reflected in the dust layer. More focus should be given to better understand this phenomenon in the future.

5.8. Discussion

As seen in Figures 30 and 32 for each M_s, there is an initial region of near-linear growth, followed by a low-growth regime and/or turbulence zone with relatively higher data scatter. In Figure 30 and 32, the average trends in the different growth regimes are

shown using dotted lines for easy visualization. Comparing the obtained data with the image sequence in Figure 28, it is seen that the quantitative data points for Y as a function of time are in agreement with the shadowgraph images of the dust layer surface. For example, the dust lifting begins after the passage of the shock wave, and in Figure 28c the growth is near-linear. Later on, the linear trend is replaced by a more-scattered growth, and eventually in Figure 28f the reflected shock wave is witnessed. In Figure 28e, it is observed that the interface between the dust cloud and the air field resembles waves, analogous to Kelvin-Helmholtz instabilities [21].

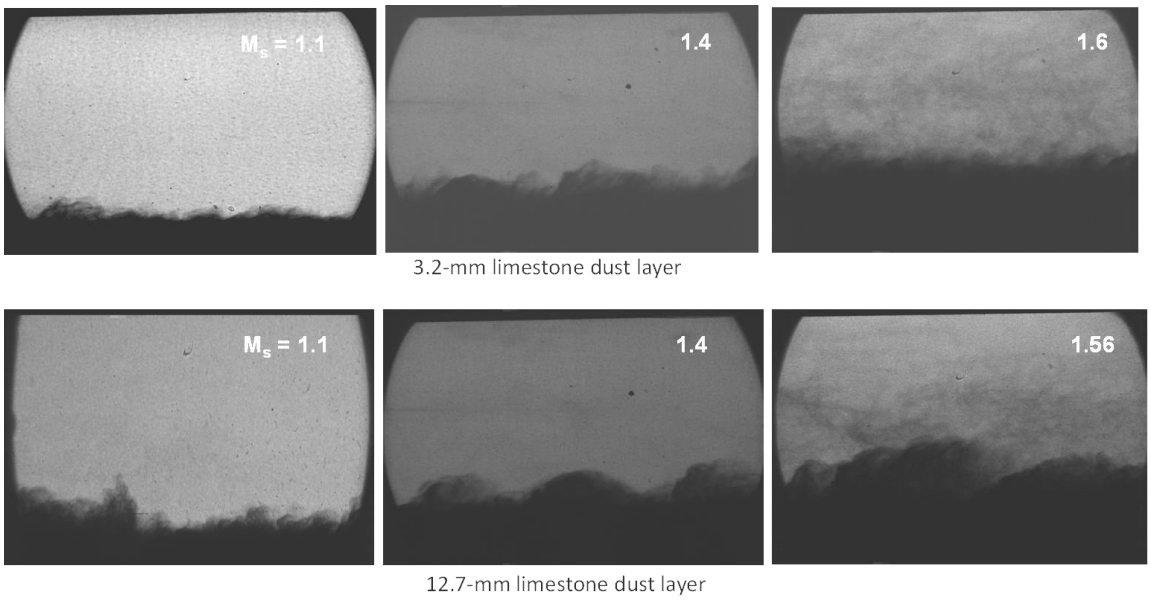

Figure 39: Shadowgraph image sequences for the 3.2-mm depth (upper) and 12.7-mm depth (lower) for three different shock wave Mach numbers. All images were taken from a post-shock time near 2.5 ms.

This behavior is in agreement with the experimental findings of Borisov et al. [21] for the passage of a detonation wave over a bed of coarse sand particles. In light of these observations, further investigation of the development of turbulence at later times after the passage of the shock wave over the dust layer would be of practical and fundamental interest. To this end, a brief discussion of this behavior, contrasting the differences between the two dust-layer heights, is presented as follows. Focusing on the turbulent regions, the relative effect of M_s and layer depth can be demonstrated through the image sequences shown in Figure 39. All of the images in Figure 39 were taken at a common time of 2.5 ms after passage of the incident shock wave. In the upper sequence, three different shock Mach numbers of 1.10, 1.40, and 1.60 are presented for the 3.2-mm depth. These snapshots show several interesting phenomena. The most-evident phenomenon is the much overall greater height of the dust layers as M_s increases. Also significant is the noticeably larger level of surface instabilities for the higher Mach numbers. In addition, the magnitude of the fluctuations for the 12.7-mm depth (lower set of images, Figure 39) appear larger than for the 3.2-mm case, particularly for the highest M_s. Finally, the $M_s = 1.60$ (and similarly for the $M_s = 1.56$ case, lower sequence) result shows a greater amount of mixing, to the extent that just defining a clear boundary between the dust layer and the surrounding gas may not be completely descriptive of the dust particle locations. Future experiments should explore the concentration gradient of the powder material in more detail, particularly for the higher shock velocities.

A quantitative analysis of the surface fluctuations at a later time after shock passage, namely at 2.5 ms, was performed using the measured Y data from plots such as

those in Figure 35. A peak-to-peak fluctuation in height, called $\delta y_{p\text{-}p}$, was therefore defined as shown in Figure 35b. This parameter is taken as the extent of peak-to-peak scatter in the Y-versus-time data for a given shock strength and dust-layer thickness. Table 5 presents a comparison of the fluctuating surface data for a common time of 2.5 ms aftershock passage. These data can be plotted as either the absolute magnitude of the variation in mm or as a relative percentage of the average value of Y at the time of interest. Figure 34a shows the results for $\delta y_{p\text{-}p}$ as a function of M_s. It is quite noticeable in Figure 34a that the deeper dust layer ultimately leads to much larger dust-layer height fluctuations at these later times than does the smaller depth. It was determined that the trend follows the form of

$$\delta y_{p\text{-}p} = \beta M_s^{\,n} \tag{21}$$

where $\delta y_{p\text{-}p}$ is in mm and β and n are constants. These curves are plotted along with the data in Figure 40a. When plotted with $\delta y_{p\text{-}p}/Y$ as a percentage, the trends are similar, as shown in Figure 40b. However, for the lower M_s, the surface fluctuations are relatively constant at about 25% for the 3.2-mm depth and about 40% for the 12.7-mm depth. Around $M_s = 1.5$, the fluctuations as a percentage of Y increase exponentially, as seen in Figure 40b. The corresponding empirical curve fits to the trends in Figure 40b follow the forms provided in the plot legend, with a Mach number variation in % fluctuations of about M_s^{10}. Of course, caution should be taken when applying these general trends outside of the conditions covered herein, but they nonetheless provide some useful insight as to the correlation between the magnitude of dust-layer surface instabilities and the shock Mach number and initial dust-layer thickness. That is, the

larger depth seems to lead to significantly more surface turbulence and, hence, mixing than the smaller dust depth.

Table 5: Measured dust height fluctuations at a common time of 2.5 ms after shock passage. The definition of δy_{p-p} is given in Fig. 35b.

	3.2-mm Depth		12.7-mm Depth	
M_s	δy_{p-p} (mm)	$\delta y_{p-p}/Y$ %	δy_{p-p} (mm)	$\delta y_{p-p}/Y$ %
1.10	1.7	24	3.2	39
1.23	2.0	23	5.0	37
1.32	3.3	27	9.0	47
1.40	3.6	29	8.0	44
1.56	-	-	20	95
1.60	7.5	39	-	-

According to the National Fire Protection Association (NFPA 654), handling combustible dust with initial depths of 12.7 mm is much above the allowed dust-layer depth at any zone. The reason behind choosing 12.7 mm and 3.2 mm herein was to help understand, primarily, the physical processes of dust lifting behind a propagating shock wave. During design modification and test section (window and dust pan) installation, special attention was given to the x-t diagram study of this facility to maximize the

experiment observation time. Also, for current facility, the maximum observation time is about 3.5 ms. Installing a dump tank at the endwall will allow for an increase in the observation time. This increase would help to understand the behavior of the dust rising beyond 3 ms (which currently is denoted as the scatter zone). Since in many cases the blast wave created by a dust explosion is subsonic, further investigation is also needed for compression waves below $M_s = 1$.

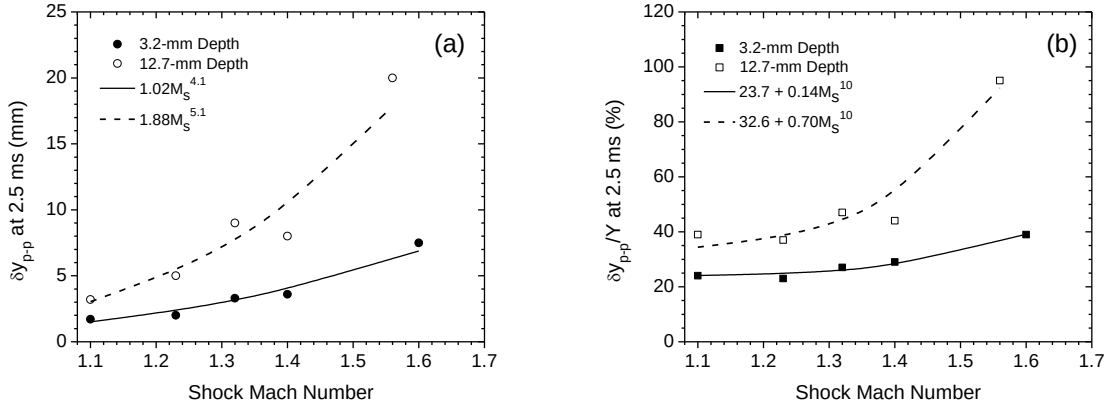

Figure 40: Analysis of the dust-layer height fluctuations, $\delta y_{p\text{-}p}$, at a post-shock time of 2.5 ms for the 3.2- and 12.7-mm dust-layer depths. (a) Magnitude of the fluctuations in mm and the corresponding correlations with M_s. (b) Fluctuations as a percentage of the average Y value along with the corresponding M_s trend curves.

5.9. Conclusions

The main purpose of this study was to develop a better understanding of the role of shock Mach number on dust entrainment behind a shock front. From the results obtained, at least two regimes of growth were identified: a faster, near-linear growth at early times, transitioning to a slower growth rate but with much larger surface fluctuations at longer times. A linear relationship was found between the dust entrainment height growth rate and the shock strength (Mach number) for different limestone dust layer depths, with larger M_s leading to higher growth rates. The effect of dust-layer depth for the two cases studied (3.2 and 12.7 mm) was minimal during the first growth regime, but the result for the 12.7-mm depth showed a delayed transition to the reduced-growth regime and much larger (by a factor of 2 or more) surface fluctuations at longer times than the 3.2-mm depth. These fluctuation results when quantified using a peak-to-peak δy parameter accentuated the differences between the two dust-layer depths and showed trends that could be well correlated with M_s. Overall, the images and corresponding changes in dust height Y showed some interesting trends and behavior that will be beneficial for developing simulation tool of secondary dust explosion in industry.

CHAPTER VI

EFFECT OF PARTICLE SIZE POLYDISPERSITY ON DUST ENTRAINMENT PROCESS

6.1. Synopsis

This study explores the effect of aluminum dust size polydispersity on the dust entrainment behind a moving shock front. Aluminum samples of analogous average size (D_{50}) with varying polydispersity (σ_D) were processed by blending commercially accessible samples of different D_{50} and narrow size distributions. This study also elucidates the effect of particle density on the dust lifting process. The study confirms particle size and size polydispersity has significant impact on dust lifting as smaller particles lift higher and faster for a given shock. The effect of size polydispersity to the best of our knowledge has not been studied experimentally prior to this work. Similar to the study with limestone, new data were collected for image analyses over longer periods than found in prior works, where the longer observation time and higher camera framing rates led to the discovery of trends not previously observed by earlier studies, namely a clear transition time between the early, linear growth regime and a much-slower average growth regime. Though current study shows similar regimes as in the case of limestone, because of a difference in density there are distinctive differences in the entrainment trend, which is discussed here by comparing dust lift height for a specific M_s for limestone and aluminum with similar size.

6.2. Introduction

All of the experiments used aluminum dust samples. The explosive properties of aluminum powder are available in the literature. According to National Fire Protection Association (NFPA) fire prevention standards [78] aluminum is graded as one of the most explosive metal dusts. The chemical safety board stated approximately one fourth of all dust explosions in the United States between 1980-2005 involved metal dusts [2,79]. Aluminum accounted for majority of these metal dust explosions [79]. Metal dusts are responsible for nearly 19% of dust explosions every year globally [80]. Aluminum powder has high explosivity measured using deflagration constant, K_{ST}[2] and ranked as a Class ST-3[3] dust [81-83]. As these data identified aluminum dust as imposing a dust explosion hazard in the current industry, we selected aluminum for our study [84, 85].

6.2.1. Operating conditions

The experimental variables of interest for the present study included particle size, particle size polydispersity, and strength of the shock wave, M_s. Similar to all limestone experiments; the initial driven section pressure was maintained at 67 kPa. Nitrogen was used as both the driver and driven gas. The reason for using nitrogen as the driven gas was to ensure an inert atmosphere inside the shock-tube while running experiments with combustible dust particles. For this study, the shock Mach numbers ranged from 1.23 to

---

[2] $K_{ST} = (dP/dt)_{max} \times V^{1/3}$; $(dP/dt)_{max}$ is the maximum pressure rise rate from the explosion and V is the volume of the confinement.

[3] ST-1, ST-2, and ST-3 are hazard classification of dusts ranked by NFPA used to determine the relative explosiveness. ST-3 dusts are the most explosive.

1.53. Dust layer thickness was kept constant at 3.2 mm. Table 6 summarizes the different experimental conditions for all the experimental studies. However, for this specific study special care was given to monitor P_5, T_5. As the pressure and temperature behind the reflected shock Zone-5 is very high, it should always be monitored closely while handling combustible material inside shock-tube. We used Aluminum particles of 2, 5,15, and 30 microns.

Table 6: Operating conditions for experiments with aluminum dust

Driver/ Driven Gas	Diaphragm Thickness (in)	Variables	T1 (K)	P1 (torr)	M_S
N_2/N_2	0.005 (LEX)	Dust Layer Depth 0.125 in Particle size $D_{3,2}$=1.7,4.3,15.4,30.3 µ Polydispersity σ_D=0.93,1.52,2.62	295	500	1.23
N_2/N_2	0.01 (LEX)		295	500	1.27
N_2/N_2	0.02 (LEX)		295	500	1.42
N_2/N_2	0.03 (LEX)		295	500	1.53

6.2.2 Dust sample characterization

Figure 41 displays example SEM images of the aluminum dust particles used in the experiments described herein. Figure 41(a) (b) (c) SEM shows the comparison of sizes for 1.7, 15.4, and 30.3 micron aluminum particles taken at the same resolution. From the images, we can confirm the samples are considered monodispersed, meaning they have very narrow particle size distribution. Table 7 summarizes deflagration constant (K_{ST}) and particle size used in this experiment. From the mean diameter (D_{50})

and Sauter diameter ($D_{3,2}$) we calculated the polydispersity (σ_D) and sphericity (Ψ) of each sample. Though for our specific experiment we do not need K_{ST} values- it is a good practice to be aware of all the necessary explosion hazard parameters while developing operating procedure for handling combustible dusts.

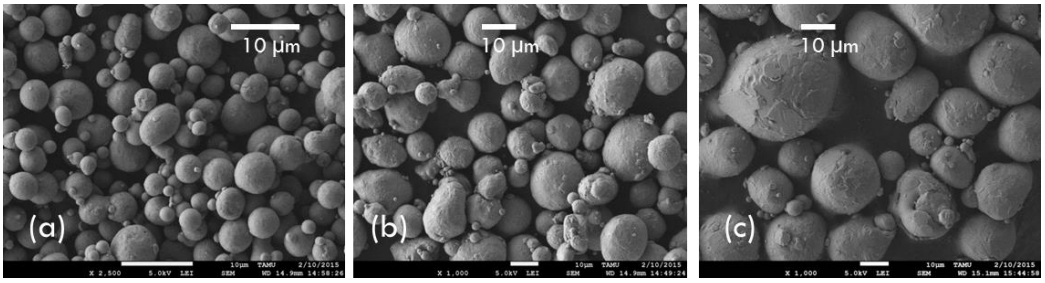

Figure 41: SEM image of Aluminum samples with different particle sizes; (a) 2 µm (b) 15 µm (c) 30 µm taken at same resolution

Table 7: Aluminum sample commercial size, D_{50}, $D_{3,2}$ and K_{st} values

Commercial Particle size	2-3 µm	5-7 µm	15-17 µm	30-35 µm
K_{st} [3] (bar-m/s)	451	430	179	110
D_{50}[4] [86]	2.57	4.76	16.21	32.88
$D_{3,2}$[5] [86]	1.66	4.38	15.42	30.28

[4] D_{50} is the mean particle size.
[5] $D_{3,2}$ is the sauter mean diameter [3]

6.3. Effect of shock strength and particle density on dust lifting process

The 3.2-mm aluminum dust was subjected to normal shock waves of the following M_s: 1.23, 1.27, 1.42, and 1.52. Figure 42 shows a typical image sequence of the experiment with 15.4 micron aluminum dust, starting from the left side; for this particular experiment, the shock Mach number was 1.52. Applying the in-house developed MATLAB code, shadowgraphs were analyzed to generate data. Dust growth rate in this case even at later times are not as distinctive as it was for limestone dust. Still the similar trend is observed. Data collection starts when the shock wave passes over the reference plane. From the image (Figure 42), subsequent movement of aluminum particle behind shock front can be identified. However, no significant evidence of eddy formation at later times was witnessed.

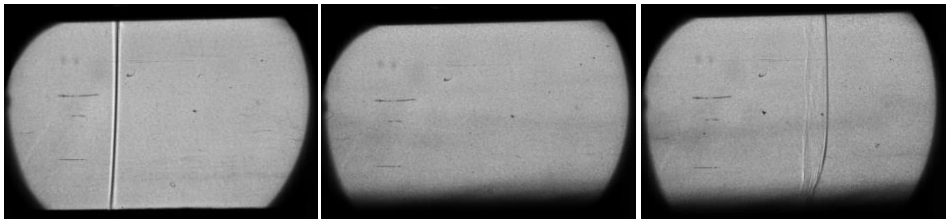

Figure 42: Typical images of air and aluminum dust interaction in the flow behind a moving shock wave in the author's shock-tube facility; M_s = 1.52

The time evolution of the dust-layer depths is plotted in Figure 43, which also compares the influence of M_s. Similar trends as for the study of the 3.2-mm limestone dust-layer depth is observed, i.e., the rate of dust rise increases with increasing Mach number, and the growth rate occurred in two stages: a linear regime of higher growth,

followed by a regime of lower average growth. An interesting observation in the first linear regime shows a comparatively flat regime (slower growth) which suddenly transitions to the linear, fast-growing regime. As mentioned earlier, with current setup first 1.45 mm dust rise data cannot be monitored. For the limestone studies, there was no indication of having different trend for the first 1.45 mm. Yet for aluminum dust it is quite possible to have presence of three growing regimes. So far from the images, we can identify the two regimes reported earlier with an indication of a different slower regime before the fast-growing linear regime. In Figure 43, the dashed line represents the two regimes that were earlier detected in this study. As for current setup it is not possible to investigate the possible third regime at the beginning of dust entrainment, in this study the flat regime will be ignored for rest of the data analysis. However, this area definitely needs further attention in future studies. So next a linear correlation was derived for the slope of this initial dust layer rise (ignoring the flat regime at the beginning) and is plotted for the various Mach numbers in Figure 44a. Figure 44b identifies the transition zone from the initial linear regime to the more-fluctuating regime.

From the findings of Figures 43 and 44, the following correlation between the shock strength and the dust entrainment height was developed using the form of Eqn. 18.

$$\alpha = dY/dt = 5.56\ M_s - 5.11 \qquad (22)$$

The above correlation has an r^2 of 0.89 and uses Y as the dust height and M_s as the shock Mach number, with units of α of mm/ms.

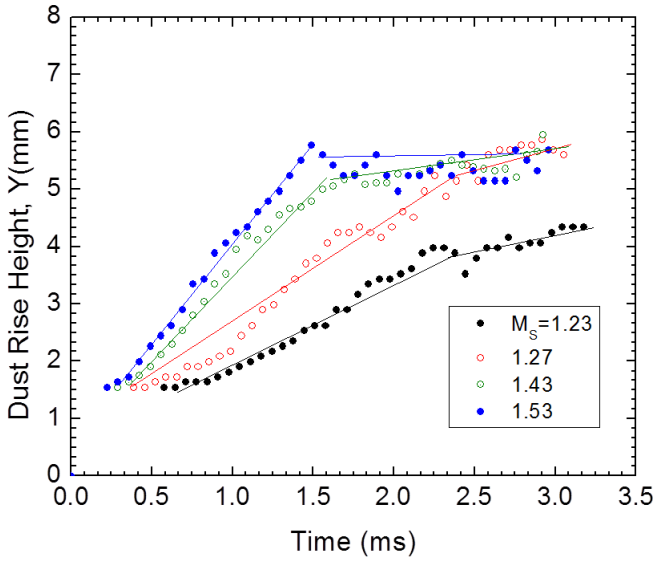

Figure 43: Time dependent dust rise height for various Mach numbers for 15.4 µm aluminum dust-layer depth of 3.2 mm.

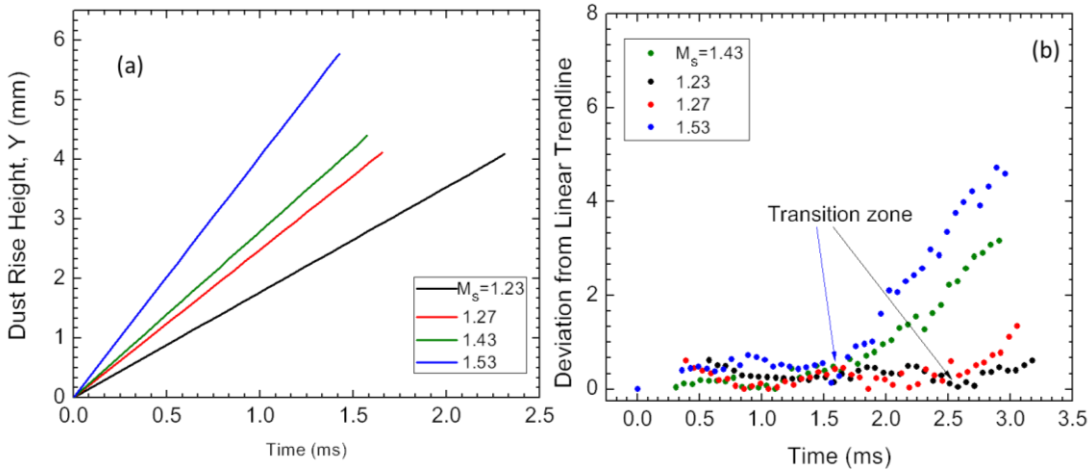

Figure 44: Detailed analysis of the 3.2-mm dust-layer depth results. (a) Initial (linear) rate of dust layer rise as a function of Mach number (b) Deviation of dust rise height from the linear trend prediction versus time for various Mach numbers.

One of the significant observations from experiments with Aluminum was even for very high Mach numbers, dust rise height was comparatively lower than what was observed in the case of limestone in the previous chapter. To have a clearer idea, experiments for limestone and aluminum dust were carried out for similar operating condition, dust layer thickness, and sizes. Figure 45 demonstrates the graphical representation of dust rise height with respect to time for M_s = 1.42 for limestone and aluminum dust both having an average particle size of 4.3 microns and a 3.2-mm dust layer thickness. For limestone and aluminum, dust we observed similar trends: a linear regime of higher growth followed by a regime of lower average growth but increased dust surface variation. For the first regime (i.e. between delay time and transition time) the trend is quite similar. However there are stark differences in the second regime, though both demonstrated transition to lower average growth rate; in the case of aluminum the surface fluctuation is distinctively lesser compared to the limestone surface variation, i.e. the magnitude of the fluctuations for limestone appear larger than for the aluminum particles.

In summary from Figure 45, the most-evident phenomenon is the much overall greater height of the dust layers for limestone dusts and noticeably larger level of surface instabilities. A quantitative analysis of the surface fluctuations at a later time after shock passage, namely at 2.8 ms, was performed using the measured Y data from plots such as those in Figure 46. A peak-to-peak fluctuation in height, called $\delta y_{p\text{-}p}$, was therefore defined as shown in Figure 45.

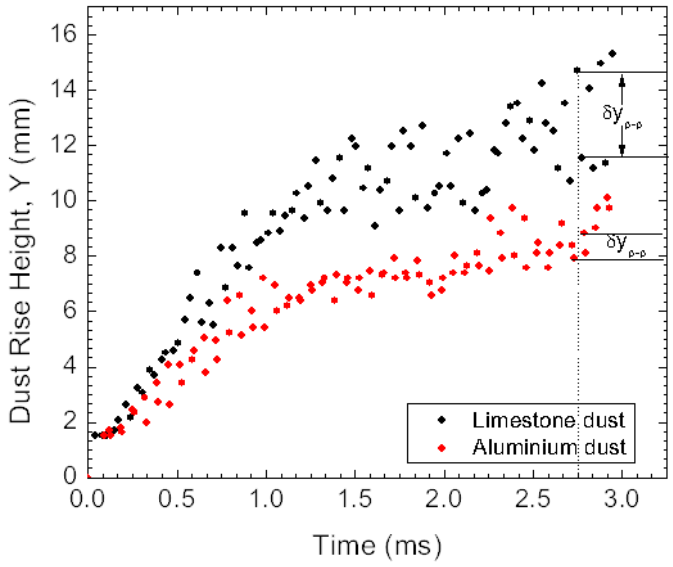

Figure 45: Effect of dust layer thickness on dust entrainment for limestone and aluminum dust. The definition of the peak-to-peak fluctuation δy_{p-p} at t = 2.8 ms is shown.

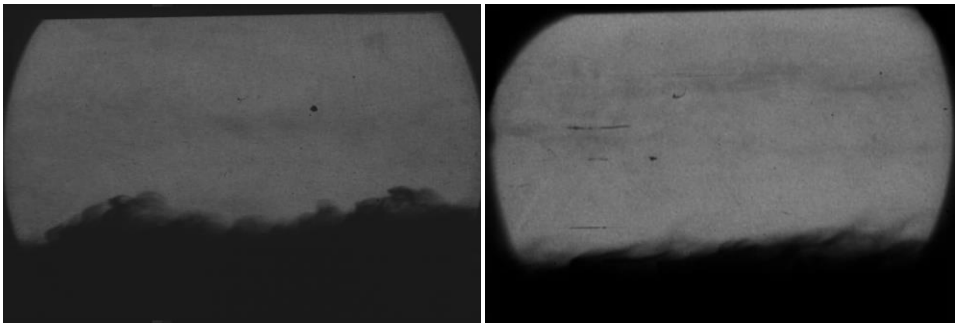

Figure 46: Shadowgraph image for the 3.2-mm depth (a) limestone dust (b) aluminum dust. All images were taken from a post-shock time near 2.8 ms.

This parameter is taken as the extent of peak-to-peak scatter in the Y-versus-time data for a given shock strength and dust-layer thickness. For limestone at 2.8 ms δy_{p-p}=

3.15 mm, whereas for aluminum δy_{p-p}= 0.09 mm. This result elucidates the effect of density and other physical properties of dust particles on the entrainment process. Bulk densities of limestone and aluminum dust are respectively around 1.1 g/cm^3 and 1.5 g/cm^3. However, the results are very interesting as at earlier times they demonstrate similar behavior with close delay time and transition time. Density did not show any significant impact there. But later on during the surface fluctuations by turbulent mixing, the physical properties could be one of the driving factors in creating eddies. Also the sphericity of the particles or morphology might have impact on the turbulent mixing process. Comparing SEM images of limestone and aluminum dust particles (Figure 27 and 41), there is startling difference in morphology, with the aluminum particles being highly spherical.

6.4. Effect of particle size on dust lifting process

Tateuki and Takashi investigated the effect of particle size on the lifting phenomenon using organic dust powder of 15, 84, and 300 μm for Mach numbers ranging from 1.4 to 1.7 and concluded that smaller particles tend to lift faster than larger particles [16]. However, in their study, the particles of different sizes were different materials with almost identical particle density but different morphology. Though [16] they demonstrate excellent work, we believe using the same particle of different sizes would eliminate the effect of other variables such as morphology or physical properties. Hence the effect of particle size on dust lifting behind a moving shock front was studied using aluminum particles having different mean diameters with very narrow particle size distributions; as demonstrated in Figure 41. In this investigation, 3.2-mm dust layer

depth was chosen, where 1.7, 4.3, 15.4, and 30.3 micron aluminum dust particles were subjected to normal shock waves of M_s = 1.42. The time evolution of the dust-layer depths is plotted in Figure 47, which also compares the influence of particle sizes. Within the current experimental data, it was observed that the rate of dust rise increases with decreasing particle size. The growth rate occurred in two stages: a linear regime of higher growth, followed by a regime of lower average growth with dust surface variation.

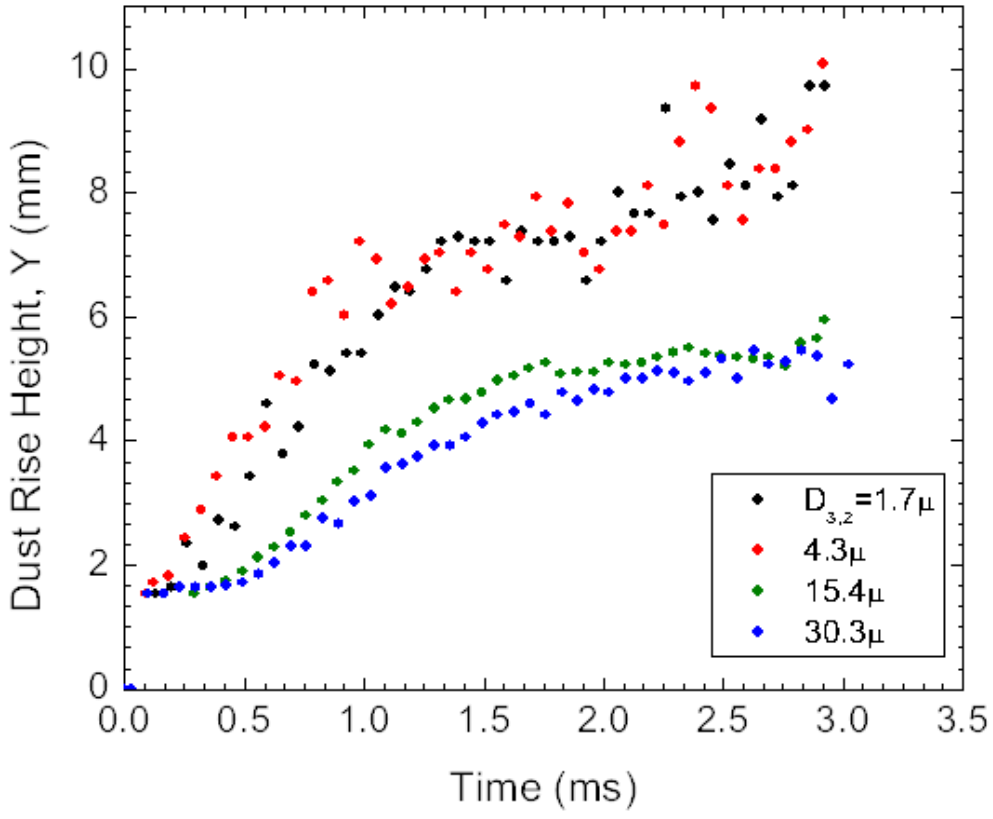

Figure 47: Time dependent dust rise height for various particle sizes of aluminum dust for M_s=1.42 at dust-layer depth of 3.2 mm.

These results for the first regime are in agreement with trends found in the literature [16], namely with respect to the effect of smaller particle size on increasing growth rate. As mentioned earlier, though the growth rate changes, even in the second regime not much surface variation is observed. From Figure 48a and b, we observe for smaller particles the initial fast growth rate is for shorter period of time, *i.e*. the transition occurs sooner. However for the smaller particles the growth rate is higher in both regions than the larger particles, and surface fluctuation is also comparatively higher. Interestingly 2- and 5-micron particles demonstrate almost identical results, whereas 15- and 30-micron particles represent similar trends as well. This indicates the possibility of a threshold size when the growth rate switches from a larger particle trend to a smaller one (for gradually lowering particle sizes).

A linear correlation was derived for the slope of this initial dust layer rise and is plotted for the various particle sizes in Figure 48a; this figure provides valuable information for the early growth regime where the dust height linearly increases with time for different sizes. For times after the dust-layer rise delay time, τ, and the regime transition time, t_{tr}, the dust height Y follows a linear trend.

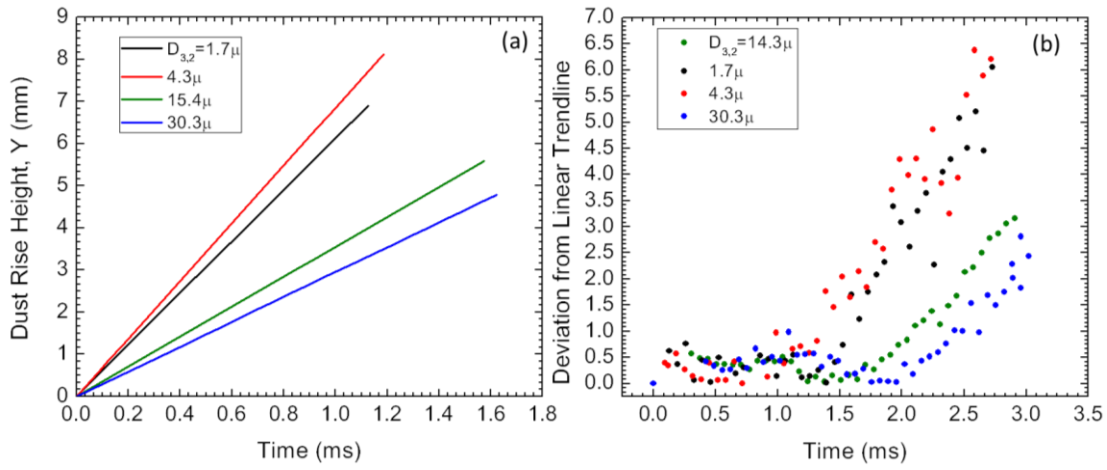

Figure 48: Analysis of 1.7, 4.3, 15.4, 30.3 μm aluminum dust. (a) Initial (linear) rate of dust layer rise as a function of particle size (b) Deviation of dust rise height from the linear trend prediction versus time for various sizes.

The experimental findings plotted in Figure 47 and the results of the analyses in Figure 48 provide valuable information to develop a correlation between the particle sizes and the dust entrainment height following the form of Eqn. 18. From the above-mentioned graphical representation, it can be concluded that a $D_{3,2}$-dependent correlation with a goodness of fit (r^2) could be determined, as seen in Eqn. 23.

$$\alpha = dY/dt = -0.095D_{3,2} + 5.02 \quad (23)$$

The above correlation has an r^2 of 0.83 and uses Y as the dust height and $D_{3,2}$ as the particle size, with units of α of mm/ms. The correlation is graphically represented in Figure 49. It should be noted that the correlation is limited to the conditions of the current study, although it does shed light on the general trend between growth rate and $D_{3,2}$. The reason for using $D_{3,2}$ instead of D_{50} in the correlation is to adapt with the dust

explosion research world. It has been discussed in the literature that explosion hazards characterization of combustible dust provides better representation in terms of $D_{3,2}$ and σ_D [3].

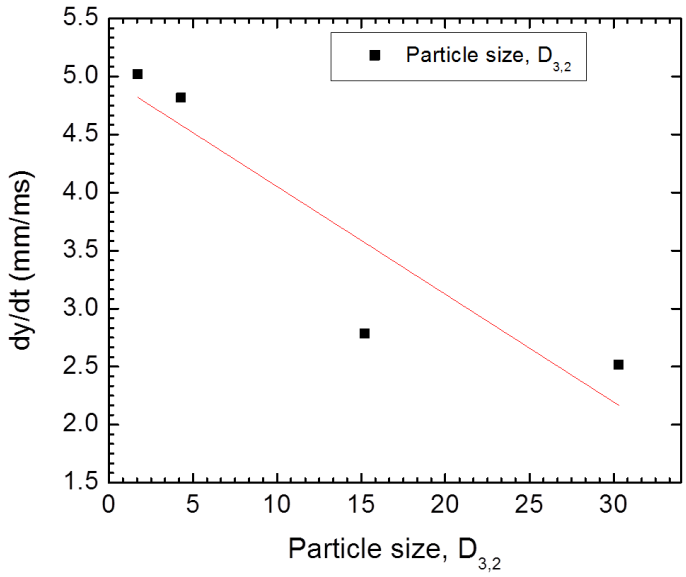

Figure 49: Correlations of the dust rise rates in the linear regime (α = dY/dt) with particle size (Sauter mean diameter, $D_{3,2}$) for the 3.2- mm dust-layer depths

6.5. Effect of particle size polydispersity on dust lifting process

Dust explosion severity is characterized using the deflagration constant, K_{St} and minimum ignition energy (MIE) [89] which is affected by dust particle sizes [3,90]. Some very recent studies identified that these parameters do not only depend on average particle diameter but also on particle size polydispersity σ_D [3].

σ_D is used to determine the width of the particle size distribution (PSD). High σ_D means a broad particle size distribution. Often it is not reported along with the mean

diameter [91,92]. Most industrial dusts demonstrate a wide particle size distribution. Still, most of the experimental and theoretical dust explosion-related research select samples with narrow particle size distributions or at least chooses to consider the average particle diameter, not the size polydispersity. Specially for modeling dust entrainment processes behind a moving shock front, it is a challenge to compare experimental data from diverse researchers when the results are reported in terms of different definitions of average particle size. Also to the best of our knowledge, prior to this study no experiments were performed to address the effect of particle size polydispersity on the dust lifting phenomenon. Therefore the objective of this investigation was to understand the effect of size polydispersity on the dust entrainment process.

6.5.1. Polydisperse sample preparation and size characterization

Aluminum samples with the subsequent mean diameters: 2, 5, 9, 15, 20, 25, and 30 μm were methodically blended to prepare polydisperse samples. The particle size distribution of the original samples was supplied by the vendors, and our SEM images are in good agreement with their analysis. The Vendor's PSD analysis provided us different valuable information such as: size distribution on a volume basis, Sauter mean diameter ($D_{3,2}$), and the statistical diameters D_{10}, D_{50} and D_{90}. For instance, D_{90} indicates the particle size for which 90% of the particles by weight are finer [3]. Table 8 summarizes the statistical diameters and polydispersity of the original sample.

Table 8: Commercially obtained sample size analysis

Commercially supplied size range (μm)	D_{10} (μm)	D_{50} (μm)	D_{90} (μm)	σ_D	$D_{3,2}$ (μm)
2-3	0.125	2.57	4.86	1.84	1.7
5-7	2.81	4.76	7.92	1.07	4.3
9-11	6.55	10.18	15.79	0.91	9.6
15-17	10.5	14.82	24.28	0.93	15.42
19-21	12.83	20.15	31.33	0.92	18.96
24-26	15.88	25.02	39.78	0.96	23.61
30-35	19.04	32.88	57.86	1.18	30.3

Our objective was to have samples with different polydispersity but same mean diameter. Therefore, 3 samples were used in this experiment with varying σ_D but similar D_{50} (~15 μm). The samples were prepared by mixing each commercially supplied sample (based on calculation) in a jar filled to about one-thirds capacity and manually shaking each sample for about 20 to 30 minutes to ensure proper mixing. The samples' SEM images proved the perfect blend. Table 9 demonstrates the mass fraction of each size added to prepare the polydisperse samples. Further details on polydisperse sample preparation can be found from dissertation of Dr. Castellanos [3].

Table 9: Polydispersed sample preparation with similar D_{50} (~15µm)

	Wt. fraction of each sample added							D_{50}	σ_D
Commercial size range	2-3 (µm)	5-7 (µm)	9-11 (µm)	15-17 (µm)	19-21 (µm)	24-26 (µm)	30-35 (µm)		
Sample-1	-	-	-	1	-	-	-	15.4	0.93
Sample-2	-	0.125	0.125	0.5	0.125	0.125	-	14.5	1.52
Sample-3	0.333	-	-	0.333	-	-	0.333	14.8	2.62

Figure 50 represents the SEM (scanning electron microscopy) images of the prepared samples with different size polydispersity. Figure 50(a) shows sample-1 with σ_D = 0.93, where a-1 and a-2 provides captured micrographs at different resolution. Figure 50(b) represents micrographs of sample-2 with σ_D = 1.52, and finally Figure 50(c) is the SEM images for sample-3 with the high polydispersity, i.e., σ_D = 2.62. As in each case the mean size, D_{50} is similar these samples represent perfect examples of polydisperse samples that if described only in terms of D_{50} will not be distinguishable, which is often a problem in industry and research world. σ_D = 0.93 represents very low polydispersity. Figure 50(a) confirms, sample-1 looks fairly monodispersed. With the gradual increase of polydispersity, sample-3 demonstrates high polydispersity in Figure 50(c). The PSD analysis of the samples also provide analogous conclusion.

6.5.2. Experiments with aluminum samples of different size polydispersity

In this investigation, a 3.2-mm dust-layer depth was chosen, where aluminum dust particles with approximately 15.4-µm particles with varying size polydispersity

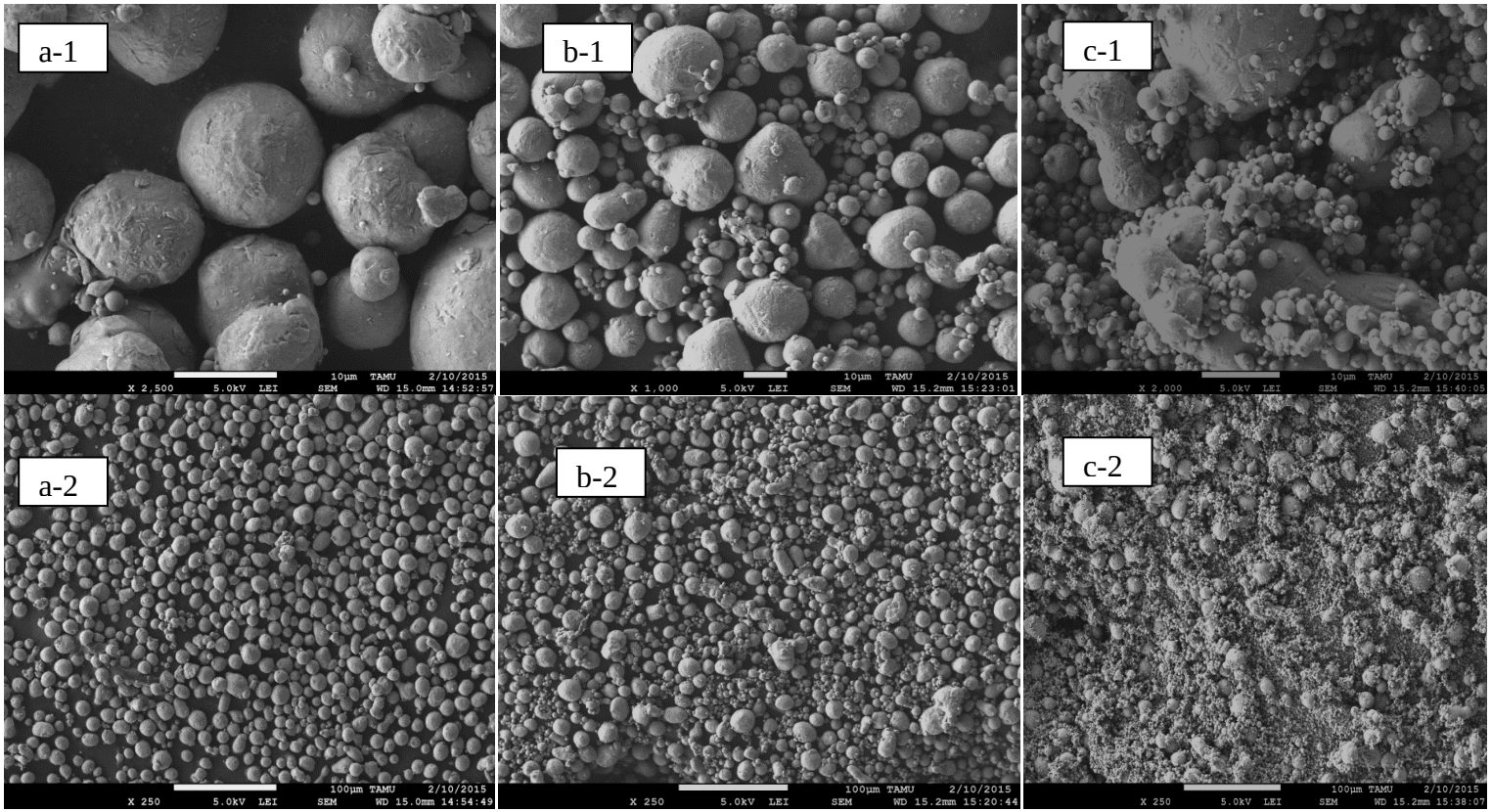

Figure 50: SEM images of prepared polydisperse (a) sample-1, (b) sample-2 and (c) sample-3

Ranging from 0.93 to 2.6 were subjected to normal shock waves of M_s = 1.42. The time evolution of the dust-layer depths is plotted in Figure 51, which also compares the influence of particle size polydispersity. Within the current experimental data, it was observed that the rate of dust rise increases with increasing particle size polydispersity. Similar to all other studies in this work, the growth rate occurred in two stages: a linear regime of higher growth, followed by a regime of lower average growth with dust surface variation. As mentioned earlier, there has been no experimental study to investigate the effect of size polydispersity. However a very recent numerical study looked into this subject [94]. The results for the first regime are in agreement with trends found in this work [94], namely with respect to the effect of high polydispersity on increasing growth rate.

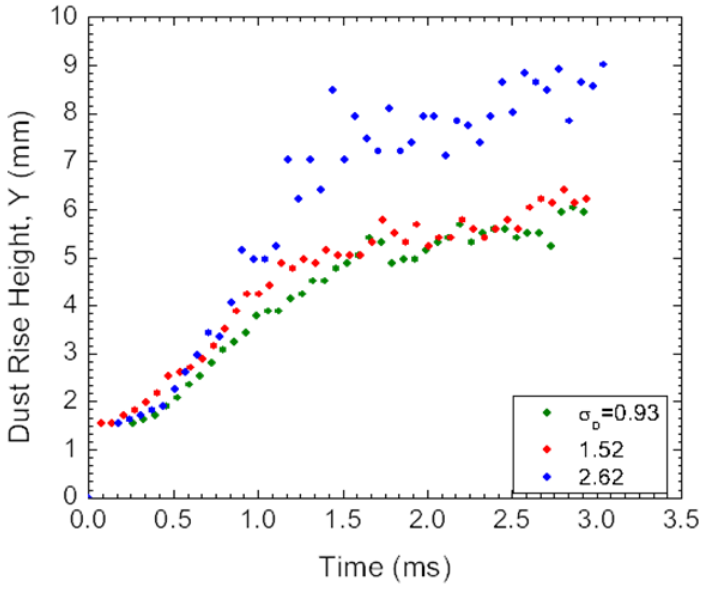

Figure 51: Time-dependent dust rise height for aluminum dust with mean size, D_{50} ~ 15 µm but different size polydispersity for M_s = 1.42 at dust-layer depth of 3.2 mm.

By comparing the overall dust rise height under the influence of particle size and polydispersity from Figures 47 and 51, many interesting facts are demonstrated. In Figure 51, though for all the three aluminum samples the mean size is identical, aluminum dust with higher polydispersity (σ_D = 2.6) reaches a higher dust height close to the one demonstrated by smallest particles (2 μm) in Figure 47. Also for particles with high polydispersity, surface variation is observed in the second regime. In fact the peak-to-peak variation observed for dust with high polydispersity is higher than the smallest particles (~2μm) observed in Figure 47. Sample-1 (σ_D = 0.93) and sample- 2 (σ_D = 1.52) interestingly demonstrate almost identical results. This indicates the possibility of a threshold value of polydispersity when it starts to affect the entrainment process for the identical mean size particles.

A linear correlation was derived for the slope of this initial dust layer rise and is plotted for different size polydispersities in Figure 52a. Figure 52b identifies the time at which the dust layer stopped rising linearly for each test, hence is used to identify the transition zone from linear behaviour for different particle size polydispersity. From Figure 52b it is evident that though the linear dust rise rate is different, the transition zone for all the three samples are very close. The experimental findings plotted in Figure 51 and the results of the analyses in Figure 52 provide valuable information to develop a correlation between the particle size polydispersity and the dust entrainment height following the form of Eqn. 18, which is the the linear trend of dust height Y for times after the dust-layer rise delay time, τ, and the regime transition time, t_{tr}.

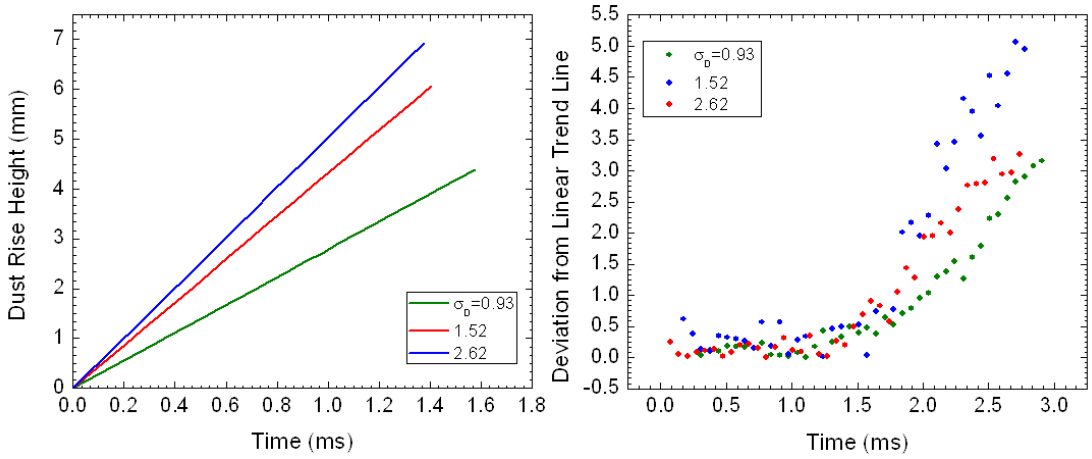

Figure 52: Analysis of (~15 µm) aluminum dust with different size polydispersity. (a) Initial (linear) rate of dust layer rise as a function of polydispersity (b) Deviation of dust rise height from the linear trend prediction versus time for various size polydispersity.

From the above-mentioned graphical representation, it can be concluded that a σ_D-dependent correlation with a goodness of fit (r^2) could be determined, as seen in Eqn. 24.

$$\alpha = dY/dt = 1.4794\sigma D + 1.02 \quad (24)$$

The above correlation has an r^2 of 0.974 and uses Y as the dust height and σ_D as the particle size polydispersity, with units of α of mm/ms; it should be noted that the correlation is limited to the conditions of the current study, although it does shed light on the general trend between growth rate and σ_D.

6.6. Delay time measurement

Similar to the study with limestone, the delay time τ is the delay in lifting the dust from the layer behind the moving shock wave. It was measured by determining the time difference between appearances of the shock wave at the reference x-axis in the image and lifting the dust above the visible bottom surface of image. As mentioned earlier, the first 1.45 mm of dust rise was not observable. Therefore, the experimentally determined delay time is higher than the actual delay time.

Figure 53a presents a plot of the raw τ as a function of M_s for aluminum dust with mean size, D_{50} of 15.4 μm. This plot in Figure 53a shows a trend towards decreasing τ for increasing Mach number, which is certainly in agreement with previous work on dust-lifting delay times [28-30]. Also, similar trends were observed for limestone dust subjected to shock waves of various strength. This plots in Figures 52b and 52c show trends towards increasing τ for increasing particle size and decreasing τ for increasing σ_D.

The effect of the 1.45-mm blind zone is corrected by assuming the rate of dust rise over this zone is the same as the rates determined from the data presented above. In this way, the Y-versus-time correlations with M_s were employed to adjust the observed delay times for the blind region shown in Figure 53d. Unfortunately, with the current uncertainty of framing rate (±0.03 ms), when the dead zone is taken into account, we could obtain only one estimated delay time for M_s = 1.42. However for M_s = 1.23, 1.27, and 1.52 there is essentially no delay time in the dust rise, at least not within the accuracy of the of the present setup. Similar results were found the Y-versus-time

correlations with $D_{3,2}$ and σ_D were employed to adjust the observed delay times for the blind region.

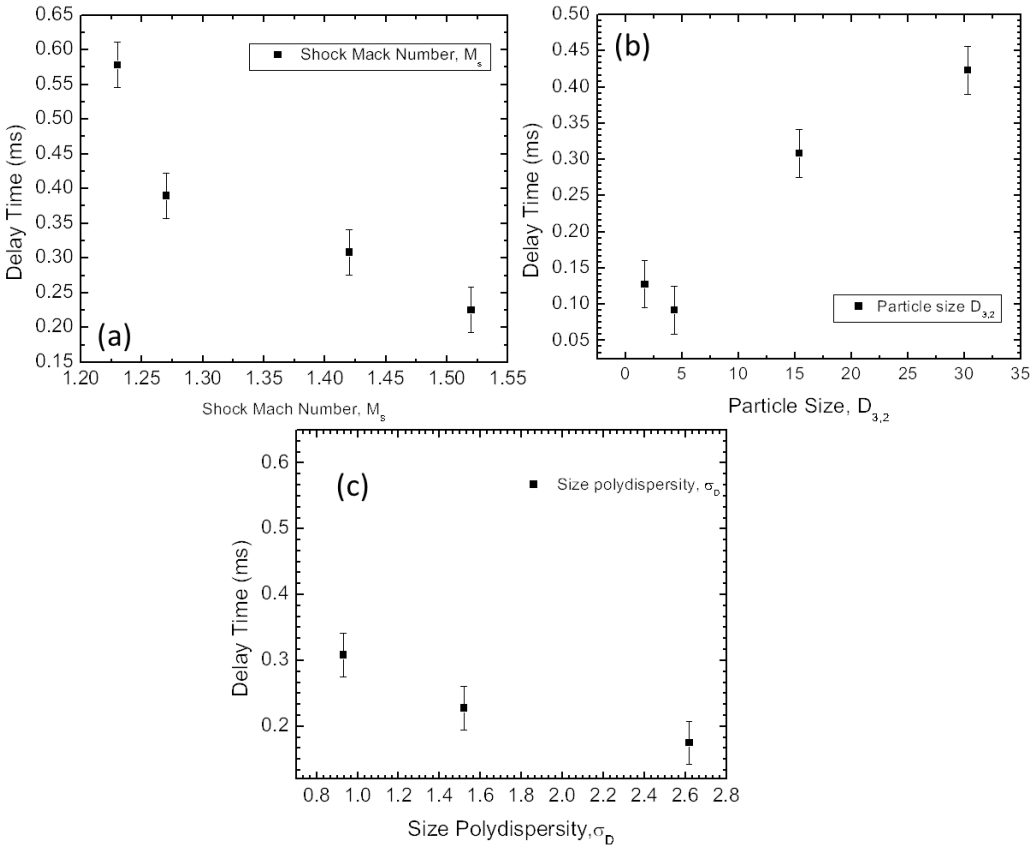

Figure 53: Measured delay time for the dust layer to reach the 1.45-mm optical aperture window for dust-layer depths, 3.2 mm. (a) Raw values for delay time τ from the experiments as a function of M_s. (b) Raw values for delay time τ from the experiments as a function of particle size, $D_{3,2}$. (c) Raw values for delay time τ from the experiments as a function of size polydispersity σ_D.

6.7. Discussion

As seen in Figures 43, 47, and 51 for M_s, $D_{3,2}$ and α_D respectively, there is an initial region of near-linear growth, followed by a low-growth regime. Table 10 summarizes the resulting α values, transition time, t_{tr} and raw delay time, τ for each M_s, $D_{3,2}$ and α_D.

Table 10: Experimental results for various dust-height parameters for different M_s, $D_{3,2}$ and α_D. The delay time τ is the raw delay time including the 1.45-mm blind zone.

(a) Effect of shock strength				
M_S	t_{tr} (ms)	α=dY/dt (mm/ms)	τ (ms)	Correlation $Y = \alpha t$ ($\tau < t < t_{tr}$)
1.23	2.378	1.54	0.578	$\alpha = 5.56\ M_s - 5.11$
1.27	1.723	2.249	0.389	
1.42	1.651	2.549	0.308	
1.52	1.492	3.443	0.225	
(b) Effect of particle size				
$D_{3,2}$	t_{tr} (ms)	α=dY/dt (mm/ms)	τ (ms)	Correlation $Y = \alpha t$ ($\tau < t < t_{tr}$)
1.7	1.195	5.023	0.128	$\alpha = -0.095D_{3,2} + 5.02$
4.3	1.386	4.816	0.092	
15.4	1.651	2.784	0.308	
30.3	1.623	2.517	0.423	
(c) Effect of size polydispersity				
σ_D	t_{tr} (ms)	α=dY/dt (mm/ms)	τ (ms)	Correlation $Y = \alpha t$ ($\tau < t < t_{tr}$)
0.93	1.651	2.549	0.308	$\alpha = 1.4794\sigma_D + 1.02$
1.52	1.472	3.037	0.228	
2.62	1.442	4.978	0.175	

As seen in Figure 44b and Table 10-a, the effect of shock strength study with aluminum, the M_s = 1.23 case exhibits a near-linear trend for the longest duration of the useable experiment (*i.e.* 2.38 ms), and the M_s = 1.27 scenario loses its linear behaviour after about 1.72 ms; for Mach 1.42 it is 1.65 ms, and for Mach 1.52 it is around 1.49 ms. Therefore we can conclude that similar to the limestone study, with an increase in Mach number, the dust-rise trend loses its linear behaviour sooner *(i.e.,* t_{tr} decreases with increasing M_s). However comparing with the overall trend of limestone dust rise, aluminum demonstrates a longer transition time in general. The correlation developed also is in agreement with the study of limestone dust lifting, where the dust rise rate increases with increasing shock strength, M_s. A quantitative analysis of the surface fluctuations at a later time after shock passage, namely at 2.8 ms, was performed for both limestone and aluminum powder, using the measured Y data from plots such as those in Figure 45. A peak-to-peak fluctuation in height, called $\delta y_{p\text{-}p}$, was therefore defined as shown in Figure 45. This parameter is taken as the extent of peak-to-peak scatter in the Y-versus-time data for a given shock strength and dust-layer thickness. It is quite noticeable that limestone dust ultimately leads to much larger dust-layer height fluctuations at these later times than does the aluminum powder. Differences in density and morphology of these two dust particles are the possible reasons behind this behavior.

As seen in Figure 48b and Table 10-b, regarding the effect of particle size study on aluminum dust lifting process, 15.4 and 30.3 μm particles exhibits a near-linear trend for the longest duration of the useable experiment, 16 ms and 1.62 ms, respectively. The smaller particles had smaller transition time, and the 1.7-μm dust had a transition from

initial linear zone after 1.2 ms. The correlation developed from the experimental finding concludes with the increase of particle size dust rising rate decrease. Next, in the study of particle size polydispersity, the transition time decreased with increasing polydispersity shown in Figure 52b and Table 10-c. The high polydispersity sample with σ_D = 2.6 was a blend of 1.7 µm, 15.4 µm, and 30.3 µm in equivalent quantity. Closely observing the experimental findings, it is found though that sample-3 with high polydispersity had D_{50}~15µm; the α values is very close to the ones determined for 1.7 µm particles. The transition time though remains close to the transition time, t_{tr} of 15.4 µm particles. This indicates the smaller particles in a dust sample of high polydispersity is the governing factor behind higher dust rise rate compared to dusts with same mean size but lower polydispersity.

In the background section, significant aerodynamic lifting forces have been discussed. Drag force, Saffman and Magnus forces are considered the governing forces for dust particle lifting. The effect of particle size can be explained through drag force as drag force depends on the size and sphericity of the particle. Smaller particles have higher drag, therefore reaching terminal velocity faster [60]. In a very recent numerical modelling work to understand the effect of particle size polydispersity on dust lifting behind a shock wave, similar conclusions to our experimental findings were observed [94]. The authors in their simulation work presented trends of particle collision frequency for polydisperse and monodisperse particles. According to their findings, particle collision increases for polydisperse samples [94], which could be another governing force in the dust lifting phenomenon.

6.8. Conclusion

The main purpose of this study was to develop a better understanding of the role of particle size and size polydispersity on dust entrainment behind a shock front. From the results obtained, at least two regimes of growth were identified: a faster, near-linear growth at early times, transitioning to a slower growth rate. A linear relationship was found between the dust entrainment height growth rate and the particle size (Mach number) for aluminum dust. Also, linear correlations were developed between dust rise rate and size polydispersity.

Dust entrainment trends of limestone and aluminum powder were compared at the same shock strength, dust layer depth, and mean size to understand the effect of particle density on the dust lifting phenomenon. Heavier particles *(i.e.* aluminum) show comparatively very low surface fluctuations. This result also indicates the morphology of powders could impact the lifting phenomenon as well.

CHAPTER VII

PHYSICS OF DUST ENTRAINMENT BEHIND SHOCK WAVE

7.1. Synopsis

This chapter identifies and summarizes the significant findings from experiments conducted in this research to elucidate the fundamental understanding of the dust entrainment phenomenon behind a propagating shock wave. Based on the research findings, recommendations are provided for numerical modelers to simulate dust entrainment behind a moving shock front. Finally, some recommendations are also provided for NFPA 654 that could be helpful for preventing secondary dust explosion.

7.2. Introduction

For numerical simulation, the mathematical interpretation of dust entrainment follows different hypotheses of dust entrainment mechanisms. One of the widely used hypotheses considers movement of a single dust particle in the shear flow under the influence of aerodynamic drag, gravity and aerodynamic lift forces such as Saffman [64] and Magnus [54] forces. Most of the computations that consider this approach tend to describe only the initial stage of dust entrainment and imitate the pattern of growth of the upper edge of the dust cloud [102]. Also, some modelers have tried to incorporate the Kelvin–Helmholtz mechanism to explicate perturbation of particles on the dust surface [102]. However, numerical simulations of the development of eddies arising due to the instability of the interface between the dust layer and the gas phase behind a propagating shock wave are still in very early stages and have not yet shown quantitative agreement with experimental findings. In this section, some of the results of the experiments with

limestone and aluminum dusts are highlighted that will improve the understanding of dust-entrainment process.

7.3. Turbulent dusty boundary layer

In this work, Aluminum and Limestone dust were subjected to shock waves of different Mach numbers to study the effect of shock strength on the dust entrainment phenomenon. Also the effect of dust layer thickness, particle size, and size polydispersity on the dust lifting process has been elucidated. For all of our experiments, we witnessed the dust entrainment occurred in two stages: a linear regime of higher growth, followed by a regime of lower average growth but increased dust surface variation. The amplitude of the linear regime as well as the surface variation of the second regime depends on many factors. The slope of the linear regime increases with the shock strength and decreases with the particle size. The second, slower-growing rate regime indicates the presence of acoustic disturbance that arises from the setup. However, limestone dust exhibited higher surface fluctuations than aluminum dust at the second stage for the identical shock strength and particle size. These indicate the presence of other governing factors that control the threshold entrainment rate of dust lifting. The cohesiveness of limestone dust could be a major contributing factor behind this behavior. It also explains why limestone dust rises to a larger height when similar-sized aluminum and limestone dusts are subjected to similar experimental conditions. Smaller, cohesive particles can be lifted as agglomerates. The degree of dust dispersion in the air medium behind the shock front also depends on the breakdown of the aggregates. Singer *et al.* demonstrated from their coal mine experiments cohesive or

wetted dusts have the tendency of lifting as relatively large chunks which then disperse in the air stream [95].

Typical image sequences of the dust-air interaction behind a shock wave for 3.2-mm and 12.7-mm limestone dust and aluminum dust are shown in Figures 20, 28, and 42, respectively. In all three cases, we observed that a normal shock wave is followed by the subsequent movement of the dust layer in the vertical direction. Gradually the edge of the dust layer becomes more turbulent, with observed eddies or ripples forming on the surface. In Figures 20 (d) and 28(e), typical eddy structures are highlighted in yellow just to show this common turbulent trend. As discussed earlier, this resembles the wave structures analogous to Kelvin-Helmholtz instabilities. Kelvin-Helmholtz instabilities typically originate in parallel shear flows. The small-scale disturbances gain kinetic energy from the mean flow [96]. These perturbations indicate the presence of a turbulent, dusty boundary layer. A turbulent dusty boundary layer is an interesting concept as it behaves differently than a clean, turbulent boundary layer. A dusty turbulent boundary layer is dominated by density effects whereas for clean turbulent boundary layers viscous effects and wall drag are the dominating factors [100]. Usually these density effects lead to baroclinically [100] created vortices, as the dust density near the wall is very large but velocity very small. Dusty boundary layers grow due to turbulent entrainment of dust from the wall, and this leads to much faster growth rates than in the clean case. So, in the case of a turbulent dusty boundary layer turbulent mixing occurs which impacts the overall entrainment. The detailed study of surface

fluctuation in this work will be beneficial for developing mathematical models for turbulent mixing.

7.4. Recommendation for numerical modelers

This study identified significant parameters that will be beneficial for developing numerical models of secondary dust explosion scenarios for better hazard assessment. Correlations are developed that depict the relation between linear dust growth rate with shock strength, particle size and size polydispersity behind a propagating shock front. Close observation of the second fluctuating regime provided correlations between the magnitude of dust-layer surface instabilities and the shock Mach number and initial dust-layer thickness. However, caution should be taken when applying these general trends outside the conditions covered herein, but they nonetheless provide some useful insight into understanding the dust lifting phenomenon.

From the experimental findings, below are some recommendations other than the developed correlations and identified parameters are provided for the numerical modelers of dust entrainment behind shock front.

- In the literature review, the significant aerodynamic forces in numerical modeling of the dust-lifting phenomenon has been summarized. Often as lifting force either Saffman [64] or Magnus [57] forces are considered. Figure 54 demonstrates result of a numerical simulation compared with experimental results of this study. Using an Eulerian framework for computation, the results of Houim and Oran [34] trended well with data obtained from our experimental findings at M_s = 1.4. In the computational study, Magnus force was assumed as

the governing lift force. In current work, it has been demonstrated that particle size and polydispersity affect the dust lifting phenomenon. Increased particle-particle collisions in high-polydispersity dust could be the reason behind higher dust rise rates. Therefore, particle-particle collision should be considered as one of the governing forces.

- 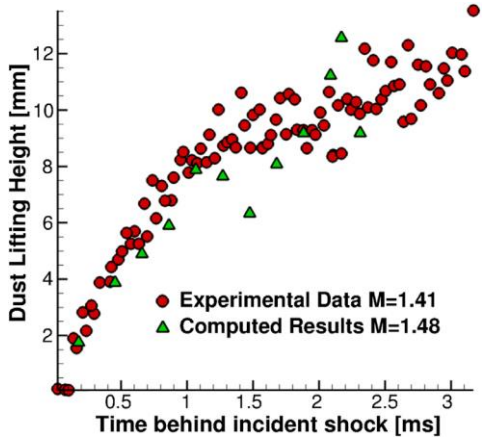

Figure 54: Comparison between experimental and simulation results [34]

- In the introduction of this chapter, different hypotheses that are usually used by numerical modelers are summarized. Movement of single particles introduced in the shear flow of a viscous gas medium under the action of different governing forces is a commonly used hypothesis. Other models have attempted to consider turbulent diffusion of particles in the gas flow field behind the propagating shock front. This research work not only proposes correlations but also identifies at least two growing regimes: a faster growing, linear regime followed by a slower-

growing, more fluctuating regime. The correlations are limited to the conditions of the current study, although they do shed light on the general trend. Therefore even for choosing hypotheses for modeling purposes, the modelers should consider two separate entrainment regimes. Also, a new parameter has been introduced as transition time which identifies the transition time between two regimes.

- Sauter mean diameter, $D_{3,2}$ is the mostly used dimension to define particle size in current research. Our experiments were able to demonstrate particle size polydispersity has impact on the dust-lifting phenomenon. Often, dust entrainment behind propagating shock wave experiments are coupled with deflagration studies [97]. Dr. Castellanos [3] in her thesis work demonstrated significant impact of particle size polydispersity on dust explosion severity. Therefore during modeling, the dust particles should be characterized in terms of $D_{3,2}$ and size polydispersity, $\sigma_{D.}$

7.5. Recommendation for NFPA-654

Combustible dust is defined by NFPA 654, the *Standard for the Prevention of Fire and Dust Explosions from the Manufacturing, Processing, and Handling of Combustible Particulate Solids*, as: *"A finely divided combustible particulate solid that presents a flash fire hazard or explosion hazard when suspended in air or the process-specific oxidizing medium over a range of concentrations."* Also there are some exceptions that can present a deflagration hazard even though the particle size is larger

than 500 microns, such as fibers, flakes, and agglomerates [13]. The determination of whether a particulate solid poses a flash fire or explosion hazard should be determined using a standardized test method such as ASTM E 1226, *Standard Test Method for Explosibility of Dust Clouds*, ASTM E 1515, *Standard Test Method for Minimum Explosible Concentration of Combustible Dusts*.

In NFPA 654, combustible dusts conventionally were defined as material 420 μm or smaller. In 2013, a revision of NFPA 654 for ensuring consistency with other standards, the appropriate size criterion was changed to 500 μm (capable of passing through a U.S. No. 35 standard sieve). However, no particular characterization definition has been provided so far. From the findings of this work, it is recommended that the dust particles should be characterized in terms of Sauter mean diameter, $D_{3,2}$ and size polydispersity, $\sigma_{D.}$

NFPA 654 includes certain criteria that are used by federal governmental agencies for dust explosion hazard assessment [13] and also to evaluate compliance with the *General Duty Clause of the OSH Act of 1970* [101]. According to a research report by NFPA-*"there is, however, genuine concern over the technical pedigree of those criteria"* [13]. Four methods are described in the NFPA 654 standard: (1) Layer Depth Criterion Method, (2) Mass Method A, (3) Mass Method B, and (4) Risk Evaluation Method. The first three methods are quantitative assessments of the amount of fugitive dust to determine if a hazard exists [13]. For example, in the layer depth criterion method, a correlation is provided between dust-layer depth and bulk density of the dust particles. Prior to revision in 2013, the threshold allowable dust accumulation depth was

1/32 inches. The new correlation compares the dust density with a reference dust density of 75 lb/ft^3 to determine the potential hazard of accumulated dust as shown in the following equation:

$$\text{Layer depth (in)} = (1/32'')*(75\ \text{lb/ft}^3)/\text{bulk density}$$

Based on the relation between bulk density and layer depth, the safe dust accumulation limit is identified. Similar to this, none of the other criteria consider the particle size polydispersity effect, which is significant in the case of dust explosion hazard assessment.

CHAPTER VIII

CONCLUSION AND FUTURE WORK

8.1. Conclusions

This dissertation reports the effect of particle size polydispersity and shock strength on the dust entrainment mechanism behind shock waves. Two components were the major focus of this investigation: combustible dust aluminum and inert dust limestone. The main objective of this research was to gain an understanding of the formation mechanism and parameters affecting the dust entrainment behind a propagating shock front in order to develop more efficient methods to prevent secondary explosion accidents. Based on the current study, the main results and conclusions can be summarized as follows:

1. To study the dust explosion phenomenon, design modification details on an existing shock-tube facility to introduce a new test section for optical flow visualization was introduced. Details of the design modification strategy and shock wave characterization efforts were reported. Finally, the operating procedure was developed for running experiments and handling dusts in shock-tube.
2. Details of the image and data analysis techniques were described in the current study. A shadowgraph imaging technique was applied by installing flat and parabolic mirrors in a particular alignment with the test section with a high-speed camera. A MATLAB code was developed to analyze the captured

shadowgraph images. The repeatability and uncertainties of data analysis technique has also been reported.

3. The role of shock Mach number on dust entrainment behind a shock front was investigated. Numerous images were available from each experiment for test times up to about 3.5 ms, to which a computer-based algorithm was applied that used an RGB technique to distinguish the edge of the dust layer at time steps of 67 μs with high clarity. From the results obtained, at least two regimes of growth were identified: a faster, near-linear growth at early times, transitioning to a slower growth rate but with much larger surface fluctuations at longer times. A linear relationship was found between the dust entrainment-height growth rate and the shock strength (Mach number) for different dust-layer depths, with larger Ms leading to higher growth rates.
4. The effect of dust-layer depth for the two cases studied (3.2 and 12.7 mm) was minimal during the first growth regime, but the result for the 12.7-mm depth showed a delayed transition to the reduced-growth regime and much larger (by a factor of 2 or more) surface fluctuations at longer times than the 3.2-mm depth. These fluctuation results when quantified using a peak-to-peak δy parameter accentuated the differences between the two dust-layer depths and showed trends that could be well correlated with M_s. Overall, the images and corresponding changes in dust height showed some interesting trends and behavior that will be beneficial for developing simulation tools of secondary dust explosion in industry.

5. The effect of size polydispersity (σD) on the dust entrainment process using aluminum dust was also investigated under the current study. Similar to limestone from the results obtained, at least two regimes of growth were identified: a faster, near-linear growth at early times, transitioning to a slower growth. A linear relationship was developed between the dust entrainment linear growth rate and the particle size for aluminum dusts. It was observed that with the increase of particle size, dust entrainment rate decreased. Also, a linear correlation was developed between linear dust rise rate and size polydispersity. Dust entrainment trends of limestone and aluminum powders were compared at similar experimental conditions to understand the effect of particle density on the dust-lifting phenomenon. Limestone dust demonstrated higher growth rates and surface fluctuations. Cohesiveness of limestone dust was identified as one of the possible, significant factors behind higher turbulent mixing.
6. From the significant findings of experiments, recommendations have been provided for developing simulation tools of the dust entrainment process in industrial-scale dust explosion scenarios. For example-mostly used governing lift forces during numerical modeling are either Saffman [64] or Magnus [57] forces. Recently Houim and Oran [34] compared the results of their numerical simulation with experimental results of this study. They assumed Magnus to be the lift force. One of the major findings of this study are significant effects of particle size and polydispersity on the dust-lifting

phenomenon. Therefore, particle-particle collision is recommended to be considered as one of the governing forces.

7. Another recommendation for the numerical modelers identifies the most appropriate dust lifting hypothesis. A comprehensive literature survey was performed to understand all the available hypotheses. This research work not only proposes correlations but also identifies at least two growing regimes: a faster-growing, linear regime followed by a slower-growing, more fluctuating regime. Therefore, even for choosing hypotheses for numerical modeling, two separate entrainment regimes need to be considered. A new parameter has also been introduced as transition time which identifies the transition time between two regimes.
8. Based on the experiments, it was demonstrated that particle size polydispersity has an impact on the dust-lifting phenomenon. One of the major recommendations of this work is to characterize dust particles in terms of Sauter mean diameter, $D_{3,2}$ and size polydispersity, σ_D both in academia and industry.
9. Finally, recommendations are also provided for the National Fire Prevention Association to incorporate particle size polydispersity and Sauter mean diameter in their definition of combustible dust. Another recommendation for NFPA is to consider the effect of particle size polydispersity in their dust accumulation hazard assessment criteria.

8.2. Recommendation for future work

In the present facility, there is a small difference in height between the lower window/aperture and the shock-tube lower wall. This resulted in positioning the initial top of the dust layer (*i.e.*, the shock-tube wall) 1.45 mm below the field of view (Figure 24). Therefore, the first 1.45 mm of dust rise could not be observed for the tests presented in the current work. The results obtained with current facility provided useful insight toward understanding the dust cloud formation mechanism behind moving blast waves. Nonetheless, the facility needs to be modified to fix the current optical aperture which will help to identify actual delay times of the dust-lifting phenomenon. Also, at the current stage two growing regimes have been proposed, though for aluminum particles it seems the linear regime could be broken down into two separate growing regimes. Therefore, dust-rise data for the initial 1.45-mm entrainment is necessary.

Two windows on both sides of the test section have an approximate viewing area of 76 mm wide by 50 mm high, which in this study was used for applying the shadowgraph imaging technique. In the current experiment program, images were captured in the middle of the dust tray. The detailed dimensions of the parabolic and flat mirror arrangement to establish a shadow imaging technique has been previously presented in Figure 19. The width of the captured images is controlled by the concave mirror diameter, which is 69 mm in this case. It will be interesting to see the edge effect on the dust entrainment process behind moving shock front.

Adding a dump tank can be considered in the future, which would allow experiments with even greater shock strengths. A dump tank will absorb the reflected shock wave, and t

can facilitate a longer recording time of the data. All the experiments in the current study were subjected to shock waves ranging from M_s = 1.1 to 1.6. However, in real industry conditions, dust explosions are deflagrations that produce subsonic (M_s < 1) compression waves. Therefore, experiments with lower wave strength (M_S <1) need to be investigated to confirm whether they follow the same trends and behavior of dust entrainment behind the weaker shocks.

The shock-tube test section has the capability of having a top window of 1 by 12 inches and allows for the future use of laser scattering techniques. A laser sheet can be projected through the top window on the test section as shown in Figure 55. The laser scattering technique can be used to determine the combustible dust cloud concentration.

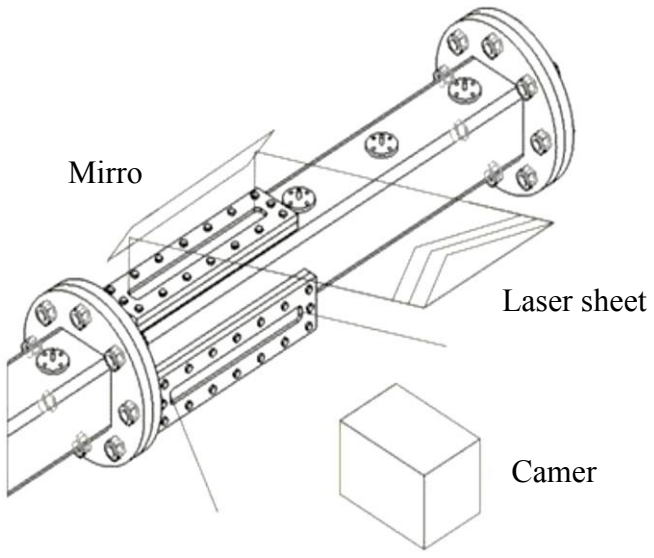

Figure 55: Laser scattering technique on shock-tube

The laser scattering technique in modern days can also identify the particle velocity. Particle velocity and dust cloud concentrations are valuable parameters for developing numerical models of dust cloud formation behind blast waves. Also, Large Scale Particle Imaging Velocimetry (LS-PIV) can be applied to the images. Successful application of LS-PIV will provide information about the velocity profile of an entrained dust cloud. Particle velocity measurements can provide very useful information, some of which are explained below:

- Capability to measure particle velocity will allow measurement of particle settling velocity which can be used for quantitative analysis of aerodynamic drag force and other lift forces such as Saffman or Magnus force. High polydispersity dusts exhibit higher growth rate due to particle collision which releases kinetic energy. Velocity measurement will help analyze this different hypothesis quantitatively to provide better correlations.
- Different research work has proposed correlations for threshold entrainment mass flux [66, 67] or threshold entrainment velocity [57]. To the best of our knowledge, none of the correlations address the issue of particle size polydispersity. With the current findings from this research, addition of velocity measurements of particles will allow developing stronger correlations.
- Another important aspect of velocity measurement is the understanding of the boundary layer effect. From our experimental findings, the presence of a turbulent dusty layer and turbulent mixing is evident. However comprehensive understanding of dusty boundary layer characteristics is required for proper dust

fire and explosion effects assessments. For instance, for developing effective numerical models with correlations considering turbulent boundary layer and turbulent mixing the following information can be useful: the turbulent dusty boundary-layer thickness, to characterize the boundary-layer profiles and the mean-flow velocity and density profiles. Velocity profiles can also indicate transition from laminar to turbulent boundary regime.

REFERENCES

1. R. K. Eckhoff, Dust explosions in the process industries, Third ed., Gulf Professional Publishing, Amsterdam, 2003.

2. CSB, Investigation Report. Combustible Dust Hazard Study, U.S Chemical Safety and Hazard Investigation Board, Washington, DC, 2006, pp. 1-108.

3. D. Y. Castellanos, The Influence of particle size and crystalline level on the combustion characteristics of particulated solids, Texas A&M University Doctoral Dissertation, College Station, 2013

4. CSB, Investigation Report. Sugar Dust Explosion and Fire, Imperial Sugar Company, U.S Chemical Safety and Hazard Investigation Board, Washington, DC, 2008.

5. B. Fletcher, The interaction of a shock with a dust deposit, Journal of Physics, D: Applied Physics **9**, (1976)197-202.

6. R.K. Eckhoff, Dust explosion research. State-of-the-art and outstanding problems, Journal of Hazardous Materials, 35 (1993) 103-117.

7. S. Mannan, and Frank P. Lees, Lee's loss prevention in the process industries: hazard identification, assessment, and control, 2005.

8. P. R. Amyotte, R. K. Eckhoff, Dust explosion causation, prevention and mitigation: An overview, Journal of Chemical Health and Safety, 17 (2009) 15-28.

9. P. van der Wel, Ignition and propagation of dust explosions, Delft University Doctoral Dissertation, Netherlands, 1993.

10. P. van der Wel, S. Lemkowitz, B. Scarlett, K. van Wingerden, A Study of Particle Factors Affecting Dust Explosions, Particle & Particle Systems Characterization, 8 (1991) 90-94.

11. United States OSHA, Combustible Dust in Industry: Preventing and Mitigating the Effects of Fire and Explosions
http://www.osha.gov/dts/shib/shib073105.html

12. United States OSHA, National Emphasis Program for Combustible Dust (Directive Number: CPL 03-00-008), 2006.

13. National Fire Protection Association, Standard for the Prevention of Fire and Dust Explosions from the Manufacturing, Processing, and Handling of Combustible Particulate Solids, 2013.

14. T. Skjold, Simplified modelling of explosion propagation by dust lifting in coal mines, Procedings on the 5th International Seminar on Fire and Explosion Hazards, Edinburgh, UK, 2007.

15. T. Skjold, Simulating the Effect of Release of Pressure and Dust Lifting on Coal Dust Explosions, Twenty-third International Colloquium on the Dynamics of Explosions and Reactive Systems (ICDERS), Poitiers, France, 2007.

16. S. Tateuki, A. Takashi, The effects of particle size on shock wave dust deposit interaction, Proc. of the 14th Intern. Symp. Space Technol. and Sci., (1984) 483-490.

17. A.V. Fedorov, Mixing in wave processes propagationg in gas mixtures (review). Combustion, Explosion, and Shock Waves, 40(2004) 17-31.

18. C.B. Brown, Engineering Hydraulics. John Wiley & Sons, New York, Chapter 12, 1950

19. L. Prandtl, The essential of fluid dynamics. Blackie & Son London, Chap 5, Sec 4, 1963.

20. J. H. Gerrard, An experimental investigation of the initial stages of the dispersion of dust by shock waves. British Journal of Applied Physics, 14(1963) 186-192.

21. A.A. Borisov, A.V. Lyubimov, S.M. Kogarko, and V.P. Kozenko, Instability of the surface of a granular medium behind sliding shock and detonation waves, Combustion, Explosion, and Shock Waves, 3(1), (1967) 95–96.

22. W. Merzkirch and K. Bracht, The erosion of dust by a shock wave in air: Initial stages with laminar flow, International Journal of Multiphase Flow, 4, (1978) 89–95.

23. K. Bracht and W. Merzkirch, Dust entrainment in a shock-induced, turbulent air flow, International Journal of Multiphase Flow, 5, No. 2, (1979) 301–312.

24. C. C. Hwang, J. M. Singer, and T. N. Hartz, Dispersion of dust in a channel by a turbulent gas stream, Rep. Invest. No. 7854, U.S. Bureau of Mines. Pittsburgh, PA (1974).

25. C. C. Hwang, Interaction of a coal dust-bed with shock induced air stream, W. Merzkirch (ed.), Flow Visualization II, Hemisphere, Germany (1982), 547–551.

26. V. M. Boiko, and A. N. Papyrin, Dynamics of the formation of a gas suspension behind a shock wave sliding over the surface of a loose material, Combustion, Explosion, and Shock Waves, 23(2),(1987) 231-235.

27. R. Klemens, P. Zydak, M. Kaluzny, D. Litwin, and P. Wolanski, Dynamics of dust dispersion from the layer behinds the propagation shock wave, Journal of Loss Prevention in the Process Industries, 19 (2006) 200-209.

28. R. Klemens, P. Oleszczak, and P, Zydak, Experimental and numerical investigation into the dynamics of dust lifting up from the layer behind the propagating shock wave, Shock Waves, 23(2012) 263–270.

29. B. E. Gelfand, S. P. Medvedev, A. A. Borisov, Shock loading of stratified dusty systems, Arch. Combust., 9, Nos. 1/4, (1989)153–165.

30. P. Manjunath, and J. Kurian, Shock interaction with a dust layer, Shock Waves, Proc.18th Int. Symposium. (1991) 499–504.

31. S. P. Medvedev, J. H. Cheng, and H. Gronig, Shock-tube study of dust layer dispersion by rarefaction wave, Proc. 5th Int. Colloquium Dust Explosions, Pultusk near Warsaw, Poland (1993), 287–292.

32. T. Skjold, Flame propagation in dust clouds: challenges for model validation, 8th International Symposium on Hazards, Prevention and Mitigation of Industrial Explosions (ISHPMIE), Yokohama, Japan, 2010.

33. Y.-C. Li, A. S. Harbaugh, C. G. Alexander, Deflagration to detonation transition fueled by dust layers, Shock Waves, 5, (1995) 249–258.

34. A. V. Fedorov, N. N. Fedorova, I. A. Fedorchenko, Mathematical simulation of dynamic phenomena in mixtures of a gas and solid particles, Preprint No. 2-2001, Inst. Theor. Appl. Mech., Sib. Div., Russ. Acad. of Sci., Novosibirsk (2001).

35. A. V. Fedorov, N. N. Fedorova, I. A. Fedorchenko, and V. M. Fomin, Mathematical simulation of dust lifting from the surface, J. Appl. Mech. Tech. Phys., 43, No. 6, (2003) 877–887.

36. L. Kuhl, K.Y. Chien, R. E. Ferguson, J. P. Collins, H.M. Glaz, & P. Colella, Simulation of a turbulent, dusty boundary layer behind a shock, Current Topics in Shock Waves, Kim, Y. W. (ed.), American Institute of Physics, New York, (1990)762-769.

37. R. Houim, E. Oran, Numerical simulation of dilute and dense layered coal-dust explosions, Combustion Institute 35, (2015) 2083-2090.

38. R. Klemens, P. Wolanski, P. Kosinski, On combustion and detonation behind a shock wave propagating over dust layer, Khim. Fiz., 20, No. 7, (2001)112–118.

39. H. Sakakita, A. K. Hayashi, A. I. Ivandaev, Numerical simulation of shock wave interaction with powder layers, K. Takayama (ed.), Shock Waves, Springer, Heidelberg, 1992.

40. N. Thevand and E. Daniel, Numerical study of the lift force influence on two-phase shock-tube boundary layer characteristics, Shock Waves, 12, No. 4, (2002) 279–288.

41. D. Guggenhelm, Transient Measurements in a shock-tube, AE3051 Experimental fluid dynamics, Georgia Institute of Technology, 2011

42. A. G. Gayden, and I. R. Hurle, The Shock-Tube in High Temperature Chemical Physics, Reinhold, New York, NY,1963.

43. J. E. John, and T. G. Keith, Gas Dynamics, Pearson / Prentice Hall, Upper Saddle River, NJ, 2006, 3rd Edition.

44. Marks, A new facility for studying shock wave passage over dust layers. Masters Thesis, Texas A & M University, 2013.

45. Rotavera, Chemiluminescence and ignition delay time measurements of C_9H_{20}, M.S. Thesis, Texas A&M University, 2009.

46. Rotavera, E.L Petersen, Model Predictions of Higher-Order Normal Alkane Ignition from Dilute Shock-Tube Experiments, Shock Waves 23, (2013)345-359.

47. J. Neggers, Image Measurement Utility. MATLAB Central. N.p., (2012). Web.

48. J. E. A. John, Gas Dynamics, 2nd edition, Prentice-Hall, Englewood Cliffs, 1984

49. J. D. Anderson, Modern Compressible Flow, 2nd edition, McGraw-Hill, Boston, 1990

50. J. N. B. Bradley, Shock Waves in Chemistry and Physics, Methuen, London, 1962.

51. I. Glass, W. A. Martin, and G. N. Patterson, A Theoretical and Experimental Study of the Shock-Tube, University of Toronto Institute for Aerospace Studies Report, November, (1953)1-45.

52. Bitondo, and R. K. Lobb, Design and Construction of a Shock-Tube, University of Toronto Institute for Aerospace Studies Report, (1950) 1-19.

53. M D. Salas, On the Thermodynamic Theory of Waves of Finite Longitudinal Disturbance, 17th Shock Interaction Symposium, Rome, Italy, (2006) 1-20.

54. W. J. M Rankine, On the Thermodynamic Theory of Waves of Finite Longitudinal Disturbances, Philosophical Transactions of the Royal Society, Vol. 160, 1870, 277-288.

55. H. Hugoniot, Propagation des Mouvements dans les Corps et Spécialement dans les Gaz Parfaits, Journal de l'Ecole Polytechnique, Vol. 57, 1887.

56. A. Christopher, An experimental study into the ignition of Methane AND Ethane blends in a new shock-tube facility, M.S. Thesis, Texas A&M University (2009).

57. A. Ural, Towards Estimating Entrainment Fraction For Dust Layers, Fire Protection Research Foundation, June 2011

58. R. A. Bagnold, The Physics of Blown Sands and Desert Dunes, Methuen and Co., London 1941.

59. B. Li, Evaluating the von karman constant in sediment-laden airflow, Texas A&M University Doctoral Dissertation, College Station, 2010

60. R. Clift, Bubbles, Drops, and Particles, Academic Press, New York, 1978.

61. M. E. O'Neill, A Sphere in Contact with a Plane Wall in a Slow Linear Shear Flow, Chemical Engineering Science, v. 23, (1968) 1293-1298.

62. G. K. Batchelor, and C. S. Wen, Sedimentation in a Dilute Polydisperse System of Interacting Spheres, Part 2, Numerical Results, Journal of Fluid Mechanics, v. 124, (1982) 495-528.

63. G. K. Batchelor, Sedimentation in a Dilute Dispersion of Spheres, Journal of Fluid Mechanics, v. 52, Part 2, (1972) 245-268.

64. P. G. Saffman, The Lift on a Small Sphere in a Slow Shear Flow," originally published in J. Fluid Mech., v. 22, Part 2, (1965) 385-400, and amended in v. 31, 624.

65. W. Cleaver, and B. Yates, Mechanism of Detachment of Colloidal Particles from a Flat Substrate in a Turbulent Flow, Journal of Colloid and Interface Science, v. 44, No. 3, (1973) 464—474.

66. P. Zydak, and R. Klemens, Modelling of dust lifting process behind propagating shock wave, Journal of Loss Prevention in the Process Industries, 20, (2007) 417-426.

67. T. Skjold, Review of the DESC project. Journal of Loss Prevention in the Process Industries, 20, (2007) 291-302.

68. P. Kosinski, A. C. Hoffmann, and R. Klemens, Dust lifting behind shock waves: comparison of two modeling techniques. Chemical Engineering Science, 60, (2005) 5219-5230.

69. Crowe, Review—numerical models for dilute gas–particle flows, Journal of Fluids Engineering 104, (1982) 297–303.

70. G. S. Settles, Schlieren and shadowgraph techniques, Springer-Verlag Berlin Heidelberg, Germany, 2006.

71. J. Klein, A planview shadowgraph technique for boundary-layer visualization, AIAA Journal, Vol 8 (1970) 963-965

72. S. Settles, The state of the art of conventional flow visualization techniques for wind tunnel testing, NASA CP-2243 (1982) 9-26.

73. H. Kiefer, M. Z. Al-Alami, J. C. Hajduk, Physical optics of the laser-schlieren shock-tube technique, Applied Optics, Vol. 20(2), (1981), 221-230

74. J. M. Singer, E. B. Cook, and J. Grumer, Dispersal of Coal- and Rock-Dust Deposits, U.S. Bureau of Mines, RI 7642, 1072.

75. J. M. Singer, M.E. Harris, and J. Grumer, Dust Dispersal by Explosion-Induced Airflow: Entrainment by Airblast," US Bureau of Mines, RI 8130, 1976

76. P. R. Amyotte, K. J. Mintz, M. J. Pegg, Y-H. Sun, K.I. Wilkie, Effects of methane admixture, particle size and volatile content on the dolomite inerting requirements of coal dust, Journal of Hazardous Materials, Vol.27(2), (1991) 187-203

77. Title 30 Code of Federal Regulations (30 CFR) (http://www.msha.gov/)

78. NFPA 68, Standard on Explosion Protection by Deflagration Venting, National Fire Protection Association, 2007.

79. CSB public hearing June 22, 2005. [www.gpo.gov] [FR Doc No: 05-9238]

80. CSB, Investigation Report. Aluminum Dust Explosion, Hayes Lemmerz International-Huntington, Inc., U.S Chemical Safety and Hazard Investigation Board, Washington, DC, 2005.

81. Nifuku, S. Koyanaka, H. Ohya, C. Barre, M. Hatori, S. Fujiwara, S. Horiguchi, I. Sochet, Ignitability characteristics of aluminum and magnesium dusts that are

generated during the shredding of post-consumer wastes, Journal of Loss Prevention in the Process Industries, 20 (2007) 322-329.

82. D.C. May, D.L. Berard, Fires and explosions associated with aluminum dust from finishing operations, Journal of Hazardous Materials, 17 (1987) 81-88.

83. O. Dufaud, M. Traoré, L. Perrin, S. Chazelet, D. Thomas, Experimental investigation and modelling of aluminum dusts explosions in the 20 L sphere, Journal of Loss Prevention in the Process Industries, 23 (2010) 226-236.

84. The Aluminum Association, Inc., 2000. Guidelines for Handling Aluminum Fines Generated During Various Aluminum Fabricating Operations, Publication F1.

85. The Aluminum Association, Inc., 1990. Recommendations for Storage and Handling of Aluminum Powders and Paste, Publication TR-2.

86. PSD analysis provided by vendor Henan Yuanyang Aluminium Industry Co,. Ltd, http://en.hnyyly.com/

87. A. Janes, J. Chaineaux, D. Carson, P.A. Le Lore, MIKE 3 versus HARTMANN apparatus: Comparison of measured minimum ignition energy (MIE), Journal of Hazardous Materials, 152 (2008) 32-39.

88. K.L. Cashdollar, Coal dust explosibility, Journal of Loss Prevention in the Process Industries, 9 (1996) 65-76.

89. Alderliesten, Mean Particle Diameters. Part III: An Empirical Evaluation of Integration and Summation Methods for Estimating Mean Particle Diameters from Histogram Data, Particle & Particle Systems Characterization, 19 (2002) 373-373.

90. Baudry, S. Bernard, P. Gillard, Influence of the oxide content on the ignition energies of aluminium powders, Journal of Loss Prevention in the Process Industries, 20 (2007) 330-336.

91. R.K. Eckhoff, Does the dust e plosion risk increase when moving from μm-particle powders to powders of nm-particles?, Journal of Loss Prevention in the Process Industries, 25 (2012) 448-459.

92. C. G. Ilea, P. Kosinski, A. C. Hoffmann, The effect of polydispersity on dust lifting behind shock waves, Powder Technology 196 (2009) 194–201

93. J M. Singer, N. B. Greninger, and J. Grumer, Some Aspects of the Aerodynamics of Formation of Float Coal Dust Clouds, U.S. Bureau of Mines, RI 7252, 1969.

94. P. K. Kundu and I. M. Cohen, Fluid mechanics, Fourth ed., Elsvier Inc, London, UK, 2008

95. Y.-C. Li, A. S. Harbaugh and C. G. Alexander, Deflagration to detonation transition fueled by dust layers, Shock Waves, 5, (1995) 249–258.

96. ASTM E 1226, Standard Test Method for Explosibility of Dust Clouds.

97. ASTM E 1515, Standard Test Method for Minimum Explosible Concentration of Combustible Dusts.

98. A. L. Kuhl, R. E. Ferguson, K. Y. Chien. and J. P. Collins, Turbulent Dusty Boundary Layer in an ANFO Surface-Burst Explosion, Defense Nuclear Agency Technical Report DNA-TR-92-17, 1992.

99. General Duty Clause of the OSH Act of 1970 (https://www.osha.gov/index.html)

100. A. V. Fedorov, Mixing in Wave Processes Propagating in Gas Mixtures (Review), Combustion, Explosion, and Shock Waves, Vol. 40, No. 1, (2004) 17–31

101. A. Y. Chowdhury, H. G. Johnston, B. Marks, B., S. Mannan, and E. L. Petersen, Effect of shock wave on dust entrainment behind moving shock wave, Journal of Loss Prevention, (2015).

APPENDIX A

NOMENCLATURE

$_s$	Speed of sound through gas in zone 1
$_2$	Speed of sound through gas in zone 2
	1.4, specific heat ratio of air
M_S	Mach number of incident shock wave represents shock strength
M_r	Mach number of reflected shock wave
P_1	Pressure at zone 1 of shock-tube
P_2	Pressure at zone 2 of shock-tube
P_5	Pressure at zone 5 of shock-tube
R	Ideal gas constant
T_1	Temperature at zone 1 of shock-tube
T_2	Temperature at zone 2 of shock-tube
T_5	Temperature at zone 5 of shock-tube
V_S	Velocity of incident shock wave
V_2	Velocity of gas medium in zone 2 of shock-tube
V_r	Velocity of reflected shock wave
X_0	Location of diaphragm
X_t	Optimum test section location, where reflected shock and contact surface cross
X_W	Shock-tube driven section length
Y	Dust particle height; height of dust layer boundary
F_D	Drag force

C_D Drag coefficient

A Particle cross sectional area

D Particle diameter

ρ Air density

U Velocity of air medium

Re_d Reynolds number

U_t Terminal settling velocity of particle

ρ_p Particle density

F_{LS} Saffman force

ΔV Velocity gradient

F_{LT} Turbulent burst lift force

τ Dust-layer rise delay time

t_{tr} Regime transition time

α Initial linear dust rise rate

δy_{p-p} Peak-to-peak fluctuation

D_{50} Median particle size

$D_{3,2}$ Sauter mean diameter

σ_D Particle size polydispersity

K_{ST} Dust explosion deflagration constant

APPENDIX B

P2/P1 DETERMINATION IN SHOCK-TUBE

P4 and P1 are input value. Applying Newton Raphson method P2/P1 ration can be calculated using the following formula. Initially P2/P1 was determined this way in our experiment for back calculation of shock Mach number to validate velocity data measurement.

Table 11: Formula and different input variable

f(p) = (p4/p1)*(1-c1(p2/p1-1)/(sqrt(1+(c2+1)(p2/p1-1)))^(c3)-p2/p1 c1 = (g4-1)/(2g1)*(a1/a4) c2 = (g1+1)/2g1 c3 = 2g4/(g4-1) p = p2/p1				a = sqrt(gRT) = speed of sound in the gas g = specific heat ratio R = ideal gas constant of gas N*m/kg*K T = temp of gas K				
			driven			**driver**		
p1	67	kPa	Air			Helium		
p4	3723	kPa	a1	348.920335	m/s	a4	348.920335	m/s
c1	0.142857143		g1	1.4		g4	1.4	
c2	0.857142857		R1	287	N*m/kg*K	R4	287	N*m/kg*K
c3	7		T1	303	K	T4	303	K

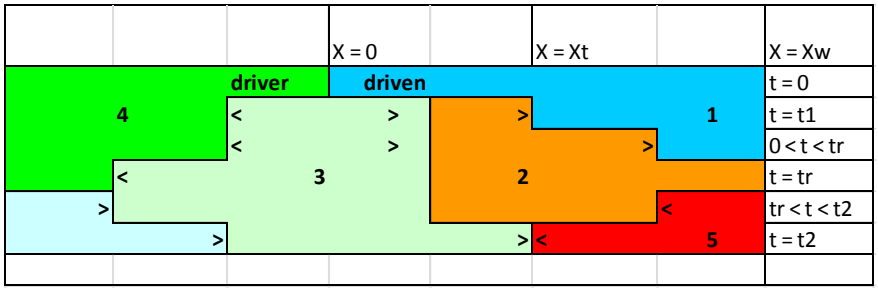

Figure 56: X-t diagram of shock-tube showing different zones considered in calculation

Table 12: Trial and error applying Newton Raphson formula to determine the P2/P1

Newton Rhapson Method to find p2/p1 (let p = p2/p1)					
p old	**f(p)**	**f(p+dp)**	**f(p-dp)**	**df(p)/dp**	**p new**
2.000000	23.595406	23.424760	23.767557	-17.139828	3.376642
3.376642	8.815142	8.747573	8.883067	-6.774665	4.677834
4.677834	2.213746	2.175544	2.252088	-3.827155	5.256265
5.256265	0.208673	0.177272	0.240172	-3.145007	5.322616
5.322616	0.002151	-0.028607	0.033005	-3.080583	5.323314
5.323314	0.000000	-0.030751	0.030847	-3.079918	5.323314
5.323314	0.000000	-0.030752	0.030847	-3.079918	5.323314
5.323314	0.000000	-0.030752	0.030847	-3.079918	5.323314
5.323314	0.000000	-0.030752	0.030847	-3.079918	5.323314
5.323314	0.000000	-0.030752	0.030847	-3.079918	5.323314

The obtained P2/P1 can be used in following equation to determine Mach number.

Mach number will also be calculated from the obtained shock speed data.

$$\frac{P_2}{P_1} = \frac{2\gamma}{\gamma+1} M_s^2 - \frac{\gamma-1}{\gamma+1} \quad (3)$$

APPENDIX C

SHOCK-TUBE OPTIMUM LOCATION DETERMINATION

From the *Rankine-Hugoniot equations* [53-55] the following formula can be generated:

$$X_t = \frac{\frac{V_r}{V_s}+1}{\frac{V_r}{V_2}+1} X_w \qquad (16)$$

$$t_o = \frac{X_w - X_t}{V_s} + \frac{X_w - X_t}{V_r} \qquad (17)$$

Equation 16 and 17 are applied to calculate the optimum test section location, the optimum value in the following table is shown as highlighted. Table below shows the calculated optimum test location, maximum possible observation time (t0) for each Mach number. According to the calculation for incident shock with Ms#2 the maximum observation time for experiment is 2.79 ms.

Table 13: Calculation to determine optimum test location

Vs	M1s	p2/p1	V2	M2	T2/T1	T2	a2	Vr	p5/p2	Msr	T5/T2	Xw	tr	Xt	t1	t2	to	Test time (ms)
375	1.08	1.20	46.42	0.13	1.05	314.2566	355.34	337.86	1.20	1.08	1.05	3.981	10.6160	0.9141	2.4377	19.6932	17.2555	3.65549237
400	1.16	1.39	83.88	0.23	1.10	327.9003	362.97	332.89	1.37	1.15	1.10	3.981	9.9525	1.4681	3.6701	17.5013	13.8312	3.5759223
425	1.23	1.59	119.39	0.32	1.15	341.4182	370.38	329.49	1.55	1.21	1.14	3.981	9.3671	1.8797	4.4229	15.7445	11.3216	3.5005503
450	1.30	1.81	153.27	0.41	1.19	354.9681	377.66	327.39	1.72	1.27	1.17	3.981	8.8467	2.1930	4.8732	14.3082	9.4350	3.42827773
475	1.37	2.03	185.77	0.48	1.24	368.6673	384.88	326.38	1.90	1.33	1.21	3.981	8.3811	2.4362	5.1288	13.1141	7.9853	3.35838694
500	1.44	2.27	217.11	0.55	1.28	382.6048	392.08	326.32	2.07	1.39	1.25	3.981	7.9620	2.6285	5.2569	12.1069	6.8499	3.29041973
525	1.52	2.52	247.44	0.62	1.33	396.8485	399.32	327.05	2.25	1.44	1.28	3.981	7.5829	2.7828	5.3007	11.2464	5.9458	3.22409316
550	1.59	2.78	276.91	0.68	1.38	411.4516	406.60	328.47	2.42	1.49	1.31	3.981	7.2382	2.9085	5.2882	10.5033	5.2151	3.15924099
575	1.66	3.05	305.64	0.74	1.43	426.4559	413.94	330.49	2.59	1.54	1.34	3.981	6.9235	3.0121	5.2384	9.8552	4.6168	3.09577311
600	1.73	3.34	333.70	0.79	1.48	441.8945	421.37	333.04	2.75	1.58	1.38	3.981	6.6350	3.0984	5.1640	9.2851	4.1210	3.03364745
625	1.81	3.64	361.18	0.84	1.54	457.7942	428.88	336.05	2.92	1.63	1.41	3.981	6.3696	3.1711	5.0737	8.7797	3.7059	2.97285083
650	1.88	3.95	388.16	0.89	1.59	474.1767	436.49	339.47	3.08	1.67	1.43	3.981	6.1246	3.2328	4.9736	8.3286	3.3550	2.91338598
675	1.95	4.27	414.68	0.93	1.65	491.0598	444.19	343.26	3.23	1.71	1.46	3.981	5.8978	3.2857	4.8677	7.9234	3.0558	2.85526296
700	2.02	4.61	440.79	0.98	1.71	508.458	451.99	347.37	3.38	1.74	1.49	3.981	5.6871	3.3313	4.7590	7.5575	2.7986	2.79849361
725	2.10	4.95	466.54	1.01	1.77	526.3836	459.89	351.77	3.53	1.78	1.52	3.981	5.4910	3.3709	4.6495	7.2254	2.5758	2.54556268
750	2.17	5.31	491.96	1.05	1.83	544.8468	467.89	356.43	3.67	1.81	1.54	3.981	5.3080	3.4056	4.5407	6.9224	2.3817	2.32975827
775	2.24	5.69	517.08	1.09	1.89	563.8559	475.98	361.33	3.81	1.85	1.57	3.981	5.1368	3.4360	4.4336	6.6450	2.2114	2.14401552
800	2.31	6.07	541.94	1.12	1.96	583.4185	484.17	366.45	3.94	1.88	1.59	3.981	4.9763	3.4630	4.3287	6.3899	2.0612	1.98285126
825	2.38	6.47	566.55	1.15	2.03	603.5404	492.45	371.76	4.07	1.91	1.61	3.981	4.8255	3.4869	4.2265	6.1546	1.9280	1.84199291

APPENDIX D

TRANSITION TIME AND SHOCK STRENGTH RELATION

Regime transition time, t_{tr} and shock strength relation

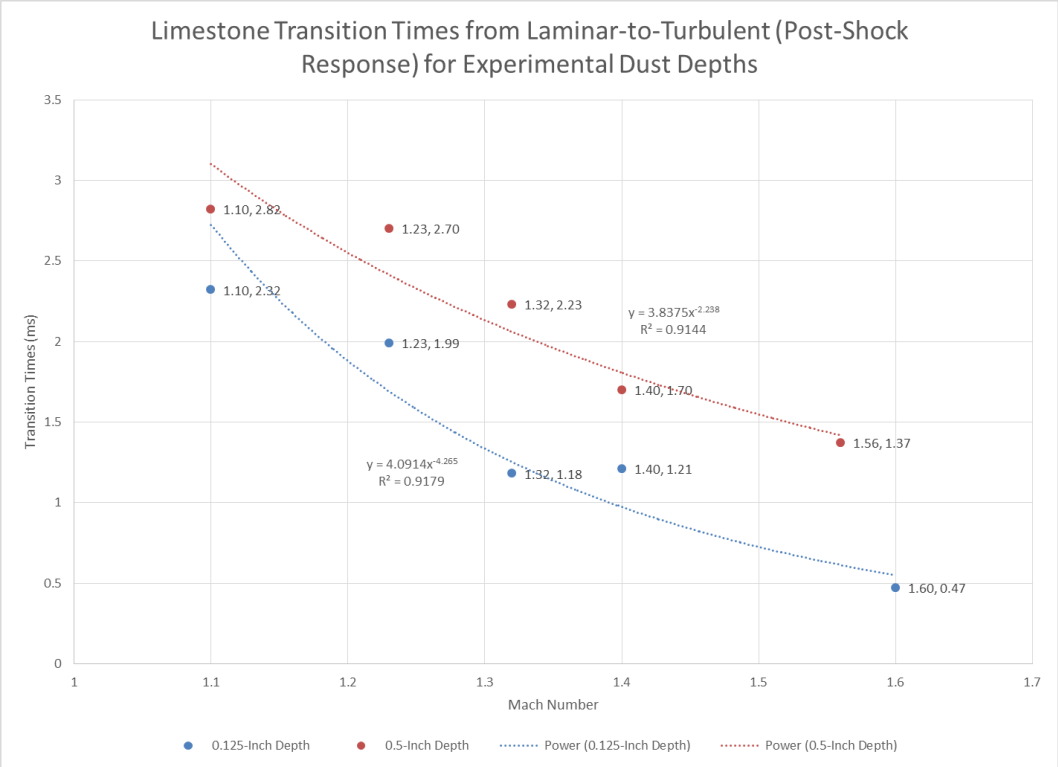

Figure 57: Transition from fast growing linear regime to more surface fluctuating lower growth rate regime at $t=t_{tr}$